Model selection for gravitational-wave transient sources

Jade Powell, MPhys

Submitted in fulfilment of the requirements
for the Degree of Doctor of Philosophy

School of Physics & Astronomy
College of Science & Engineering
University of Glasgow

May 2017

Abstract

A hundred years after Einstein predicted the existence of gravitational waves, the Advanced Laser Interferometer Gravitational-wave Observatory (aLIGO) [1] made the first direct detection of gravitational waves from the binary black hole system GW150914 [2]. With the Advanced Virgo (AdVirgo) [3] gravitational-wave detector joining the detector network in 2017, multiple detections of gravitational-wave signals are predicted over the network operating time [4, 5]. As well as binary sources, other potential sources for an advanced detector network include core-collapse supernovae. A detection of a core-collapse supernova gravitational-wave signal will allow us to measure astrophysical parameters of the dying massive star. Gravitational waves are emitted from deep inside the core where the star is opaque to electromagnetic radiation. Therefore, they are direct probes of parameters that cannot be determined electromagnetically, such as, the core-collapse supernova explosion mechanism.

A detection of a core-collapse supernova signal is challenging, as noise of non-astrophysical origin contaminates the science data taken by the advanced detectors. Due to complicated simulations of the physics involved in core-collapse supernovae, the exact waveform of a core-collapse supernova signal is unknown. Noise transients in the detectors limit the false alarm rate of astrophysical detections, and could potentially mimic a core-collapse supernova signal. They can reduce the duty cycle of the detectors, which is particularly harmful for core-collapse supernovae detections due to their low event rate. Prompt characterization of instrumental and environmental noise transients will be critical for improving the sensitivity of the advanced detectors during observing runs.

During the science runs of the initial gravitational-wave detectors, noise transients were manually classified by visually examining the time-frequency scan of each event [6]. Here, we present a Bayesian model selection algorithm designed for the automatic classification of noise transients in advanced gravitational-wave detectors. The algorithm is tested on simulated data sets and real non-Gaussian, non-stationary aLIGO noise, and we demonstrate the ability to automatically clas-

sify transients by frequency, SNR and waveform morphology. A classification of noise transients as data is taken can lead to an improvement in data quality during an observing run and determine their origin.

In this thesis, we show how Bayesian model selection can be used to determine if a core-collapse supernova candidate gravitational-wave signal is a noise transient, a core-collapse supernova signal or other astrophysical transient. If the signal is a core-collapse supernova detection, we show how the core-collapse supernova explosion mechanism can be determined using a combination of principal component analysis and Bayesian model selection. We use the latest three-dimensional simulations of gravitational-wave signals from core-collapse supernovae exploding via neutrino-driven convection and rapidly-rotating core-collapse. We show that with an advanced detector network, we can determine if the core-collapse supernova explosion mechanism is neutrino-driven convection for sources in our Galaxy, and rapidly-rotating core collapse for sources out to the Large Magellanic Cloud.

Contents

List of Figures

List of Tables

Acknowledgements

I would like to thank my supervisor Siong Heng for his help and support. Thank you to my office mates Gareth Davies and Daniel Williams, and especially Matt Pitkin who has helped me out with many technical problems. I have benefited from many conversations with the rest of the Glasgow IGR group, especially Graham Woan, Chris Messenger, Joshua Logue, Ignacio Santiago, Brynley Pearlstone, Yiming Hu, Martin Hendry, Xilong Fan, Mervyn Chan, David Keitel, Joe Bayley and Natalia Korsakova. Thank you Gail Penny for all of the walks around beautiful Scotland.

From the LIGO and Virgo collaborations I would like to thank Elena Cuoco, Marco Cavaglia, Daniele Trifiro, Salvatore Vitale, James Clark, Alejandro Torres, Toni Font, Scott Coughlin and Jonah Kanner for their help and support with my research. I would like to thank Marek Szczepanczyk, Michele Zanolin and the rest of the LIGO supernova group for the impact they have had on my research. I would like to thank STFC for funding my thesis and the Scottish University Physics Alliance.

I would like to thank my mum Julie Moffat for her help and support, and the rest of my family, especially Benn Powell, Simon Powell, Allison Powell, Heleana Powell, Joel Powell, Daniel Powell and Andrew Moffat. Most of all, thank you to my baby Lewis Powell and my husband Simon Stevenson.

Declaration and Papers

I, Jade Powell, confirm that the work in this thesis is my own. Chapter 1 gives a background on gravitational waves. Appropriate references have been given for figures and information from other sources.

The work in Chapter 2 is the result of collaboration with Daniele Trifiro, Marco Cavaglia, Elena Cuoco and Siong Heng. The PCAT and WDF-ML results used in the comparison study were produced by Daniele Trifiro and Elena Cuoco, respectively. All PC-LIB results are produced by me. All analysis and figures are entirely my own or referenced appropriately. This work is published in Classical and Quantum Gravity [7], and it is reproduced here with permission of the journal.

The work in Chapter 3 is the result of collaboration with Daniele Trifiro, Marco Cavaglia, Elena Cuoco, Ryan Lynch, Toni Font, Alejandro Torres and Siong Heng. The PCAT, WDF-ML and Omicron results used in the comparison study were produced by Marco Cavaglia, Alejandro Torres and Ryan Lynch, respectively. All PC-LIB results are produced by me. All analysis and figures are entirely my own or referenced appropriately. This work is published in Classical and Quantum Gravity [8], and is reproduced here with permission of the journal.

The work in Chapter 4 is the result of collaboration with Joshua Logue, Siong Heng, Sarah Gossan, Christian Ott and James Clark. All results, analysis and figures are entirely my own or referenced appropriately. This work is published in Physical Review D [9], and is reproduced here with permission of the journal.

The work in Chapter 5 is the result of collaboration with Marek Szczepanczyk and Siong Heng. The cWB triggers were produced by Marek Szczepanczyk. All results, analysis and figures are entirely my own or referenced appropriately. The

conclusions in Chapter 6 are entirely my own.

Chapter 1

Introduction

The existence of gravitational waves (GWs) was first predicted in 1915 by Einstein's theory of general relativity [10, 11]. A hundred years later, the Advanced Laser Interferometer Gravitational-wave Observatory (aLIGO) [1] made the first direct detection of GWs from the binary black hole system GW150914 [2]. With the Advanced Virgo (AdVirgo) Italian GW detector [12, 3] joining the detector network in 2017, current rate predictions for compact binary events [13, 4, 5, 14, 15] indicate that the advanced detector network will lead to multiple detections of GW signals over the network operating time. A new era of GW astrophysics has begun, opening a new window on the Universe outside of the electromagnetic spectrum.

In this chapter, we give an introduction to GWs, the detectors, and their source properties. In Section 1.1, we give an overview of GWs and their properties. In Section 1.2, a brief description of the potential sources for ground based GW detectors is given. This thesis focuses in particular on GW bursts sources with waveforms that are un-modelled due to unknown or difficult to simulate astrophysics. In Section 1.3, we describe the GWs detectors. In particular, we provide a detailed description of the aLIGO detectors, and we include a brief description of the detectors potential noise sources.

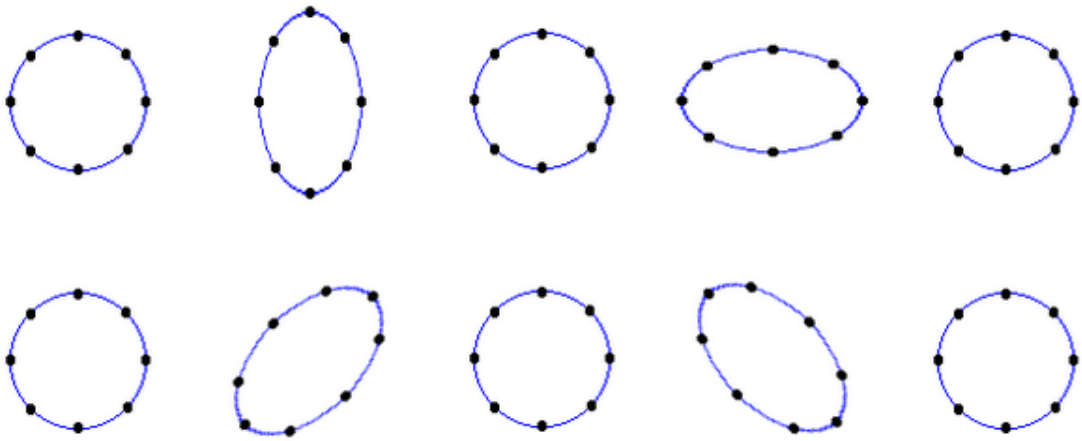

Figure 1.1: The effect of the two GW polarizations, h_+ (top), and $h_\times$ (bottom), on a ring of test masses as a GW signal moves into the page. The circle of test masses is stretched and squeezed transverse to the direction of propagation. Figure reproduced from [16].

1.1 Gravitational Waves

GWs are ripples in space time that are produced by accelerating masses. They were predicted by Einstein's theory of general relativity [10, 11]. Einstein's equations describe how gravity is the curvature of space time created by large masses. Assuming the GWs are small, weak perturbations in linear space, solving Einstein's equations gives a solution that is a plane wave equation. The waves travel transverse to the direction of propagation, at a speed equal to the speed of light. GWs only interact weakly with matter, but they can be detected by their effects on freely falling test masses. GWs have two polarizations, known as h_+ and $h_\times$, and are orthogonal with an angle between the polarizations of $\pi/4$. The effect of the two polarizations on a ring of test masses is illustrated in Figure 1.1. As a GW moves into the page, the circle of test masses is stretched in one direction and squeezed in another direction.

The first indirect detection of GWs came from the Hulse Taylor binary pulsar system PSR 1913+16 [17, 18]. A pulsar is a rapidly rotating neutron star, that emits regular pulses of electromagnetic radiation. A neutron star is a very high density star composed mainly of closely packed neutrons. The pulsar was detected in 1974, and its orbital period showed that it was in a binary system with another neutron star. General relativity predicts that as the binary system orbits it should lose energy due to the emission of GWs. This results in a decrease in the orbital period as the stars start to inspiral towards each other and eventually merge. The orbital period of PSR 1913+16 was measured for a number of years, and agreed

perfectly with the decrease predicted by the emission of GWs. Hulse and Taylor were awarded the Nobel prize for the discovery in 1993. The first direct detection of GWs was made by the aLIGO detectors on the 14th of September 2015 [2], and a second detection was made on the 26th of December 2015 [19]. In the next section, we describe in more detail the current detected sources, and other possible sources for ground based detectors.

1.2 Gravitational-Wave Sources

Potential sources of GWs can be roughly split into four groups. They are compact binary coalescences (CBC) signals, which are produced by in-spiralling binary neutron stars or black holes, which are areas of space time with a gravitational potential well so large that nothing can escape, continuous sources that may be produced by an individual neutron star with a mountain on the surface, burst sources with an unknown waveform, or a stochastic GW background that may be due to a superposition of GW background sources or remnant GWs from the big bang. In the remainder of this section, we give more details about the potential sources, with a particular focus on short duration transient sources as they are the sources considered in later chapters of this thesis.

1.2.1 Continuous Waves

Continuous GWs may be emitted by neutron stars, which typically have a mass of $1.4\,\mathrm{M}_{\odot}$ and a radius of 10 km. Conservation of angular momentum and magnetic flux can result in neutron stars with extremely rapid spins and strong magnetic fields. To emit a continuous GW, a neutron star must have a deformation or a mountain on the surface. The radiation amplitude is given by,

$$h \sim \frac{4}{5}(2\pi R f)^2 \frac{\epsilon M}{r}, \tag{1.1}$$

where ϵ is the fractional asymmetry that is proportional to the mass of the bump on the surface, f is the frequency, R is the radius, M is the mass, and r is the distance [20]. A detection of continuous GWs could determine the neutron star equation of state, and help understand neutron star glitches [21]. As neutron stars emit

electromagnetic radiation, it is possible to target searches of GWs for neutron stars with positions, frequencies and spin-downs known from X-ray, radio and gamma-ray observations [22]. Examples are the Crab and Vela pulsars. Months of observations with ground based detectors will be necessary for the detection of continuous GWs. Continuous GWs have not yet been detected, but current searches have produced upper limits for their emission [22, 23].

1.2.2 Stochastic Background

A stochastic GW background may consist of a superposition of weak GWs, and are expected to be a promising source for future spaced based GW detectors [24]. They could be composed of white dwarf or black hole binary systems. A stochastic GW background from the early Universe may be caused by a flux of gravitons left over from when the Universe became optically thin to gravitons, just before Big Bang Nucleosynthesis occurred. A GW background would allow us to test theories about the earliest possible moments in our Universe [25].

1.2.3 Compact Binaries

CBC signals are the most promising sources of GWs for ground based GW detectors, and the only source directly detected during the first aLIGO observing run (O1) [2, 19]. The components of the binary must consist of neutron stars or black holes. They are ideal sources for ground based GW detectors, as their orbital separation can become small enough before they merge for them to emit GWs in the detectors sensitive frequency band. If one of the components of the binary is a neutron star then there may be an electromagnetic counterpart to the GW signal [26].

The typical waveform of a CBC signal is shown in Figure 1.2. The signal has three main parts. The first is the inspiral that increases in frequency and amplitude as the compact objects move closer together, and energy and angular momentum is carried away in GWs. The second is the merger when the black holes or neutron stars collide, and finally there is a ringdown phase.

As the waveforms of CBC GW signals are well known, is it possible to perform

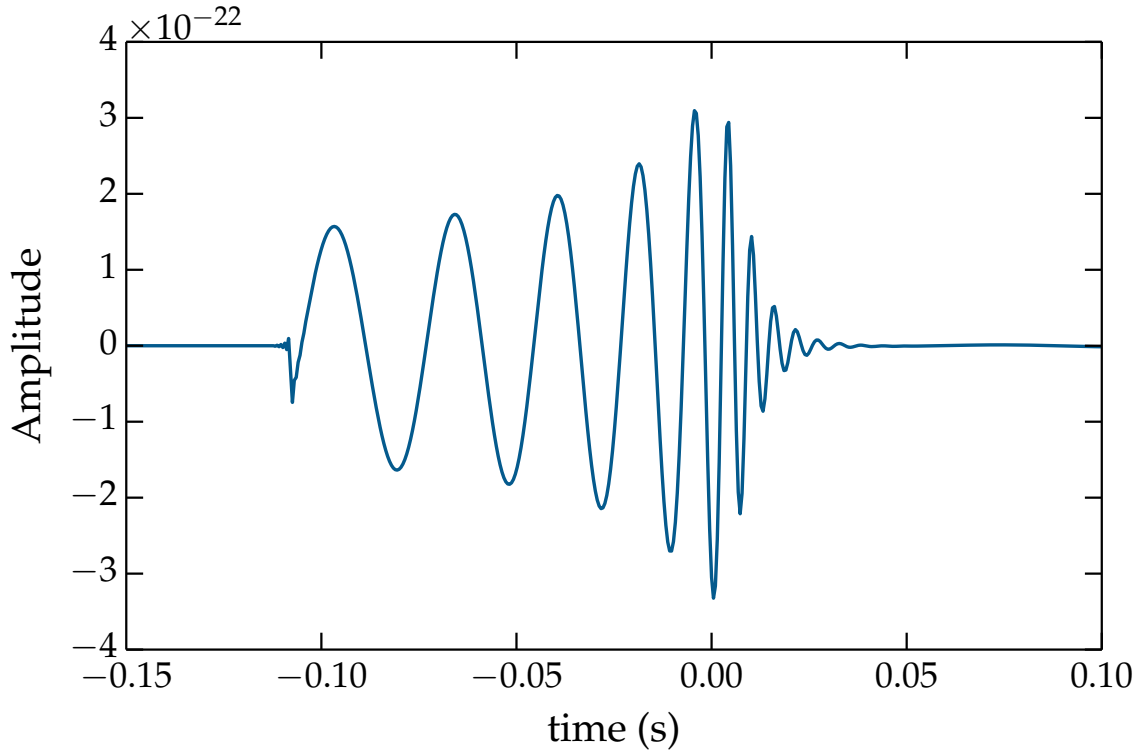

Figure 1.2: An example of GWs from a non-spinning binary black hole merger, with two equal $100\,M_{\odot}$ black holes. As the two black holes inspiral towards each other the GW amplitude and frequency increases until the black holes merge at $t = 0$. This produces the characteristic chirp shape. After the merger the final black hole will ringdown. The measured waveform will allow us to determine the black holes mass and spin.

a search using a technique known as matched filtering [27, 28]. Matched filtering is a data analysis technique that matches signals of a known shape to the data. This is achieved by correlating the output of the data with a large number of waveforms, known as templates, calculated with different source parameters such as mass and spin. Two different matched filter CBC searches exist that use the same set of templates but differ in their implementation [29, 30, 31]. Given a signal in the data, the searches look for the template that produces the largest signal to noise ratio (SNR). The optimal SNR ρ is given by the equation,

$$\rho = 2\left(\int_0^{\infty} \frac{|\tilde{h}(f)|^2}{S_h(f)} df\right)^{\frac{1}{2}}, \tag{1.2}$$

where $S_h(f)$ is the noise power spectral density (PSD), and h is the GW amplitude.

An approximation of the amplitude of a GW binary system is given by,

$$h = \frac{2G\mathcal{M}}{c^2 D_L}\left(\frac{\pi G\mathcal{M}f}{c^3}\right)^{\frac{2}{3}}, \tag{1.3}$$

where D_L is the luminosity distance, f is the GW frequency, which is twice the orbital frequency, and $\mathcal{M}$ is the chirp mass. The chirp mass is given by,

$$\mathcal{M} = \frac{(m_1 m_2)^{\frac{3}{5}}}{(m_1+m_2)^{\frac{1}{5}}} = \frac{c^3}{G}\left[\frac{5}{96}\pi^{-8/3} f^{-11/3}\dot{f}\right]^{3/5}, \tag{1.4}$$

where m_1 and m_2 are the masses of the two components of the binary, f is the frequency and $\dot{f}$ is the frequency derivative. The chirp mass can be determined directly from a GW detection as it depends only on the frequency and frequency derivative. The dimensionless spin of a binary system in given by,

$$a = \frac{c}{G}\frac{S}{m^2}, \tag{1.5}$$

where S is the spin angular momentum and m is the mass. The effective spin parameter is then given by,

$$\chi_{\text{eff}} = (m_1 a_1 + m_2 a_2)/(m_1+m_2).\frac{L}{|L|}, \tag{1.6}$$

where 1 and 2 are each component of the binary, and L is the orbital angular momentum. The χ_{eff} parameter can take values between -1 when both black holes have maximal spins anti-aligned with respect to the orbital angular momentum, and $+1$ when they have maximal aligned spins. To fully describe the binary system, other parameters can be measured, such as, the luminosity distance D_L, right ascension, declination, eccentricity and source orientation.

The waveform of GW150914 was loud enough that it was possible to visibly see it in the data. It was produced by two black holes with masses around $36\,\mathrm{M}_\odot$ and $29\,\mathrm{M}_\odot$. The dimensionless spin magnitude of the more massive black hole was measured to be < 0.7. The final black hole had an approximate mass of $62\,\mathrm{M}_\odot$ and spin 0.67 [32]. The second detection, GW151226, had smaller masses of around $14.2\,\mathrm{M}_\odot$ and $7.5\,\mathrm{M}_\odot$, and an approximate final black hole mass of $20.8\,\mathrm{M}_\odot$. It was determined that at least one black hole has a spin bigger than 0.2 [19]. As well as short duration GW signals from compact binaries, it is possible that GWs may be detected from other less understood sources.

1.2.4 Bursts

A burst is a GW signal with an unknown waveform. This may be due to unknown or complicated physics, or the source may be something totally unpredicted. As the waveform of a GW burst signal is unknown, it is not possible to use matched filtering to search for this type of signal. Searches for GW bursts typically search for excess power that occurs coherently between multiple detectors [33, 34, 35, 36]. The burst searches make minimal assumptions about the source, and use a sine Gaussian or sine Gaussian wavelets to model the GW signal in the data. Possible astrophysical sources of burst signals could be gamma-ray bursts [37], black hole or neutron star mergers with high mass ratios or eccentricity [38], cosmic strings [39], and core-collapse supernovae (CCSNe) [40]. In this thesis, we focus on CCSN bursts in particular. Burst searches can be sensitive to CBC sources, and were the first to detect GW150914 [41].

There are two independent searches for all-sky generic bursts, coherent Waveburst (cWB) [35, 36] and omicron-LALInference-Burst (oLIB) [34]. Another burst tool BayesWave [33] is used as a follow-up analysis of candidate events identified by cWB. The cWB algorithm has been searching for GW signals in LIGO data since 2004, and can provide a first estimation of source parameters within minutes of the signals arrival time. First, cWB whitens the data and converts to the time-frequency domain using the Wilson-Daubechies-Meyer wavelet transform [42]. Data from multiple detectors are then combined coherently to obtain a time-frequency power map. A signal is identified as a cluster of time-frequency data samples with power above some noise threshold. The signal waveforms in both detectors can then be reconstructed using a constrained likelihood method [43].

Even with no knowledge of the source of a GW signal, it is still possible to estimate some of the source parameters. Searches for GW bursts typically give estimations of the duration, amplitude and frequency of the source. An estimation of the sky position is given by measuring the difference in arrival time between different detectors [44]. If the distance to the source is known, perhaps through an electromagnetic counterpart, then it is possible to estimate the energy of the source. Assuming the signal is narrowband and the emission is isotropic, the GW energy is given by,

$$E_{GW} = \frac{\pi^2 c^3 d^2 f^2 h_{rss}^2}{G}, \tag{1.7}$$

where d is the distance to the source, f is the frequency and h_{rss} is the root sum squared amplitude.

A detection of a CCSN signal is an example of a good multi-messenger burst source. In 1934, Baade and Zwicky proposed that CCSNe are massive stars, $8 - 100\,M_{\odot}$, that collapsed into neutron stars when the star is no longer able to gravitationally support itself [45]. Type Ia supernovae occur when mass is accreted onto a White Dwarf, and do not emit GWs in the frequency range of ground based detectors. CCSNe collapse to a neutron star or black hole, and are some of the brightest known electromagnetic and neutrino events, making CCSNe good potential multi-messenger GW sources.

The GWs are emitted from deep inside the core of the CCSN, which may allow a GW detection to measure parameters that cannot be determined with electromagnetic radiation. GWs from non-rotating and rotating core-collapse may be observable throughout the Milky Way and the Large Magellanic Cloud (LMC) [46]. As this is a small distance compared to the sensitivity range for CBC sources, the rate for CCSN GW detections is low at around $\lesssim 2 - 3$ CCSNe per 100 yr [47, 48, 49, 50]. No GW detections were made in the first targeted cWB search for CCSNe [51]. The physics behind CCSN is still not well understood, and the exact GW waveform of these signals is unknown. The physical processes occurring in CCSNe are incredibly difficult to model, and so even state of the art simulations require a lot of computing time, do not include all of the required physics, or are ended prematurely resulting in only partial GW waveforms. Some of the latest waveform simulations are discussed later in this thesis, in Section 4.2.1 and Section 4.2.2.

1.3 Gravitational-Wave Detectors

GW experimental science was pioneered by Joseph Weber in the early 60's [52]. Weber attempted to measure GWs with a detector known as a bar antenna. The bar antenna was an aluminium cylinder, which was 2 meters long and one meter in diameter, contained in a vacuum chamber. A passing GW will change the length of the bar and can be detected if the frequency of the GW is close to the bars resonant frequency. Crystals on the bar will produce a current if the bars resonant

modes are excited. Weber claimed to have detected a GW signal from a CCSN [53], but his claims were not accepted as other groups failed to reproduce his results. Modern bar detectors are at lower temperatures to help improve their sensitivity, however, they are only sensitive to narrow frequency bands around their resonant frequencies.

Modern GW detectors use interferometry to detect GW signals. Laser light is split by a central beam splitter and travels down two perpendicular arms. At the end of the arms, the light is reflected by mirrors and travels back down the arms into the detector output. A single test mass cannot be used to detect GWs, because of the equivalence principal, which states that it is impossible to distinguish a uniform gravitational field from uniform acceleration in empty space. Since a freely falling reference frame for one mass can always be chosen so that the mass remains at the origin, to detect GWs the relative position of at least two freely falling test particles is needed. As a GW passes into the page, the arms will undergo a tiny change in length. The change in length is then measured as GW strain h in the detector output as,

$$h = \frac{\Delta L}{L}\,, \tag{1.8}$$

where L is the detector arm length. The detectors are most sensitive at the frequency where the gravitational wavelength is roughly the distance probed by the time of flight of the lasers $f = c/2\pi L$.

The sensitivity of the detector depends on the direction of the source. The GW strain measured in the detector is given by,

$$h(t) = F_+ h_+ + F_\times h_\times\,, \tag{1.9}$$

where h_+ and $h_\times$ are the two GW polarizations, and F_+ and $F_\times$ are the antenna patterns, shown in Figure 1.3, which describe the sensitivity of the detector in different directions. They can be described by the equations,

$$F_+ = \frac{1}{2}(1+\cos^2\theta)\cos 2\phi\cos 2\psi - \cos\theta\sin 2\phi\sin 2\psi\,, \tag{1.10}$$

$$F_\times = \frac{1}{2}(1+\cos^2\theta)\cos 2\phi\sin 2\psi + \cos\theta\sin 2\phi\cos 2\psi\,, \tag{1.11}$$

where θ is the local polar angle, ϕ is the local azimuthal angle and ψ is the polarization angle of the source. The detectors have some sensitivity in almost all directions

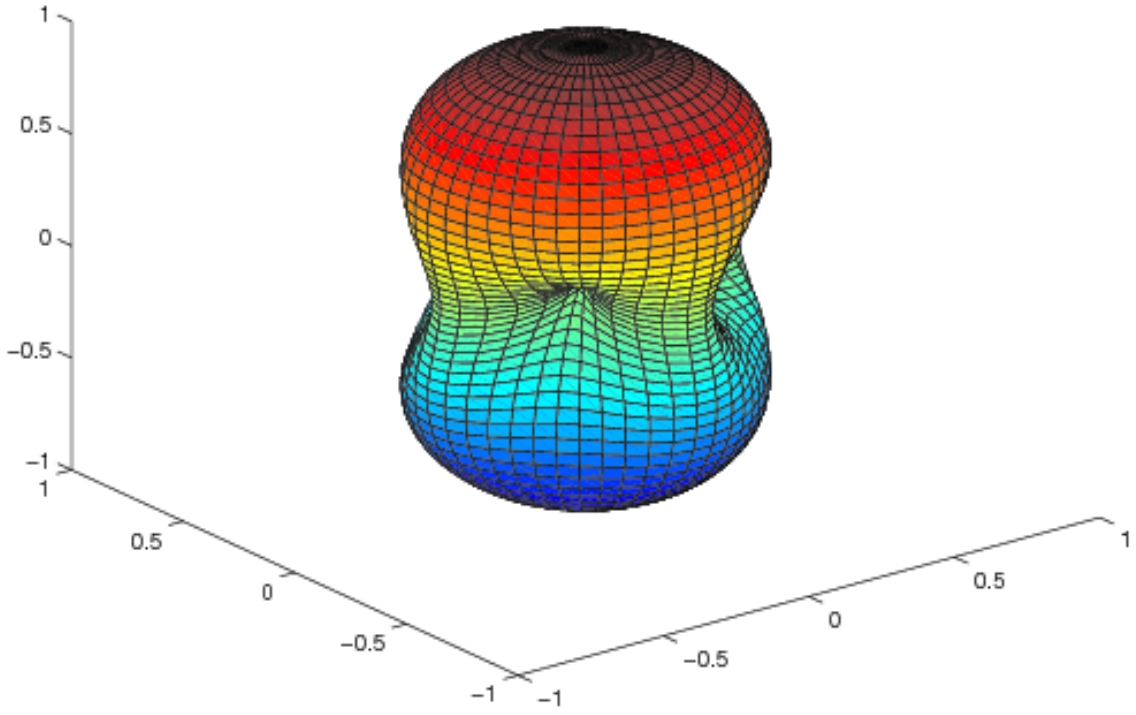

Figure 1.3: The antenna pattern of a GW interferometer. The antenna pattern is a measure of how sensitive a detector is in each direction. The detectors have some sensitivity in almost all directions, and are most sensitive in the directions above and below the detector arms. Figure reproduced from [20].

and are most sensitive in the directions above and below the detector arms.

Current ground based GW interferometers include GEO, a German detector with 600 m long arms [54], AdVirgo, an Italian detector with 3 km long arms [12, 3], and aLIGO, which consists of two 4 km detectors in Livingston, Louisiana and Hanford, Washington [1]. Future planned GW detectors include the Einstein telescope [55], an underground detector that is expected to be 100 times more sensitive than current ground based detectors, and KAGRA [56], a detector currently under construction in the Kamioka mine in Japan. KAGRA will have 3 km long arms with cryogenic mirrors to reduce the thermal noise, and reduced seismic noise due to its underground location.

The Laser Interferometer Space Antenna (LISA) [24], will be the first GW detector in space, and will be sensitive to higher mass sources than ground based detectors, such as, super massive black holes. The LISA pathfinder mission [57]

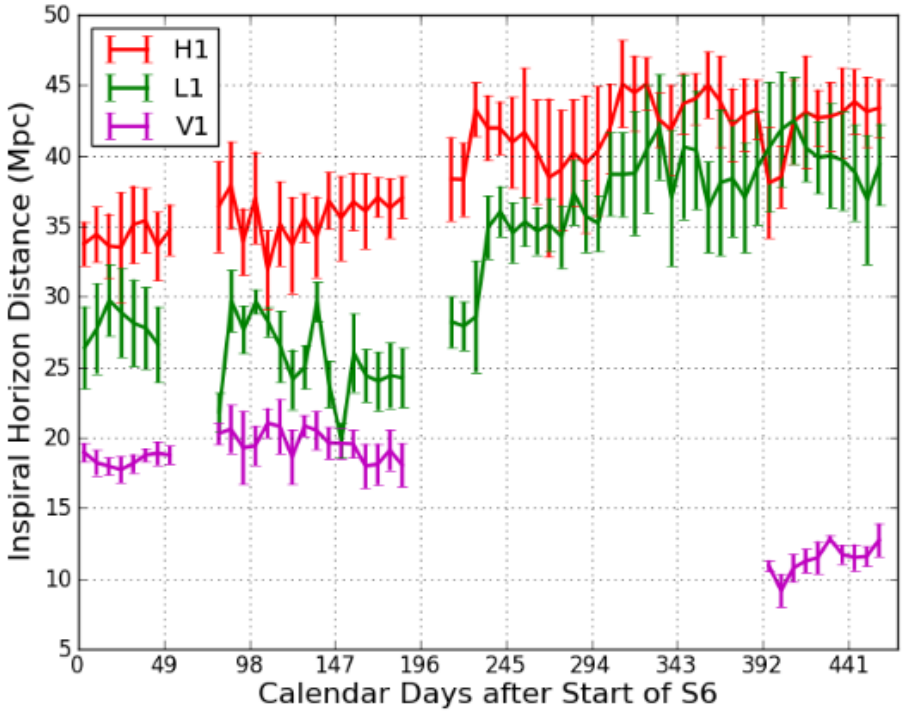

Figure 1.4: The inspiral horizon distance during the Initial LIGO and Virgo S6 and VSR2/3 runs. The average inspiral horizon distance is shown for each week with error bars the correspond to the standard deviation for that week. The Hanford detector was the most sensitive reaching distances of up to 45 Mpc towards the end of the science run. Figure reproduced from [59].

is designed to test the technology that is needed for the LISA detector. LISA pathfinder has two test masses, and was launched in December 2015. The LISA pathfinder results were five times more sensitive than expected [58], and has demonstrated the technology needed for the future LISA mission.

1.3.1 Initial Detectors

The construction of the Virgo detector started in 1996. The first Virgo Science Run, VSR1, occurred in 2007, and the second Virgo Science Run, VSR2, occurred in 2009. The LIGO detectors were built in 1995 with the first Initial LIGO science run starting in 2002. In 2007, the LIGO detectors completed a two year long science run, S5, during which one year of science quality data was collected at design sensitivity. In Initial LIGO, the lower noise limit was from motion of the mirrors, and the higher noise limit was created by shot noise. After S5, LIGO went offline to begin upgrade to Enhanced LIGO. Enhanced LIGO had more powerful lasers than Initial LIGO, with an increase from 10 W to 35 W. Enhanced LIGO was

twice as sensitive as Initial LIGO. The first Enhanced LIGO run, S6, began in 2009 at the same time as the Virgo VSR2 run.

The inspiral horizon distance, which is defined as the distance at which an optimally located and oriented binary system would give expected SNR equal to 8, during the LIGO S6 and Virgo VSR2/3 runs is shown in Figure 1.4. The LIGO Hanford detector was the most sensitive reaching distances of up to 45 Mpc towards the end of the science run. The initial detectors did not find any GWs [60, 61], however, upgrades to the detectors began in 2008, with the advanced detectors expected to be a factor of 10 more sensitive than the initial detectors, with a 1000 times larger source volume.

1.3.2 Advanced Detectors

The aLIGO upgrades finished in 2015, and O1 began in September 2015. A diagram of the aLIGO detectors is shown in Figure 1.5. The light from the Nd:YAG 1064 nm laser first travels to the input mode cleaner, which improves the beam mode quality by filtering out higher order spatial modes. The light is then split by the beam splitter and travels down the two perpendicular detector arms. The Fabry-Perot cavities build up power in each arm that increases the effective response of the detectors to a change in phase that would be produced by a GW. The GW will create a phase shift that changes the interference pattern when the light recombines at the detector output. Some of the aLIGO detectors expanded detection volume comes from better sensitivity at low frequencies, moving the lower noise cutoff from 40 Hz to 10 Hz.

1.3.3 Noise Sources

The sensitivity of aLIGO is limited by multiple sources of noise from the hardware subsystems and the environment. An overview of the limiting noise sources is shown in Figure 1.6. The low frequency sensitivity of the detectors ($\lesssim$ 10 Hz) is limited by the effects of seismic noise, due to motion in the ground, which propagates through the suspensions. Thermal noise due to Brownian motion in the optical coatings is the most dominant noise source in the most sensitive frequency range of

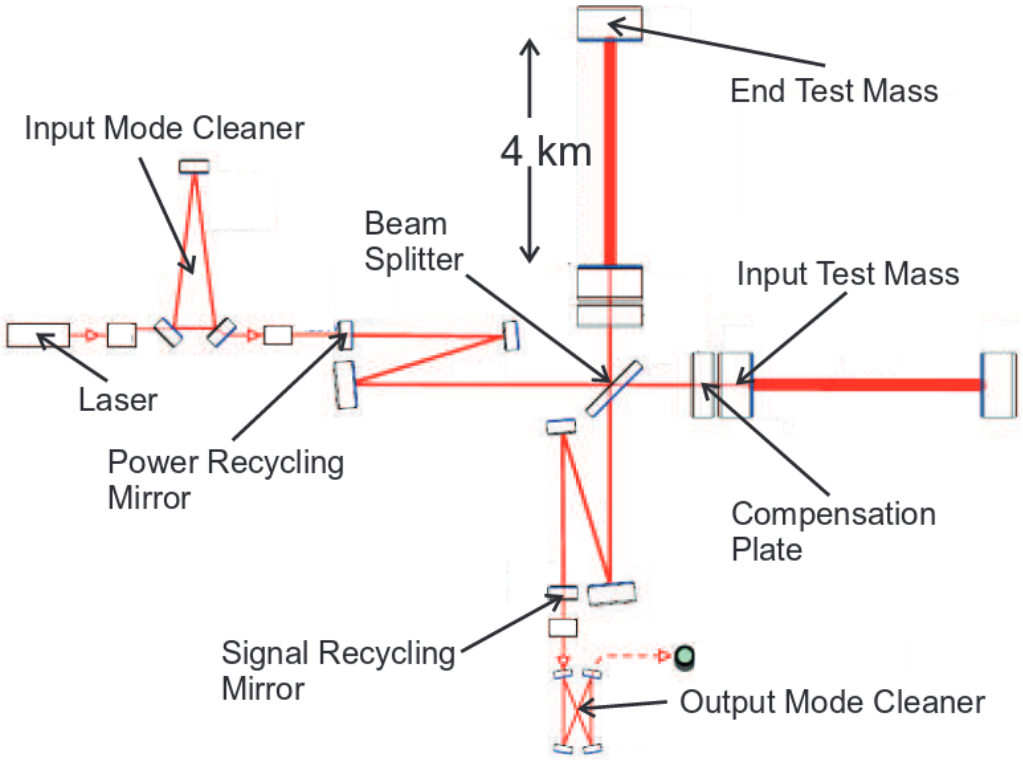

Figure 1.5: A diagram of the aLIGO GW interferometers. The light from the laser first travels to the input mode cleaner that improves the beam mode quality by filtering out higher order spatial modes. The light is then split by the beam splitter and travels down the two perpendicular detector arms. The Fabry-Perot cavities build up power in each arm to increase the effective response of the detectors to a change in phase produced by a GW moving into the page. The GW will create a phase shift that changes the interference pattern when the light recombines at the detector output. Figure reproduced from [1].

the instruments. At frequencies higher than $\sim 150\,\mathrm{Hz}$, shot noise, due to random fluctuations in the arrival time of the photons at the photo-detector, is expected to be the dominant noise source. Shot noise can introduce random fluctuations in the interference pattern that may mimic a GW signal. Shot noise improves with increased laser power. However, radiation pressure noise, due to the pressure of photons hitting the end mirrors, will also increase with increased laser power. Gravity gradient noise due to fluctuations in the local gravitational field is another source of noise for the aLIGO detectors.

Another limiting noise source for GW advanced detectors are instrumental and environmental disturbances that produce non-astrophysical short duration transients in science data, called *glitches*. Glitches increase the false alarm rate of searches, and decrease the detectors' duty cycles. The success of the advanced detectors requires a huge effort in commissioning and detector characterization [62, 63].

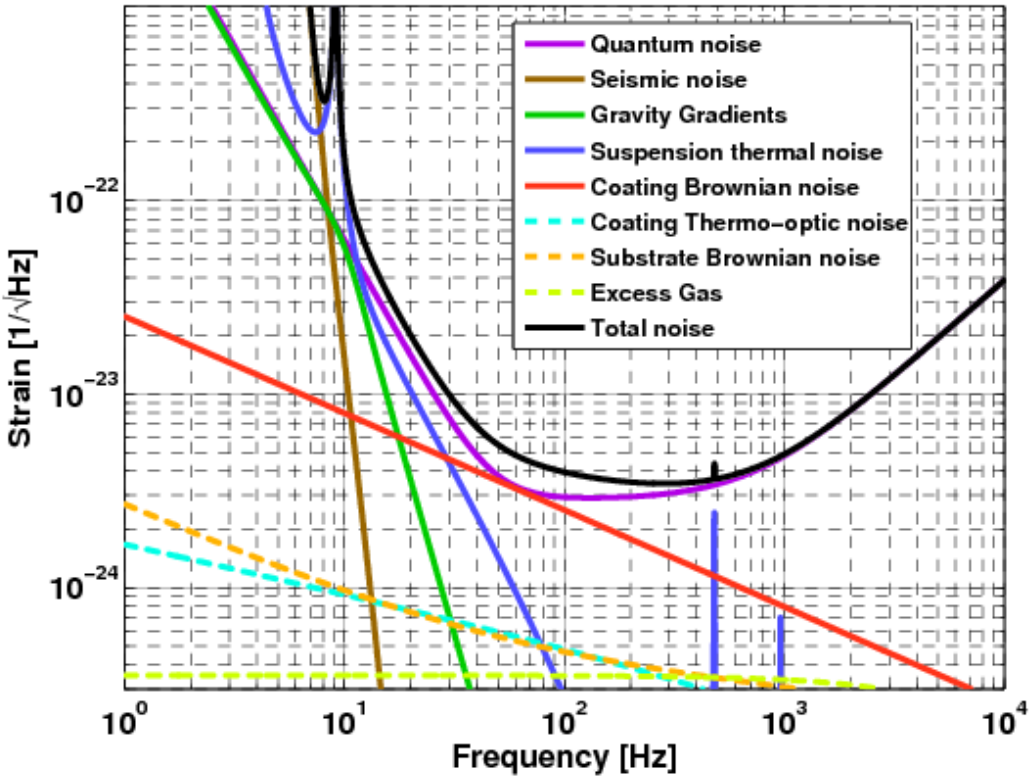

Figure 1.6: The contribution of different noise sources to the sensitivity of the aLIGO detectors. The different colours show the different noise sources, with quantum noise being the limiting noise source. Thermal noise due to Brownian motion in the optical coatings is the most dominant noise source in the most sensitive frequency range of the instruments, at a few hundred Hertz. Figure reproduced from [1].

Over 200,000 auxiliary channels of data are used to monitor the detectors behaviour and environment. These channels can be used to identify the cause of glitches if there are coupling mechanisms between the auxiliary channels and the GW strain data.

If it is not possible to remove the source of the glitch, then auxiliary channels can be used to create data quality *vetoes* [64, 65, 6]. Vetoes remove data where transients are coincident with auxiliary channels that are not sensitive to GWs. Vetoes are not an ideal method to eliminate glitches, because they reduce the duty cycle of the instruments. Data quality flags can be applied to data when events occur that have been known to create noise couplings with the GW strain in the past. DQ flags were used in the initial detector science runs, and were highly effective in increasing the sensitivity of searches [6]. The use of DQ flags in the Virgo VSR2 run gave an $\sim 30\%$ increase in the volume of which Virgo was sensitive to CBC sources [63], and $\sim 5\,\mathrm{Mpc}$ increase in the detection range of an SNR 8 binary neutron star system in

the Initial LIGO detectors [6].

GW searches can have search specific procedures to limit the impact of glitches. In searches for CBC signals, a technique known as *gating* is used to roll the GW data smoothly to zero at times when significantly loud glitches occur. In searches for GW bursts, measuring how coherent a signal is between different detectors can be used to reject signal candidates created by glitches. An extensive study of the glitches, which occurred in the data containing the detections, was carried out for the validation of the signals [66]. As the advanced detector network approaches its design sensitivity, the number of detections is expected to increase. Adding more detectors to the network increases the number of possible noise sources and the time it will take to identify their origin. Adding more detectors will increase the significance of detections, but glitches which occur in any one detector will limit the joint analysis time for the network. Understanding the sources of glitches in the detectors will become increasingly more important with a latency of a few hours, so that the data quality can be improved during the joint observing runs.

Multiple different types of glitches have been identified through their common origin, or by their time-frequency morphology. Some examples are shown in later chapters, for example, in Figure 3.2 and Figure 3.4. If a glitch type is not correlated with any auxiliary channel that is not sensitive to GWs, then it will not be removed by DQ vetoes, and their origin is particularly difficult to identify. The background for GW searches during O1 was estimated by time shifting the data between the interferometers to measure the number of coincident background noise triggers. Therefore, the significance of a GW detection during O1, and in future observing runs, has been limited by the number of glitches.

Chapter 2

Glitch Characterization

2.1 Introduction

The aLIGO and AdVirgo detectors are designed to detect GWs of various astrophysical origin [67]. The non-Gaussian, non-stationary nature of advanced detector noise produces glitches, which affect the sensitivity of searches, and can be mistaken as GW detections, in particular for un-modelled sources. To determine if a potential GW source is astrophysical, the signal is required to be coincident between two or more GW detectors. The high rate of glitches means that it is possible for accidental coincidence between the detectors to occur. Glitch classification and categorization can provide valuable clues for identifying the source of the glitches, and lead to their elimination. In initial LIGO and Virgo science runs, this classification was performed by visual inspection of the glitches' time series and/or spectrograms. Visual inspection of individual glitches proved to be a slow and inefficient method in attempts to categorize glitches during the S6 LIGO science run. Faster and more reliable techniques for the classification of glitches was needed. This can only be achieved with automatic glitch classification algorithms running in low-latency as data is collected [68].

In this chapter, we develop a method called PC-LIB, designed for the fast classification of advanced detector glitches, and test the method on simulated data sets. The chapter in structured as follows: In Section 2.2, we introduce the algorithm used for glitch classification. In Section 2.3, we describe other methods used for

glitch classification, which we use for a comparison study later in the chapter. In Section 2.4, we created three different data sets, which are specifically designed to test the efficiency of the algorithms in classifying glitches with different waveform morphology or frequency content. In Section 2.5, we describe the PC-LIB results, and compare them to results from other classification methods. A summary and discussion is given in Section 2.6.

2.2 PC-LIB

The PC-LIB glitch classification algorithm is implemented in C, and is a part of the LIGO data analysis software package, LSC Algorithm Library (LAL) [69]. More specifically, we use the `LALInference` package [70, 44, 34], which is designed for parameter estimation of GW signals, and can be used for model selection, or to produce posterior distributions for the parameters of a signal, such as the sky location [71, 44]. `LALInference` typically uses CBC waveforms or a sine Gaussian as a signal model. For glitch classification, we have adapted `LALInference` to include a signal model that is created from a linear combination of principal components (PCs). An overview of the classification procedure implemented in PC-LIB is given in Figure 2.1. When the signal models have been created, Bayesian model selection can be applied to determine the correct glitch type.

2.2.1 Bayesian Inference

For a given set of data D and hypothesis H Bayes theorem is given by,

$$\text{prob}(H|D) = \frac{\text{prob}(D|H)\text{prob}(H)}{\text{prob}(D)}, \tag{2.1}$$

where $\text{prob}(H|D)$ is the posterior probability, which represents what we know about the hypothesis from the given data, $\text{prob}(D|H)$ is the likelihood function that represents what we know from the data, and $\text{prob}(H)$ is the prior, which represents what we know about the hypothesis before any analysis of the data.

The data from GW interferometers is a set of time series samples d, sampled

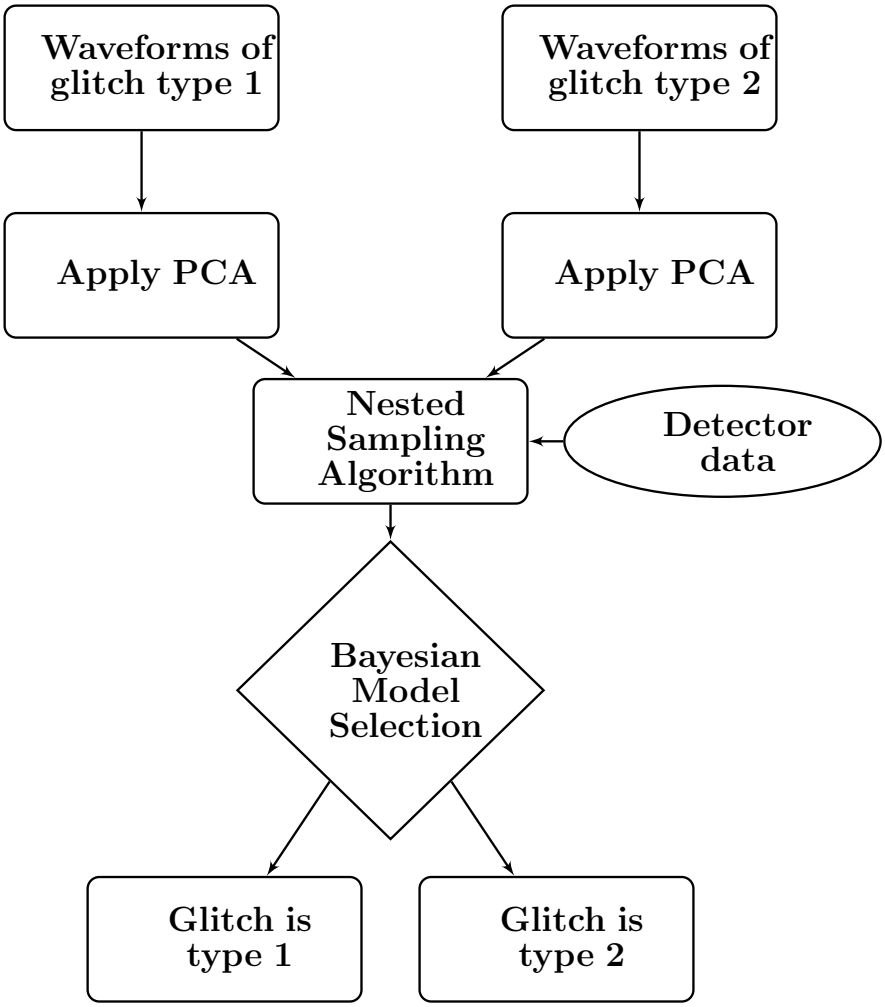

Figure 2.1: An outline of the classification procedure implemented in the PC-LIB algorithm. First, PCA is applied to the time series waveforms of different types of glitches. A linear combination of the PCs can then be used as signal models for different glitch types. Bayesian model selection is then applied to determine the correct type of glitch. Figure reproduced from [7].

uniformly in time t. For the noise model, we assume Gaussian stationary noise with a certain power spectral density (PSD), $S_n(f)$, which is estimated from 100 seconds of data adjacent to the time of interest. The likelihood function for the noise model, for all likelihood calculations in this thesis, is the product of Gaussian distributions in each frequency bin,

$$p(d|H_N, S_n(f)) = \exp \sum_i \left[-\frac{2|\tilde{d}_i|^2}{TS_n(f_i)} - \frac{1}{2}\log(\pi T S_n(f_i)/2) \right], \tag{2.2}$$

where T is the duration of the analysis segment, and $\tilde{d}_i$ is the discrete Fourier

transform of d_i,

$$\tilde{d}_i = \frac{T}{N}\sum_k d_k \exp(-2\pi ijk/N). \tag{2.3}$$

When a signal h is present in the data, the likelihood then becomes,

$$p(d|H_N, S_n(f), \theta) = \exp\sum_i \left[-\frac{2|\tilde{h}_i(\theta) - \tilde{d}_i|^2}{TS_n(f_i)} - \frac{1}{2}\log(\pi T S_n(f_i)/2)\right], \tag{2.4}$$

where θ is the parameters of the signal h. In later chapters of this thesis we need to analyse the data from a network of detectors coherently. If the noise in each detector is uncorrelated then it is possible for a coherent network likelihood to be the product of likelihoods from the individual detectors,

$$p(d_{HLV}|H_S S_{nHLV}(f)) = \prod_{i\epsilon H,L,V} p(d_i|H_S, S_{ni}(f)), \tag{2.5}$$

where H,L and V are the three different GW interferometers [70].

Comparisons between two competing models M_i and M_j can then be made by calculating the odds ratio,

$$O_{i,j} = \frac{p(M_i)}{p(M_j)}\frac{p(D|M_i)}{p(D|M_j)} = \frac{p(M_i)}{p(M_j)}B_{i,j}\,, \tag{2.6}$$

where the priors cancel out if each model has the same prior, and $B_{i,j}$ is the Bayes factor given by the ratio of the evidences,

$$B_{i,j} = \frac{p(D|M_i)}{p(D|M_j)}\,, \tag{2.7}$$

where $p(D|M_i)$ is the evidence for model M_i given data D, and $p(D|M_j)$ is the evidence for model M_j given data D [72]. The evidence for each model is calculated by integrating the likelihood $p(D|\theta, M)$, multiplied by the prior $p(\theta|M)$, over all parameter values θ,

$$p(D|M) = \int_\theta p(\theta|M)p(D|\theta, M)d\theta\,. \tag{2.8}$$

Example parameters of a GW detection are the sources mass, spin, distance and sky position. For a large number of model parameters the evidence integral becomes difficult. This problem is solved using a technique called nested sampling [72, 73].

Nested Sampling

Nested sampling is a numerical technique that can be used to estimate evidence integrals [72, 73]. It can produce posterior distributions on the parameters of a model. A diagram explaining how nested sampling works is shown in Figure 2.2. The nested sampling algorithm calculates the likelihood of a selected sample of points in the models parameter space. First, the likelihood is calculated for a set of random points that are distributed over the entire prior. Then the worst point, which has the smallest likelihood and largest prior mass is selected. The worst points likelihood and prior mass values are then used as the new limiting values, and the worst point is discarded. A new point is then generated inside the new limiting values using Markov Chain Monte Carlo (MCMC) techniques [72]. This is repeated so that it iterates inwards in prior mass and upwards in likelihood until the region of the prior mass with the highest likelihood is found. The evidence integral can then be expressed as,

$$Z = \int_{\theta} p(\theta|M)p(D|\theta, M)d\theta \,, \tag{2.9}$$

$$Z \approx \sum_{i=1} p(D|\theta_i, M)\omega_i \,, \tag{2.10}$$

$$Z \approx \sum_{i=1} \mathcal{L}_i\omega_i \,, \tag{2.11}$$

where the weight ω is given by $\omega_i = p(\theta_i|M)d\theta$ and represents the fraction of the prior distribution represented by the ith sample, and $\mathcal{L}_i = p(D|M, \theta_i)$ is the likelihood. If a signal is present, the evidence integral will be dominated by a small region of the prior with the highest likelihood, concentrated in a fraction $\exp(I)$ of the parameter space. I is called the information in the data, and is given by,

$$I = \sum p(\theta|D, M) \log \frac{p(\theta|D, M)}{dX} d\theta d\theta \,. \tag{2.12}$$

I represents the amount of information in the posterior relative to the prior.

Now that the evidence integrals can be solved, PC-LIB can calculate a signal verses noise Bayes factor, $B_{S,N}$, for each possible type of glitch. Taking the log of the Bayes factor gives,

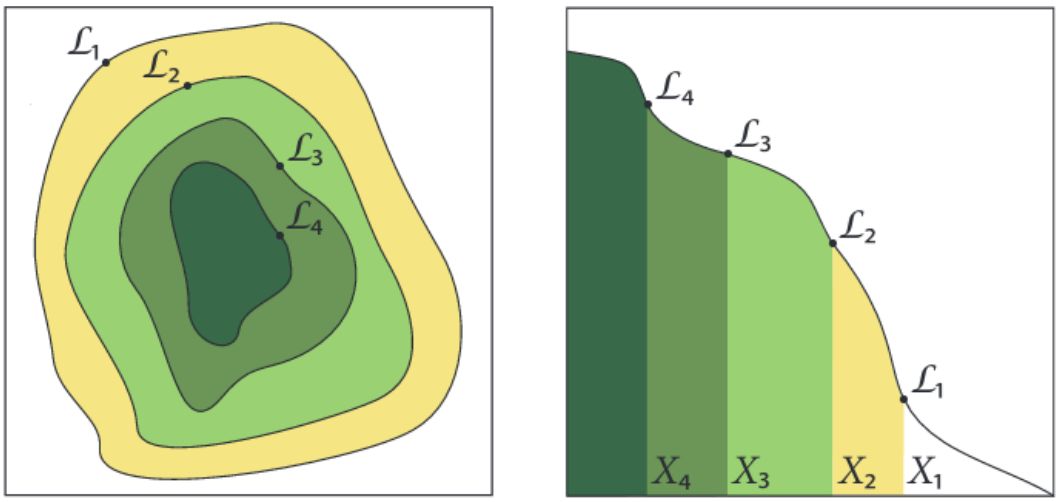

Figure 2.2: Each sample in the set of live points can be thought of as lying on a contour line of equal likelihood value, where $\mathcal{L}$ represents the likelihood and X represents the prior mass. First, the likelihood is calculated for a set of random points that are distributed over the entire prior. Then the worst point, which has the smallest likelihood and largest prior mass is selected. The worst points likelihood and prior mass values are then used as the new limiting values, and the worst point is discarded. A new point is then generated inside the new limiting values. Figure reproduced from [74].

$$\log B_{S,N} = \log[p(D|M_S)] - \log[p(D|M_N)]\,, \tag{2.13}$$

where M_S and M_N are the signal and noise models, respectively. To compare two different glitch models, M_{type1} and M_{type2}, the signal vs. noise Bayes factors can be subtracted to obtain a new log Bayes factor that determines the glitch type as,

$$\log B_{type1,type2} = \log B_{S_{type1},N} - \log B_{S_{type2},N}\,. \tag{2.14}$$

If the glitch belongs to type 1 then $\log B_{type1,type2}$ will be positive, and if the glitch belongs to type 2 then $\log B_{type1,type2}$ will be negative.

To adapt `LALInference` for the classification of glitches, we adopt the Principal Component Analyses (PCA) approach taken by Logue *et. al.* [75], in their analysis of the explosion mechanism of CCSN signals. We take the time series of the first fifty glitches of a known type, sampled at 4096 Hz, and apply a second order Butterworth high pass filter at 30 Hz. PCA is then applied to the glitch waveforms.

2.2.2 Basics of Principal Component Analysis.

Time series waveforms are used to construct an $m \times n$ data matrix $\mathbf{D}$, where n is the number of waveforms, and the rows of the matrix are the time series of the waveforms of length m. The ideal glitch waveforms for the PCA procedure are those that have a large enough amplitude to be clearly distinguishable from the rest of the background noise. However, as some glitches only occur with lower amplitudes it is not possible to only use loud glitches for all glitch types. The $m \times n$ data matrix $\mathbf{D}$ can be factored so that,

$$\mathbf{D} = \mathbf{U}\Lambda\mathbf{V^T}, \tag{2.15}$$

where $\mathbf{U}$ is an $m \times m$ matrix with columns given by the eigenvectors of $\mathbf{D}^T\mathbf{D}$, $\mathbf{V}$ is an $n \times n$ matrix with the eigenvectors of $\mathbf{D}\mathbf{D}^T$ as columns, and $\mathbf{\Lambda}$ is an $m \times n$ diagonal matrix. The rows of the matrix $\mathbf{U}$ are the PCs, which are ordered by decreasing eigenvalue absolute value. The diagonal values of $\mathbf{\Lambda}$ are the eigenvalues of the PCs. The data matrix $\mathbf{D}$ can be projected on the PC basis as,

$$\mathbf{S} = \mathbf{D}\ \mathbf{U}\,. \tag{2.16}$$

The $m \times n$ matrix $\mathbf{S}$ is called the Coefficient Matrix. The coefficients of the expansion of the original data set w.r.t. the new basis are called PC coefficients. Waveforms with different features are expected to have different PC coefficients. Since the PC eigenvectors are ordered by decreasing eigenvalues, the first few coefficients typically identify the most important features of the waveforms. The waveforms can be accurately reconstructed from a linear combination of the first k PCs, weighted by their respective coefficients β,

$$h_i = A\sum_{j=1}^{k} U_j\beta_j\,, \tag{2.17}$$

where A is an amplitude scale factor, and k is usually $\ll n$.

The amount variance of the data explained by each PC is defined as,

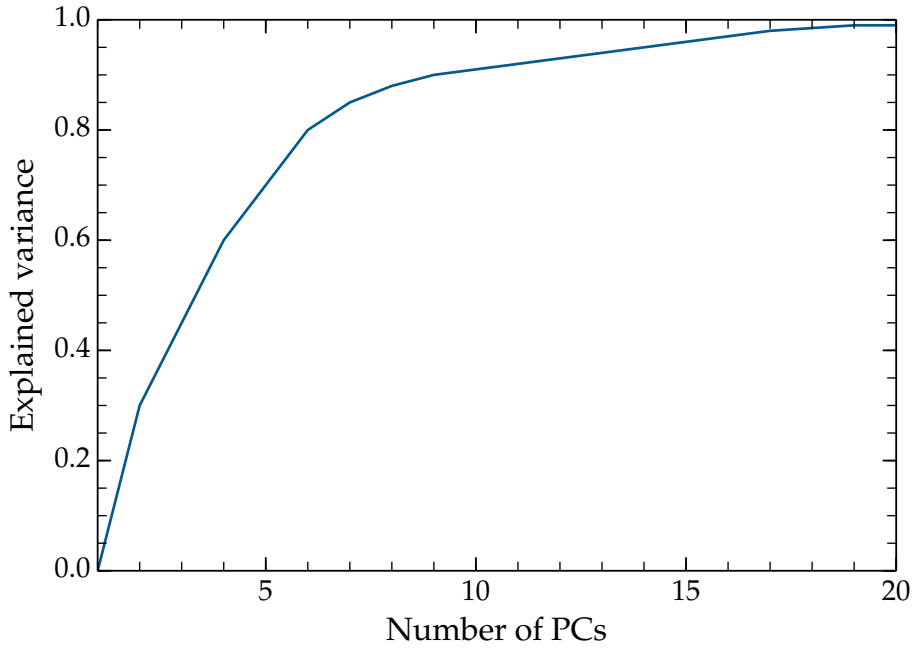

Figure 2.3: An example of how much variance of a data set is represented by each PC. The ideal number of PCs can be determined by setting a threshold on the variance, or by looking for changes in the variance curve, as the variance should increase at a slower rate when the ideal number of PCs is reached. Figure reproduced from [7].

$$v(k) = \frac{1}{\Lambda} \sum_{i=1}^{k} \Lambda_i \,, \qquad \Lambda = \sum_{i=1}^{n} \Lambda_i \,, \tag{2.18}$$

where Λ_i are the eigenvalues of the matrix $\mathbf{\Lambda}$. The explained variance $0 \leq v \leq 1$ measures the variation (dispersion) of the data set as a function of its dimensionality. An example of a variance curve is given in Figure 2.3. The number of PCs that are needed to describe the sample up to a given accuracy can be determined by setting a threshold on v, or plotting the variance and looking for changes in the curve. Therefore, PCA allows dimensional reduction of the data set.

A linear combination of the PCs, multiplied by the PC coefficients, is then used as the new signal model in PC-LIB for each different population of glitch. Bayesian model selection can then be used to determine the type of each new glitch that is detected in the data, using the different signal models for each glitch population. A flat, uniform prior is used for the PC coefficients for each glitch type. To calculate the minimum and maximum values for the PC coefficient priors, we use the method described by Logue *et. al.* [75] of projecting the glitch waveforms on to the PCs.

For glitches in real detector noise, an event trigger generator (ETG) is used

before running PC-LIB. ETGs typically search for excess power in individual interferometers and output the time, SNR, frequency, duration and other parameters of transients found in the data. PC-LIB uses Omicron, the main ETG used by the LIGO Scientific Collaboration's (LSC) detector characterization group [76, 77].

2.3 Other Classification Methods

Other methods for the classification of glitches have been developed. In this section, we give a brief description of those methods, and in later sections we carry out a study to compare their performance on real and simulated noise from advanced GW detectors.

2.3.1 Principal Component Analysis for Transients

Principal Component Analysis for Transients (PCAT) is a python-based algorithm based on the use of PCA [78] to identify and classify glitches in aLIGO data channels. A summary of the classification procedure implemented in the PCAT algorithm is given in Figure 2.4. PCAT uses the time-sampled values of the aLIGO h(t) strain as PCA input variables. The PCs are used to analyse the time variability of the data and reconstruct the properties of the glitches.

Pre-processing.

The raw time series (sampled at 16384 Hz) is first split into 32 second-long segments with a 50% overlap, then down sampled to 8192 Hz, and high passed with a Butterworth 4th order filter with a 30 Hz cut-off frequency. The data are then whitened by multiplying the Fast Fourier Transform (FFT) of the time series by the inverse of the square root of the detector's noise PSD, which is computed using the median-mean average algorithm, as described in [27]. The whitened FFT is inverted, yielding the whitened time series, of which the first and last 8 seconds are discarded to avoid FFT artifacts at the edges. Glitches are identified when the channel amplitude exceeds a chosen threshold in units of the standard deviation

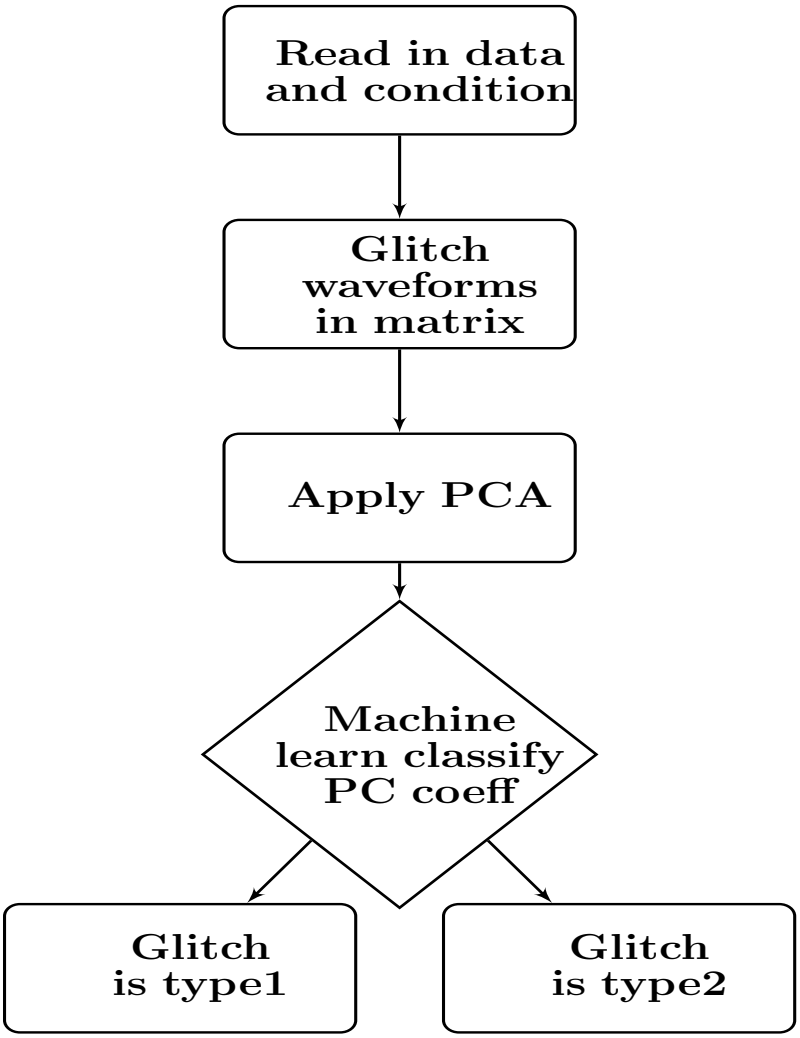

Figure 2.4: The classification procedure implemented in the PCAT algorithm. PCAT reads in the time series data and finds glitches above a certain SNR threshold. PCA can then be applied to the whitened time series of all the glitches found in the data. Different types of glitches live in different areas of the PC coefficient parameter space. A machine learning classifier is then applied to the the PC coefficients to determine the correct type of glitch. Figure reproduced from [7].

of the analysed 16 second segment. A value between 4.5 and 5 has been shown to maximize the efficiency in identifying glitches, while minimizing false positives. For each set of points above the threshold (triggers), the time series is sampled with a fixed-width interval around the trigger's maximum amplitude (typically corresponding to around 125 ms), and then rescaled to a maximum (absolute) amplitude equal to one. This step is required to properly compare the time series and identify the main features of different glitch families.

Classification.

Machine learning classification procedures can be supervised or unsupervised [79]. A supervised machine learning algorithm trains on a sample of correctly labelled data. An unsupervised classification procedure has no labelled training set of data. PCAT uses an unsupervised classification procedure, as we have no previously labelled data set on which to train the algorithm. PCAT uses the scikit-learn Gaussian Mixture Model (GMM) algorithm to cluster the PCA-reduced data [80]. The data are fit to a linear combination of multivariate Gaussian distributions. The number of these distributions (number of classes) is determined by minimizing the Bayesian Information Criterion (BIC) [81]. An important feature of the BIC algorithm is the calculation of a penalty score for each of the free parameters in the data set to avoid over-fitting.

Accurate classification of glitches requires a careful choice of the number of PCs. A low number of PCs typically results in insufficient information to characterize the data. A high number of PCs leads to the inclusion of Gaussian noise features in the reduced dataset, which results in poor performance of the clustering algorithm [82].

2.3.2 Wavelet Detection Filter and Machine Learning

WDF-ML consists of a event detection algorithm, Wavelet Detection Filter (WDF), followed by a Machine Learning (ML) classification procedure. WDF-ML is part of the Noise Analysis Package (NAP), a C++ library embedded in python, developed by the Virgo Collaboration [83].

Wavelet Detection Filter.

Wavelet-based algorithms are well tuned for the identification of glitches because they decompose the data into multiple time-frequency resolution maps. The efficiency in detecting glitches is linked to the similarities between the analysing wavelet and the waveforms of the glitches. As different wavelet types could better match different waveform morphologies, WDF-ML performs wavelet domain decomposition using different types of wavelet basis, including the Daubechies and Haar wavelets

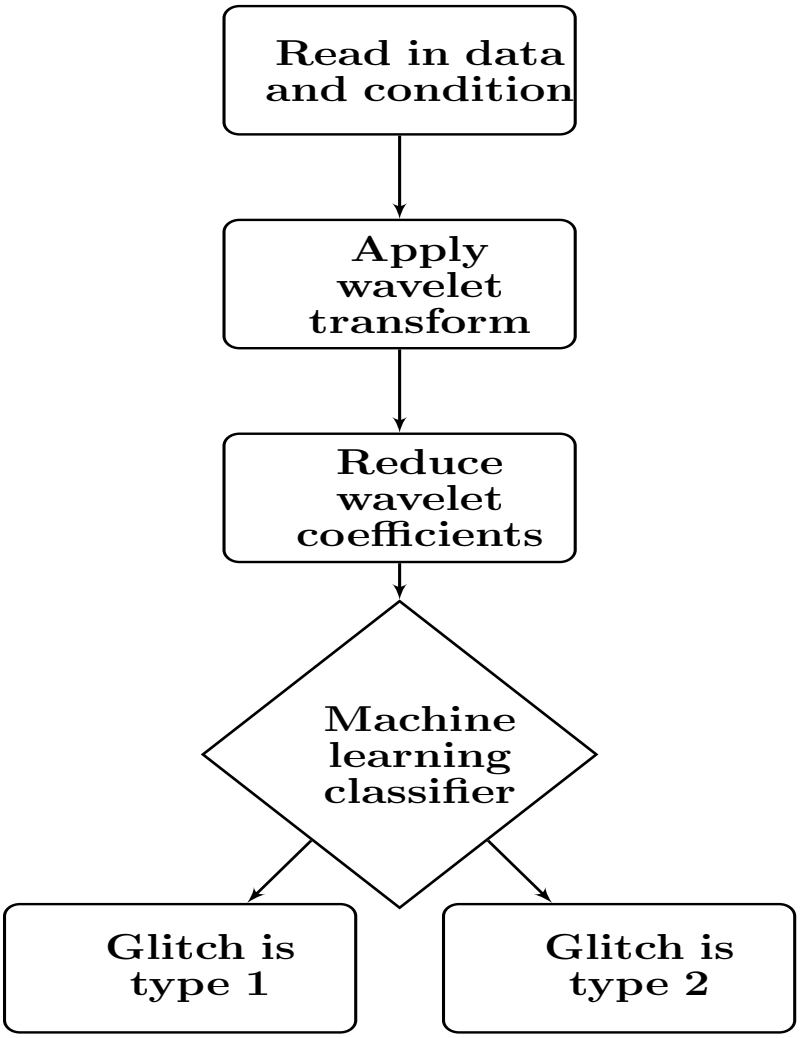

Figure 2.5: The classification procedure implemented in the WDF-ML algorithm. WDF-ML conditions the data and then applies a wavelet transform using multiple different types of wavelets. The wavelet coefficients are then reduced using data reduction techniques, such as PCA. A machine learning classifier is then applied to the reduced wavelet coefficients to determine the correct type of glitch. Figure reproduced from [7].

[84, 85].

A wavelet transform is similar to a Fourier transform. The Fourier transform sinusoidal waves are replaced by an orthonormal basis generated by translations (shifting) and dilations (scaling) of the mother wavelet,

$$\psi_{a,b}(t) = \frac{1}{\sqrt{b}}\psi\left(\frac{t-a}{b}\right), \tag{2.19}$$

where b is the scale and a is the translation. The wavelet transform of a signal $f(t)$

is defined as the projection of f on the wavelet basis,

$$Wf(a,b) = \langle f, \psi_{a,b} \rangle = \int_{-\infty}^{+\infty} f(t) \frac{1}{\sqrt{b}} \psi^* \left(\frac{t-a}{b} \right) \quad dt \,, \tag{2.20}$$

where ψ^* is the complex conjugate of the mother wavelet. The wavelet transform has a time frequency resolution that depends on the scale b. The time spread is proportional to b, and the frequency spread is proportional to the inverse of b. The discrete wavelet transform uses a discrete set of the wavelet scales and translations. This transform decomposes the signal into a mutually orthogonal set of wavelets.

Figure 2.5 shows an outline of the classification procedure implemented in the WDF-ML algorithm. The first five minutes of data are used to estimate the parameters for the whitening filter in the time-domain. The whitening procedure is based on a Linear Predictor Filter, whose parameters are estimated through a parametric Auto Regressive (AR) model fit to the noise PSD, as described in [86]. One of the AR parameters is the standard deviation σ of the background noise, which is used in the wavelet de-noising procedure.

A signal x_i that is corrupted by additive Gaussian random noise $n_i \sim \mathcal{N}(0, \sigma^2)$ is given by,

$$x_i = h_i + n_i, \quad i = 0, 1, ...N-1, \tag{2.21}$$

where h_i is the transient signal. The signal x_i is used to find an approximation $\hat{h}_i$ to the original h_i, which minimizes the mean squared error,

$$\|\mathbf{h} - \hat{\mathbf{h}}\|^2 = \frac{1}{N} \sum_{i=0}^{N-1} |h_i - \hat{h}_i|^2. \tag{2.22}$$

If an orthogonal wavelet transform W is applied to the sequence of data x_i, we obtain,

$$W(x_i) = W(h_i) + W(n_i) \,. \tag{2.23}$$

For a given wavelet thresholding function T the threshold based de-noising can be written as,

$$\hat{h_i} = W^{-1}(T[W(x_i)]) \,. \tag{2.24}$$

The thresholding function is applied to the wavelet transform of the noisy signal, then the output is inverted and the wavelet transformed. The effectiveness of the technique is dependent upon the choice of wavelet used, the decomposition level,

and the amplitude of the threshold value.

For a given threshold T and wavelet coefficient w, the wavelet coefficient is retained if $|w| > T$, or is set to zero if $|w| < T$. This removes wavelet coefficients that are due to background noise, and retains wavelet coefficients that are due to the glitches. WDF-ML uses the universal Donoho and Johnstone threshold method [87], where,

$$T = \sqrt{2 \log N} \hat{\sigma} \,. \tag{2.25}$$

N is the number of data points, and $\hat{\sigma}$ is an estimate of the noise level σ, estimated during the AR parametric fit to the data.

The wavelet coefficients contain the energy of the glitch at different scales. After the wavelet thresholding procedure is applied, only the highest coefficients of the wavelet transform remain. These coefficients are expected to contain only features of the glitches. The energy of the glitch is given by the sum of the square of the coefficients above the threshold value. The SNR is then given by the energy divided by $\hat{\sigma}$.

WDF-ML outputs a list of triggers, which include the maximum SNR and frequency, a GPS starting time for the glitch, the duration, the name of the wavelet family which triggered the event, and the full list of the wavelet coefficients after the de-noising procedure. The peak frequency of the glitch is estimated as,

$$f_{max} = \frac{f_s}{2.0 \times \mathrm{w}} \times b \,, \tag{2.26}$$

where f_s is the sampling frequency, w is the window used in the WDF-ML process, and b is the scale of the wavelet transform corresponding to the coefficient with the maximum value. The event duration is estimated after applying a clustering step for events that are closer than 0.01 s.

For WDF-ML to correctly identify the glitch, the choice of window size and overlapping parameter between two consecutive sliding windows becomes important. A window size of 1024 points is used. As there is no re-sampling filter in the data pre-processing, the data is sampled at 16384 Hz, therefore, with 1024 points the time window is 0.0625 seconds. This ensures that the waveforms of duration 2 ms will be inside the window. An overlap value of 0.05 seconds is used in order to avoid problems caused by a glitch being in two consecutive windows.

WDF-ML applies the same machine learning classification algorithm, GMM, as described in section 2.3.1, but other clustering algorithms could be used, such as Affinity Propagation [88] or Kmeans [89]. Dimensional reduction is required to retain the most important features of the wavelet coefficients. This is achieved by first applying PCA, and then projecting the remainder of the coefficients on a two-dimensional space with Spectral Embedding [90, 91]. Spectral Embedding finds a low-dimensional representation of the data using a spectral decomposition of the graph Laplacian. The GMM machine learning algorithm is then applied to the reduced coefficients for classification.

2.3.3 Gravity Spy

Gravity Spy is a project that uses citizen scientists and machine learning to classify glitches [92]. Gravity Spy was launched in October 2016, before the start of the second aLIGO observing run (O2). Although this method is slower than the ones described previously, it is also more accurate, as every glitch is examined by multiple citizen scientists before they are classified. Glitches classified by the citizen scientists are used as training sets for a supervised machine learning classification on a larger set of glitches.

To find the glitches, Gravity Spy uses all Omicron triggers above an SNR threshold of 7.5. Only glitches that occur when the detectors are in observing mode are used, and any data that has been flagged as poor quality is discarded. The glitches are then made into spectrograms with four different time windows to accommodate short and longer duration glitches. Citizen scientists first train on a golden set of glitches previously classified by experts. The users are then split into three groups, which are beginner, intermediate, and advanced based on their performance. When enough confidence in a classification is reached, it is added to the training set. Gravity Spy uses a deep learning method that uses a Convolutional Neural Network (CNN) with multiple processing layers [92].

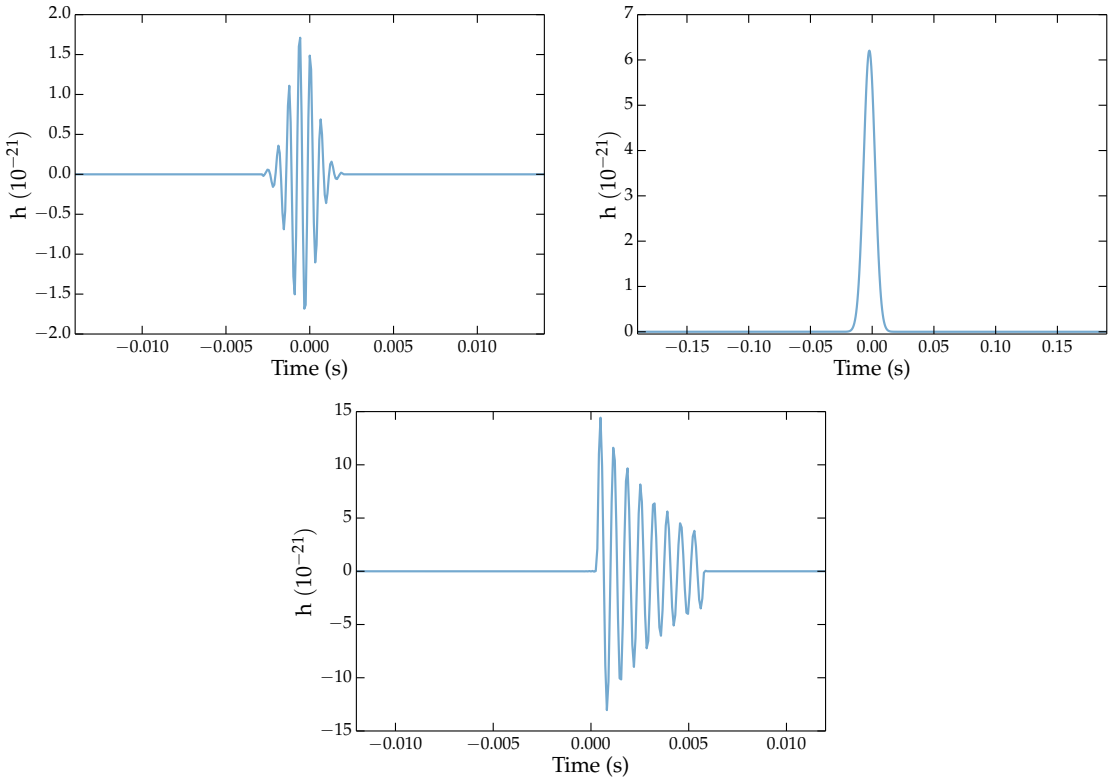

Figure 2.6: Examples of simulated glitches produced for data sets designed to test the performance of glitch classification algorithms. Top left is a typical sine Gaussian waveform. Top right is a typical Gaussian waveform. Bottom is a typical ringdown waveform. All of the simulated glitches have millisecond durations.

2.4 Mock Data Challenge

To test the performance of the classifying algorithms, three different simulated data sets were created. Gravity Spy is not included in this study, as it did not exist at the time the study was carried out. The data sets are designed specifically to test the efficiency of the algorithms in classifying glitches with different waveform morphology or frequency content.

For the sake of this investigation, we assume all advanced detectors to be affected by the same populations of glitches. Thus, we use early aLIGO sensitivity curves, for the Livingston detector only, to generate simulated Gaussian noise [71]. We do not use real data for this study because we need to know all of the properties of the glitches in the data set in order to accurately test the different methods. We generate three different data sets containing different types of simulated glitches, which are added to the Gaussian noise in five second intervals. The three data sets are designed to test if the different algorithms can classify glitches by frequency,

SNR and waveform morphology. Some example simulated glitches are shown in Figure 2.6. We consider three different waveform morphologies: sine Gaussian (SG), Gaussian (G) and ringdown (RD).

Sine Gaussian.

The Sine Gaussian waveforms are defined by,

$$h_{\times}(t) = h_0 \sin[2\pi f_0(t - t_0)]e^{-(t-t_0)^2/2\tau^2}\,, \tag{2.27}$$

$$h_{+}(t) = h_0 \cos[2\pi f_0(t - t_0)]e^{-(t-t_0)^2/2\tau^2}\,, \tag{2.28}$$

where $\tau = Q/\sqrt{2}\pi f_0$, f_0 is the central frequency, Q is the quality factor, t_0 is the GPS time at the centre of the sine Gaussian, and $h_0 = \text{hrss}/\sqrt{\tau}$, where hrss is the root sum squared amplitude of the transient. The τ parameter determines the width of the simulated waveform in the time-domain. A example of a real aLIGO glitch with a time series morphology similar to a sine Gaussian is shown in the next chapter, in Figure 3.8(d).

Gaussian.

The Gaussian simulated waveforms are defined by,

$$h_{\times}(t) = h_0 e^{-(t-t_0)^2/2\tau^2}\,, \tag{2.29}$$

$$h_{+}(t) = h_0 e^{-(t-t_0)^2/2\tau^2}\,. \tag{2.30}$$

The Gaussian waveforms are centred at zero frequency with the maximum frequency determined by the duration. An example of a real aLIGO glitch with a time series morphology similar to a Gaussian is the blip glitch, shown in Figure 3.8(a). Blip glitches are the most common type of glitch found in both of the aLIGO detectors.

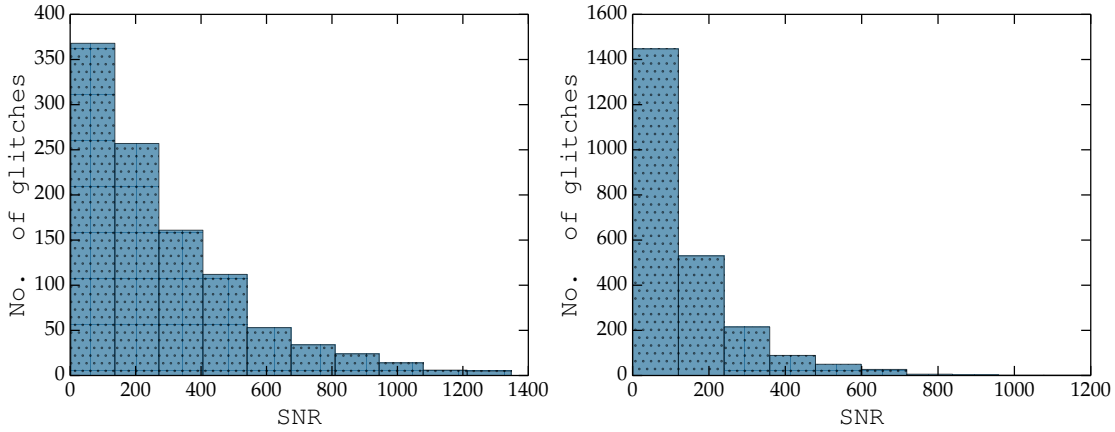

Figure 2.7: The distribution of SNR values of the simulated glitches added to simulated Gaussian early aLIGO noise. The left figure shows the SNR distribution for the glitches simulated in data set 1. The right figure shows the SNR distribution for the simulated glitches in data set 3. There are more glitches at lower SNR values with a few extremely high SNR glitches, as would be expected in real data. Figure reproduced from [7].

Ringdown.

The ringdown simulated waveforms are defined by,

$$h_{\times}(t) = h_0 \sin[2\pi f_0(t - t_0)]e^{-(t-t_0)/2\tau}\,, \tag{2.31}$$

$$h_{+}(t) = h_0 \cos[2\pi f_0(t - t_0)]e^{-(t-t_0)/2\tau}\,, \tag{2.32}$$

where $t > t_0$, and the other parameters have the same definition as the sine Gaussian. The time-domain waveforms of some high SNR glitches have a ringdown feature that appears after their initial spike.

2.4.1 Data Set 1

The first data set contains 1000 simulated Gaussian glitches, and 1000 simulated sine Gaussian glitches of different duration, frequency and SNR. The glitch waveforms were generated with Q, hrss, duration and frequency values distributed uniformly between the limiting values shown in Table 2.1. The SNR distribution for all glitches in this data set is shown in Figure 2.7.

	Waveform	Min Value	Max Value
Frequency (Hz)	SG	380	420
hrss ($Hz^{-1/2}$)	SG	1×10^{-21}	5×10^{-21}
Q	SG	5	10
SNR	SG	1	400
hrss ($Hz^{-1/2}$)	G	1×10^{-21}	5×10^{-21}
Duration (s)	G	0.001	0.01
SNR	G	1	400

Table 2.1: The limits on the parameters used when creating the simulated glitches in data set 1. The sine Gaussian and Gaussian glitches are well separated in frequency and duration. Table reproduced from [7].

2.4.2 Data Set 2

Data set 2 consists of 1000 simulated sine Gaussian glitches and 1000 ringdown glitches with SNR uniformly distributed between 1 and 400. All glitches were generated with identical frequency (400 Hz) and duration (2 ms). This data set is designed to test that the different algorithms can classify glitches by waveform morphology only.

2.4.3 Data Set 3

Data set 3 includes 1000 Gaussian, 1000 sine Gaussian, and 1000 ringdown glitches. The waveform parameters in this data set have a large range of values, which makes this data set more challenging to classify than the first two data sets. The parameters of the simulated noise glitches in this data set allow us to test the limitations of the three different classifying methods. The parameters for the simulated waveforms are distributed uniformly between the limiting values in Table 2.2, with an SNR distribution shown in Figure 2.7.

	Min Value	Max Value
Frequency (Hz)	40	1500
hrss ($Hz^{-1/2}$)	5×10^{-22}	4×10^{-21}
Q (SG, RD)	2	20
duration (G)	0.001	0.01

Table 2.2: The limits on the parameters used when creating the simulated glitches in data set 3. The glitches in this data set have a larger range of parameters than the glitches in the other data sets. Table reproduced from [7].

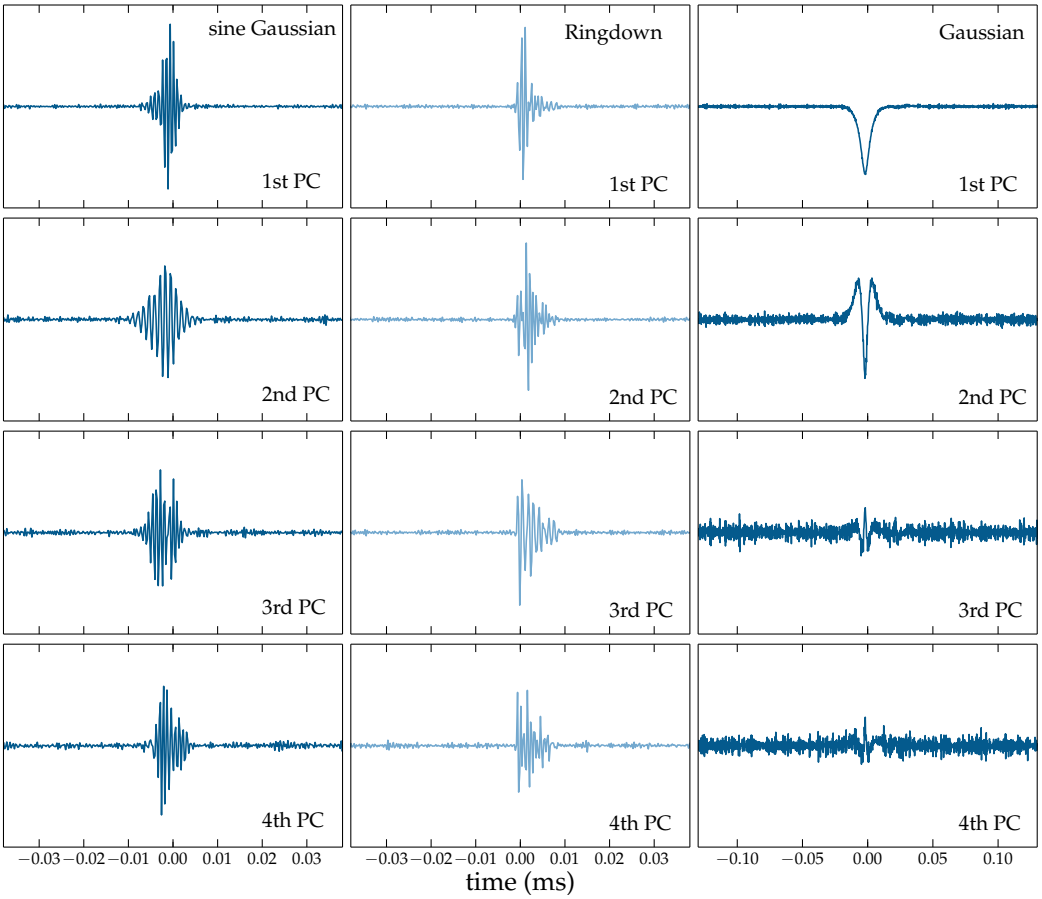

Figure 2.8: The first four PCs linearly combined in PC-LIB to make signal models for the different simulated glitches in data set 3. The left column are PCs made from fifty sine Gaussian simulated glitches. The PCs in the middle column are made from fifty ringdown glitches. The right column PCs are made from fifty Gaussian glitches.

2.5 Results

In this section, we show the PC-LIB results for the three data sets. The results are then compared to those obtained with the other classification algorithms WDF-ML and PCAT.

2.5.1 PC-LIB

For this study, we do not run Omicron to find the glitches, as the GPS times for the glitches are already known from the simulation process. This means that PC-LIB attempted to classify some glitches with an SNR too low for them to be detected. This does not happen when using Omicron triggers because an SNR threshold is

applied to Omicron triggers before they are analysed. The variance of the different glitch types is used to determine the ideal number of PCs. When analysing real GW data, PC-LIB can only classify glitches that belong to types that have been seen in the data many times previously. Therefore, to simulate how PC-LIB works on real detector data we assume that the first fifty glitches from each type in the data sets have been classified previously by machines or humans. The fifty waveforms are then used to make the PCs. An example of the PCs created from the different types of simulated glitches is shown in Figure 2.8. After the data has been whitened and high pass filtered there is still some noise around the waveforms that cannot be eliminated. This results in some higher order PCs that look only like noise that should not be included when reconstructing the waveform.

Data Set 1

For the first data set, 7 PCs were used to classify the glitches in to two different types. The variance curve is shown in Figure 2.9(a). The type 1 PCs represented 97% of the variance of the sine Gaussian glitches, and the type 2 PCs represented 70% of the variance of the Gaussian glitches. Although setting a threshold on the variance suggests that seven is an ideal number of PCs, after the 5th PC, the rest consisted of noise only, and did not contain any more information about the glitches.

In order to better interpret the results, it is important to understand how PC-LIB performs on Gaussian noise that contains no signals or glitches. In Figure 2.9(d), the distribution of Bayes factors using the signal model for the sine Gaussian glitches is shown for 100 instances of Gaussian noise only. The distribution shows that the expected value for noise only is $\log B_{S,N} \sim -5.5$. Due to the spread in $\log B_{S,N}$, we only classify glitches with $\log B_{S,N} > 5$ and consider any others as too low in SNR for them to be detected. To be conservative, a model for a type of glitch is considered to be correct if $\log B_{type1,type2} > 5$ for a type 1 glitch, or $\log B_{type1,type2} < -5$ for a type 2 glitch.

The log Bayes factors that were used to determine the glitch type for all of the detected glitches in this data set are shown in Figure 2.10. If the type 1 waveforms have been correctly classified then $\log B_{Type1-Type2}$ should be positive, and if the type 2 waveforms have been correctly classified then $\log B_{Type1-Type2}$ should be negative. When using the correct glitch waveform model, the increase in $\log B_{S,N}$ is

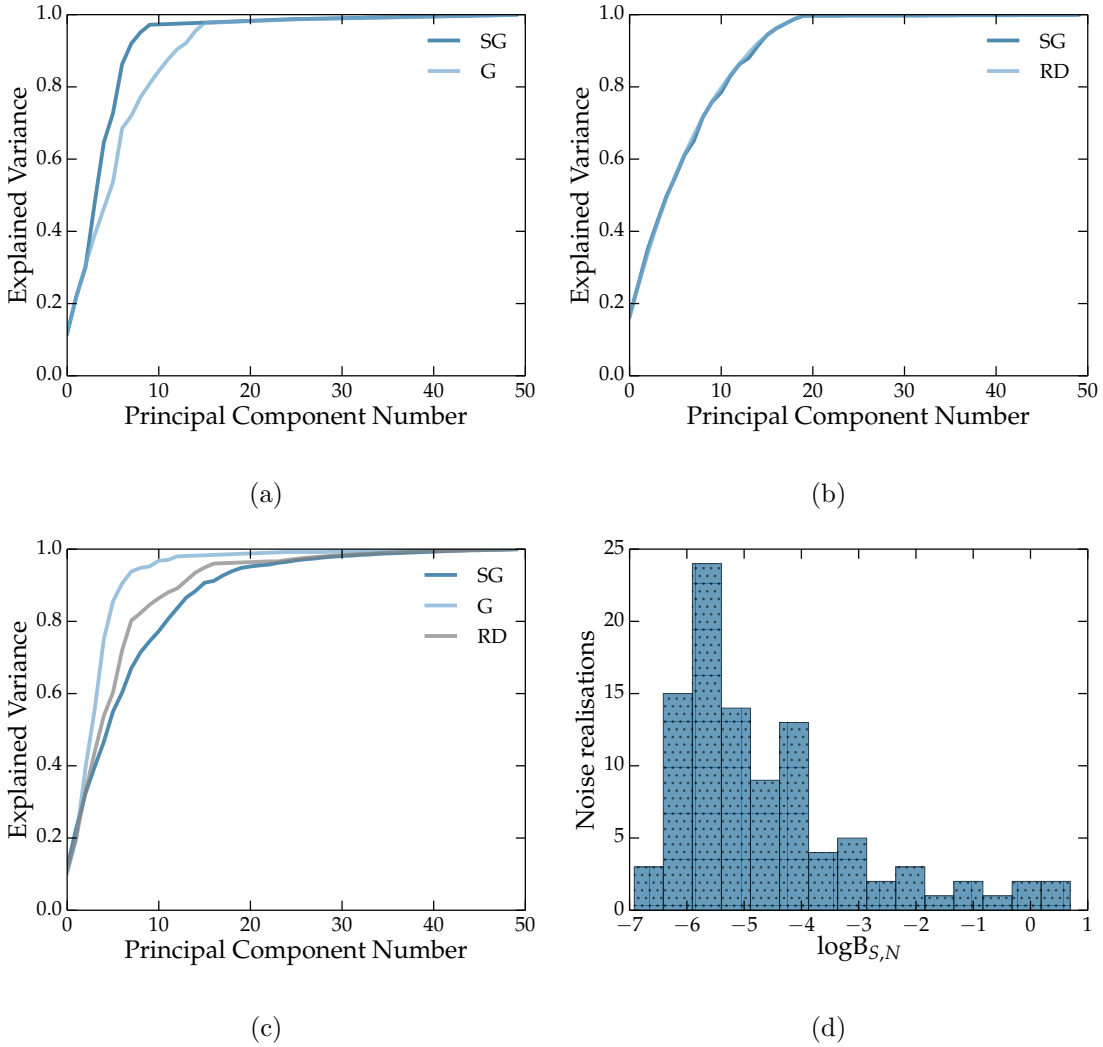

Figure 2.9: The PC-LIB variance curves for the simulated data sets, and the distribution of log Bayes factors. (a) The PC-LIB variance curves for data set 1. (b) The PC-LIB variance curves for data set 2. (c) The PC-LIB variance curves for data set 3. (d) The distribution of log Bayes factors obtained with the sine Gaussian signal model for Gaussian noise only. Similar values are obtained using other glitch models. If there is only noise with no glitches present then $\log B_{S,N} \sim -5.5$. To be conservative, we consider a glitch to be detected if $\log B_{S,N} > 5$.

proportional to the square of the SNR. When using the incorrect glitch waveform model $\log B_{S,N}$ remains low as the SNR values of the glitches increases.

In data set 1, 1452/2000 glitches have a large enough SNR for them to be detected by PC-LIB. The undetected glitches have SNR values smaller than 10. The results are shown in Table 2.3. PC-LIB classified all of the glitches with a very high efficiency ($\geq 95\%$). Type 1 is the main type for the sine Gaussian waveforms, and type 2 is the Gaussian waveforms. The 5% of Gaussian waveforms that were in the incorrect class had low SNR values (≤ 20).

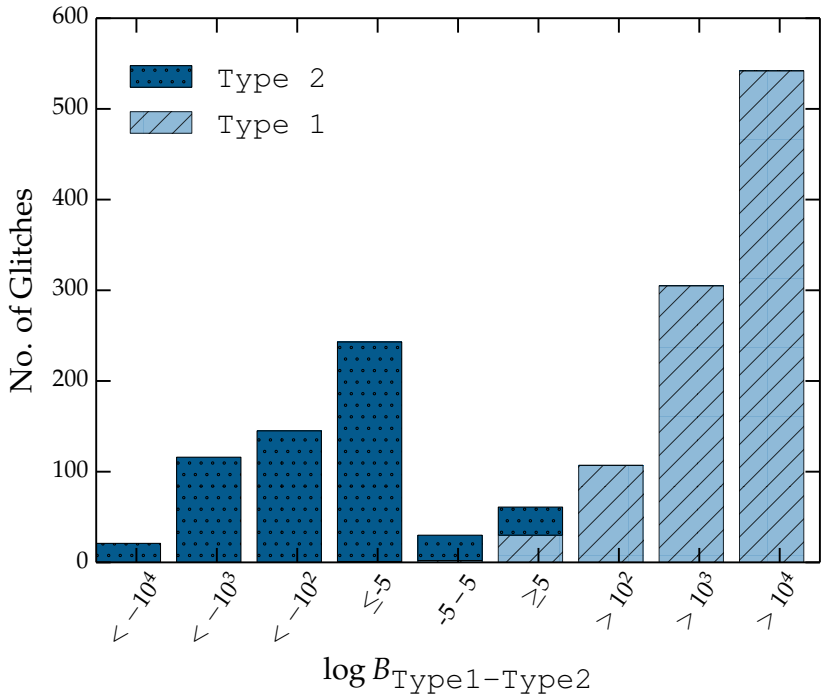

Figure 2.10: The distribution of the log Bayes factors used to determine the glitch type for all of the detected glitches in data set 1. Bayes factors are larger for glitches with a higher SNR. Type 1 corresponds to the sine Gaussian waveforms, and Type 2 corresponds to the Gaussian waveforms. If the sine Gaussian glitches were correctly classified then their log Bayes factor should be positive, and if the Gaussian glitches were correctly classified then they should have a negative log Bayes factor.

Data Set 2

For data set 2, 7 PCs are used to produce signal models which represent each glitch type. The variance curve is shown in Figure 2.9(b). The 7 PCs represented 80% of the variance of the type 1 (sine Gaussian) glitches, and 80% of the variance of the type 2 (ringdown) glitches. As we know that the glitches in each type are identical in this data set, only 1 PC should be necessary to represent all of the variance of the waveforms. The variance curve showed a larger number of PCs were needed to accurately represent the data set. This is because the variance curve is affected by the noise included in the glitch waveforms used to make the PCs. The PCs may give a better representation of the features of the glitches if only high SNR glitches are selected when creating the PCs. However, this may not always be possible if the glitches do not occur at high SNR values.

In data set 2, 1925/2000 of the simulated glitches were classified by PC-LIB, as shown in Table 2.4, and the others glitches have SNR values too small for them to be detected. 97.8% of the glitches with a sine Gaussian morphology were classified

	SG	G
PCAT Type 1	8.5	0
PCAT Type 2	0	15.4
PCAT Type 3	0	19.5
PCAT Type 4	0.9	0.2
PCAT Type 5	0	35.9
PCAT Type 6	0	29.0
PCAT Type 7	90.5	0
(maxcluster 2) PCAT Type 1	99	0
(maxcluster 2) PCAT Type 2	1	100
LIB Type 1	99.9	5
LIB Type 2	0.1	95
WDF Type 0	99.5	2.4
WDF Type 1	0.3	46.1
WDF Type 2	0.2	51.5

Table 2.3: The PC-LIB, PCAT and WDF-ML classification results for data set 1. The values show the percentage of the different morphologies classified in each type. The total number of simulated waveforms was 1000 of each type. The total number of glitches analysed were 1309 for PCAT, 1452 for PC-LIB and 1814 for WDF-ML. Table reproduced from [7].

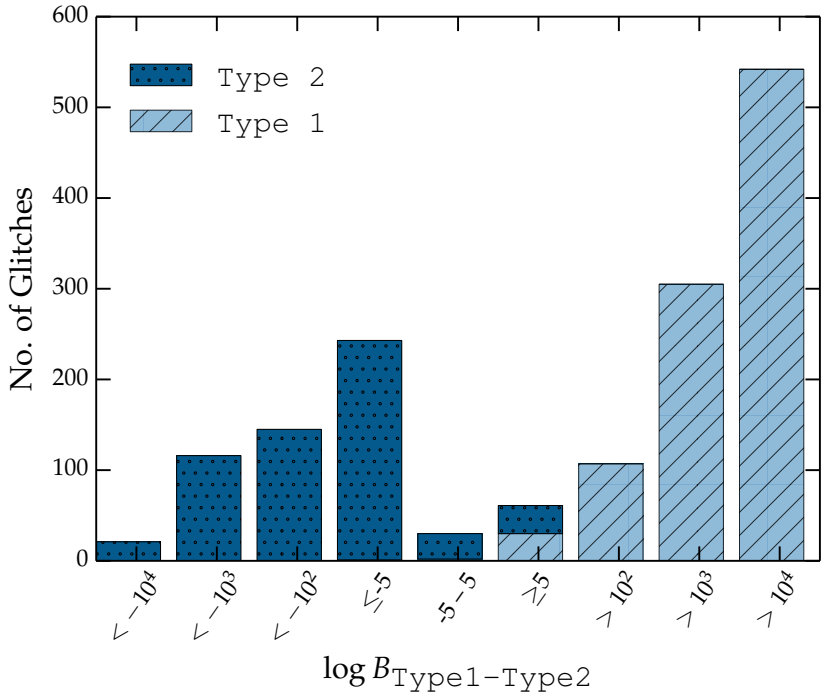

Figure 2.11: The distribution of log Bayes factors used to determine the glitch type for the 1925 glitches detected by PC-LIB in data set 2. If the type 1 (sine Gaussian) glitches were correctly classified then the log Bayes factor is positive, and if the type 2 (ringdown) glitches were correctly classified then their log Bayes factor should be negative. It is not possible to determine the type for glitches that have a Bayes factor between 5 and -5.

	SG	RD
(5 PCs) PCAT Type 1	0.32	12.6
(5 PCs) PCAT Type 2	25.5	0.2
(5 PCs) PCAT Type 3	20.4	1.3
(5 PCs) PCAT Type 4	1.3	2.8
(5 PCs) PCAT Type 5	0	37.4
(5 PCs) PCAT Type 6	0	30.0
(5 PCs) PCAT Type 7	52.4	0
(5 PCs) PCAT Type 8	0	16.1
(5 PCs, maxcluster 2) PCAT Type 1	1.1	97.4
(5 PCs, maxcluster 2) PCAT Type 2	98.9	2.5
LIB Type 1	97.8	4.8
LIB Type 2	2.2	95.2
WDF-ML Type 0	8.7	100
WDF-ML Type 1	48.0	0
WDF-ML Type 2	43.3	0

Table 2.4: The classification results obtained by PC-LIB, PCAT and WDF-ML for data set 2, which is designed to see if the methods can classify glitches by waveform morphology only. The values show the percentage of the different morphologies classified in each type. Two sets of PCAT results are included with different numbers of maximum clusters. The total number of glitches analysed were 1265 for PCAT, 1925 for PC-LIB and 1914 for WDF-ML. Table reproduced from [7].

as type 1, and 95.2% of the glitches with a ringdown morphology were classified as type 2. PC-LIB was clearly able to classify the glitches by waveform morphology alone with a high efficiency. The simulated glitches that were incorrectly classified by PC-LIB had SNR values below 20. The log Bayes factors for the two types of glitches are shown in Figure 2.11. The similar size and shape in distribution of Bayes factors is due to both of the glitch types having the same distribution of SNR values. If the type 1 (sine Gaussian) glitches were correctly classified then the log Bayes factor is positive, and if the type 2 (ringdown) glitches were correctly classified then their log Bayes factor should be negative.

Data Set 3

Using 7 PCs for the signal models, 2162/3000 of the glitches have a large enough SNR to be detected by PC-LIB. The variance curve is shown in Figure 2.9(c). The 7 PCs represent 67% of the variance of the sine Gaussian waveforms, 93% of the variance of the Gaussian waveforms, and 80% of the variance of the ringdown waveforms. The results are shown in Table 2.5. The table shows that type 2 contains

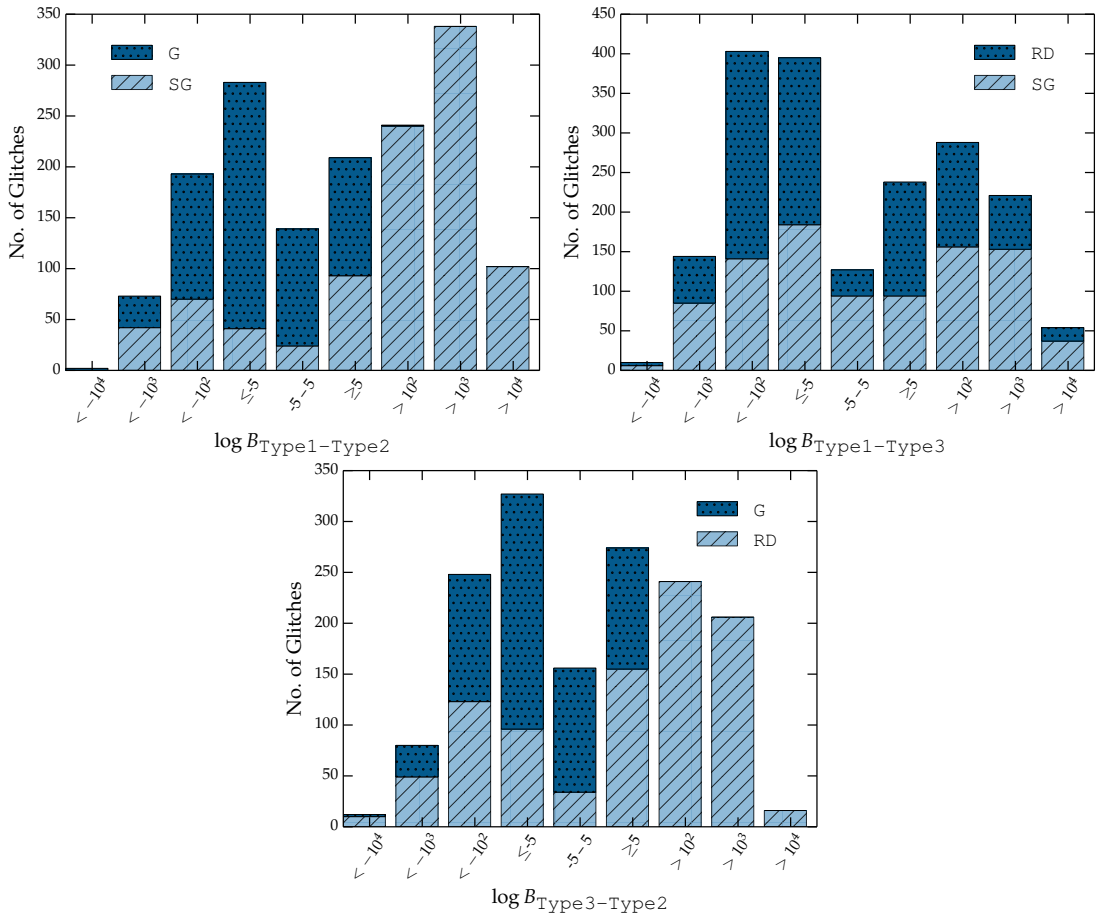

Figure 2.12: The distribution of log Bayes factors used to determine the glitch type for the detected glitches in data set 3. The top left compares the sine Gaussian and Gaussian glitches. The top right compares the sine Gaussian and ringdown glitches. The bottom compares the Gaussian and ringdown glitches. The Gaussian glitches can be distinguished from the others, but it is not possible to distinguish between the sine Gaussian and ringdown glitches.

the majority of the Gaussian glitches, 88.3%, and the other two types of glitches are mixed in types 1 and 3. Type 1 contains the mid frequency range ($300 - 700\,\mathrm{Hz}$) waveforms, and type 3 contains higher frequency waveforms ($700 - 1500\,\mathrm{Hz}$). A small number of low frequency sine Gaussian and ringdown glitches, $\sim 20\%$, were in the type 2 class with the Gaussian glitches. The 12% of Gaussian glitches that were incorrectly classified had low, $\lesssim 20$, SNR values.

The frequency distribution for the total number of simulated glitches in this data set is uniform. However, as only a small number of the total glitches were used to create the signal models, the frequency distributions for the glitches used to make the PCs was not a good representation of the glitch parameter space. The type 1 (sine Gaussian) glitches used to make the PCs contained more mid frequency range waveforms. The type 3 (ringdown) glitches used to make the PCs contained more

	SG	G	RD
PCAT (33PCs) Type 1	16.9	0	14.5
PCAT (33PCs) Type 2	4.8	100	9.6
PCAT (33PCs) Type 3	37.1	0	41.8
PCAT (33PCs) Type 4	10.7	0	4.5
PCAT (33PCs) Type 5	4.5	0	0.7
PCAT (33PCs) Type 6	21.2	0	19.7
PCAT (33PCs) Type 7	4.8	0	9.2
PCAT (20PCs) Type 1	15.5	0	13.6
PCAT (20PCs) Type 2	36.8	0	41.4
PCAT (20PCs) Type 3	14.2	0	13.0
PCAT (20PCs) Type 4	9.1	0	13.0
PCAT (20PCs) Type 5	0.8	0	0.3
PCAT (20PCs) Type 6	21.8	0	17.2
PCAT (20PCs) Type 7	1.8	100	1.5
LIB (5PCs) Type 1	39.5	4.9	23.8
LIB (5PCs) Type 2	17.3	88.3	23.2
LIB (5PCs) Type 3	43.3	6.8	53.0
WDF-ML Type 1	89.5	9.6	86.9
WDF-ML Type 2	5.9	49.7	7.0
WDF-ML Type 3	4.6	40.7	6.1

Table 2.5: The PCAT, PC-LIB and WDF-ML classification results for data set 3. The values show the percentage of the different morphologies classified in to each type. Two sets of PCAT results are included with different numbers of maximum PCs. The total number of glitches analysed were 1480 for PCAT, 2162 for PC-LIB and 2547 for WDF-ML. All methods were unable to distinguish between the sine Gaussian and ringdown waveform morphologies in this data set. Table reproduced from [7].

higher frequency waveforms. This shows that for real glitch types with a wider range of parameters, we need to be careful in the selection of waveforms that are used to make the signal model, so that a bias in the results will be not be introduced in certain areas of the parameter space.

PC-LIB was unable to distinguish between the sine Gaussian and ringdown glitches when the range of parameters for the waveforms was very large. This is because a low frequency sine Gaussian waveform has a closer waveform shape to a low frequency ringdown waveform than to a high frequency sine Gaussian waveform. Real glitches with characteristic waveforms have narrow frequency or duration distributions, see examples in Chapter 3, but this data set allows us to test the limitations of the different glitch classifying algorithms. The wide range of parameters of the simulated waveforms, especially duration, make it difficult to capture the variability of the glitches in the first few PCs.

Since PC-LIB needs to make signal models in advance for each glitch type, it is only possible for PC-LIB to classify known types of glitches in the data. A new signal model will need to be created any time that a new family of glitches appears in the data. On the other hand, PCAT and WDF-ML do not need any information about a glitch type before they start the classification procedure, they can begin to classify new glitch types as soon as they appear in the advanced detector data.

2.5.2 PCAT.

PCAT finds the glitches for all data sets using its own internal ETG. PCAT differs from PC-LIB as it applies PCA to all of the glitches found by the ETG in a segment of data.

Data Set 1

The PCAT ETG identifies 1309/2000 glitches above the SNR threshold. The first 5 PCs account for 75% of the variance in the data, as shown in Figure 2.14. The first 12 PCs describe all the major features of the glitches. Clustering with the first 5 PC coefficients leads to seven glitch types, as shown in Table 2.3. Types 2, 3, 5 and 6 contain Gaussian glitches. Types 1 and 7 contain sine Gaussian glitches.

The breakdown of Gaussian and sine Gaussians in to multiple types can be understood as a separation in frequency and SNR, for the Gaussian and the sine Gaussian waveforms, respectively. This is illustrated in Figure 2.13. Types 3 and 6 are the lower frequency Gaussian glitches, $\sim (40 - 90)\,\mathrm{Hz}$, and types 5 and 2 are the higher frequency Gaussian glitches, $\sim (100 - 150)\,\mathrm{Hz}$. Type 7 contains, on average, sine Gaussian glitches with SNRs larger by a factor of ~ 5, and a standard deviation larger by a factor of ~ 10, than type 1 glitches.

By forcing PCAT to cluster the data on a maximum of two types, 99% of sine Gaussian and 100% of Gaussian glitches are classified as type 1 and type 2, respectively. The few misclassified glitches in this case correspond to glitches with an identified GPS time not correctly aligned with the peak of glitch. This issue can be resolved by further tuning of the PCAT trigger generator.

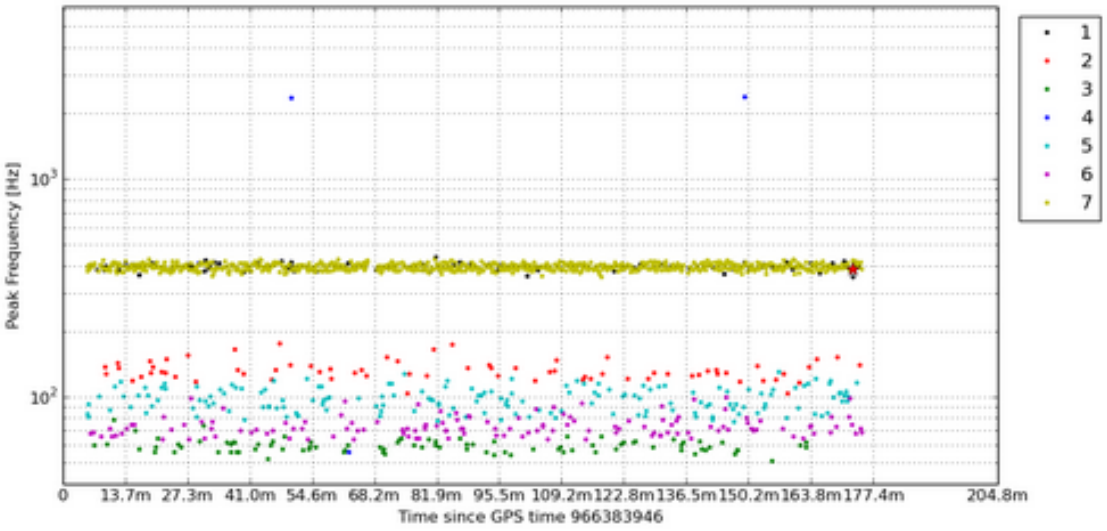

Figure 2.13: The GPS time, peak frequency, and classification of each glitch classified by PCAT in data set 1. The different colours show the 7 different PCAT glitch classes. Types 2, 3, 5 and 6 contain Gaussian glitches. Types 1 and 7 contain sine Gaussian glitches. The Gaussian glitches are clearly split into sub-types by frequency. Figure reproduced from [93]

Data Set 2

Here we describe the PCAT results for the second data set, which is designed to test if the classification methods can classify glitches by waveform morphology only. The classification results are shown in Table 2.4.

The PCAT ETG identifies 1265/2000 glitches above the PCAT SNR threshold. For this data set, the number of PCs used was changed to 5, which corresponds to the location of the "knee" of the variance curve (accounting for 51% of the variance), shown in Figure 2.14, as this method yields better classification efficiency. Glitches are first classified by waveform morphology and then broken down in to subclasses with different SNRs. The sine Gaussian glitches are in types 2, 3 and 7. The ringdown glitches are contained in types 1, 5, 6 and 8. Type 4 contains less than 30 glitches that are a mixture of the two types. The results show that PCAT is able to classify glitches, by waveform morphology alone, with a very high efficiency when noisy PCs are not included.

To demonstrate the effects of using too many noisy PCs, we run PCAT with 94 PCs, which account for 75% of the variance of the glitches in this data set. Clustering using the first 94 PC coefficients results in seven different glitch types, of which three types only contain one low SNR glitch. Morphology classification is

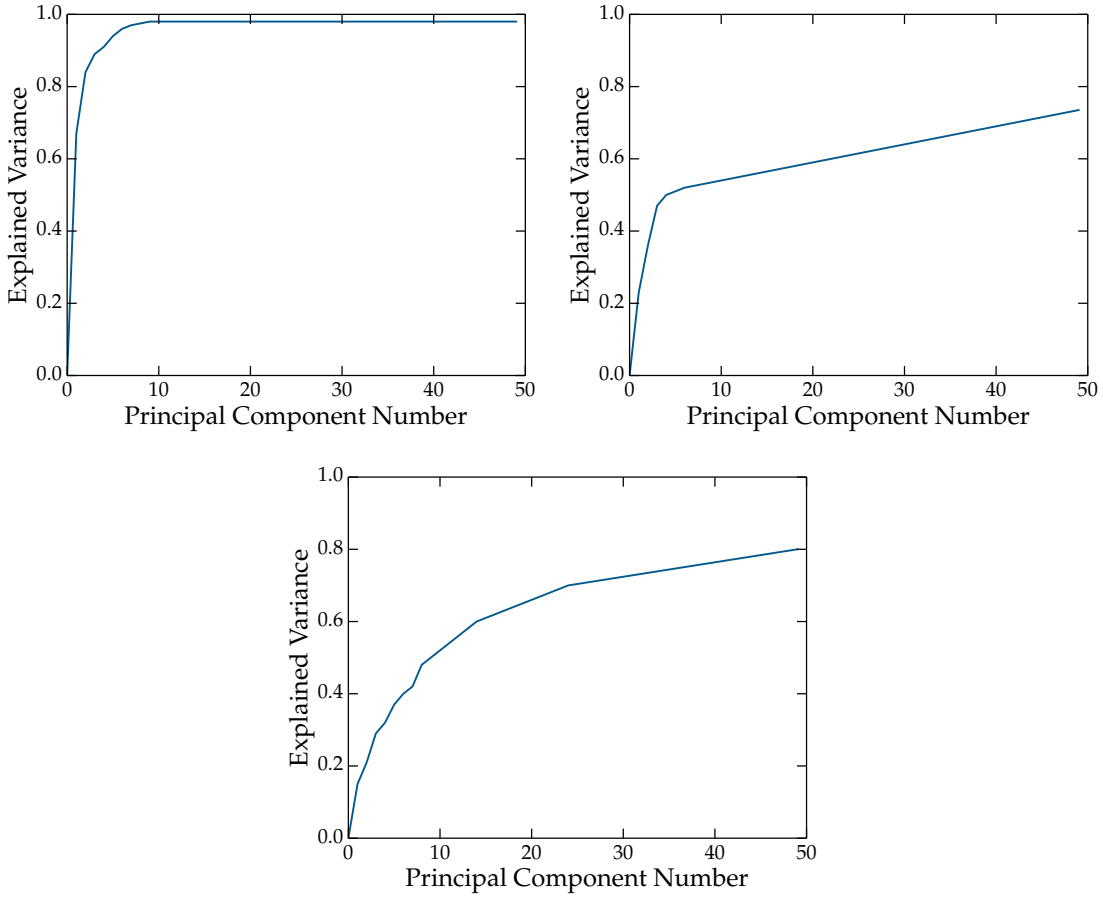

Figure 2.14: The amount of variance in the three different simulated data sets that is encompassed by each PCAT PC. Changes in the variance curve can determine the ideal number of PCs. Top left is the variance curve for data set 1. Top right is the variance curve for data set 2. The first 5 PCs are used for data sets 1 and 2, as this number correspond to the *knee* of the variance curve. Bottom is the variance curve for data set 3. Data set 3 has the largest variance, and the ideal number of PCs is less clear from the variance curve. The variance does not reach 1 due to the background noise included in the waveforms.

mixed: most types contain a roughly equal number of sine Gaussian and ringdown glitches. Glitches are classified according to SNR, as after the 10th PC, the rest only account for noise, and including too much noise degrades the efficiency of the classification algorithm.

The results can be improved further by limiting the maximum number of clusters to two, as shown in Table 2.4. Type 1 contains the ringdown glitches, and type 2 contains the sine Gaussian glitches. In this case, the few mis-classified glitches either have low SNR (∼10) or have waveforms with peaks that are not aligned with the GPS time for the glitch.

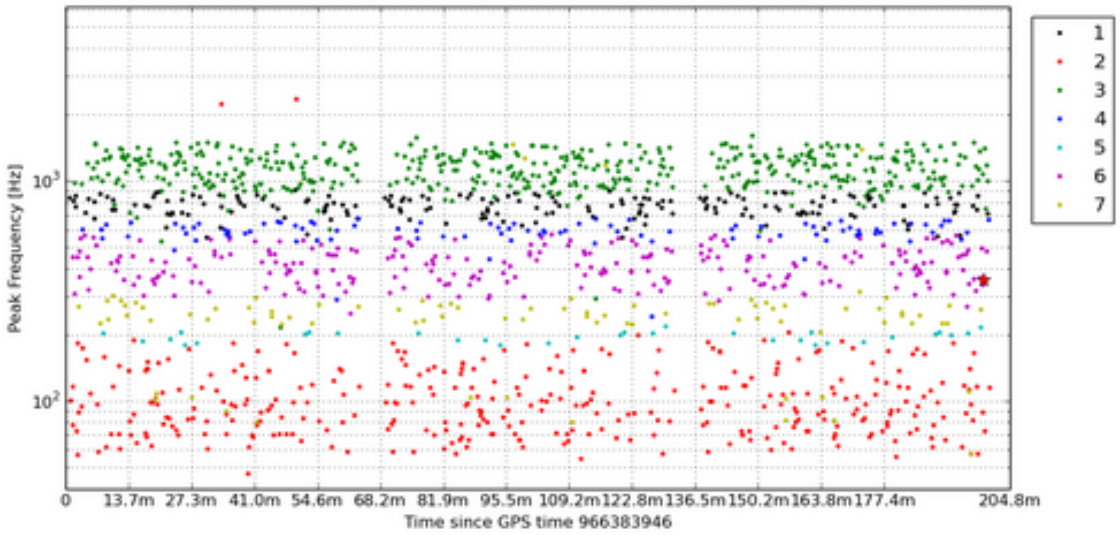

Figure 2.15: The GPS time, peak frequency, and classification of each glitch classified by PCAT in data set 3. The different colours show the classification results. The three different glitch types have been classified by frequency. Type 2 are the lowest frequency glitches. Type 3 are the highest frequency glitches. Figure reproduced from [94].

Data Set 3

The PCAT ETG identifies 1480/3000 of the glitches above the PCAT SNR threshold. They are classified into seven different types, as shown in Table 2.5. The first 33 PCs represent 75% of the variance of the data set, shown in Figure 2.14. The classification results are mixed, with type 2 being the exception, containing 100% of the simulated Gaussian glitches. From the distribution of peak frequencies for each PCAT type, shown in Figure 2.15, the mixed-classification can be understood as a frequency-based classification. Type 3 contains the highest frequency glitches. Type 7 and 5 contain the lower frequency glitches. There are a few ringdown and sine Gaussian glitches that are classified as type 2 (Gaussian), which have frequency distributions similar to the Gaussian glitches ($70 - 150\,\mathrm{Hz}$). The wide range of parameters of the simulated glitches makes it hard to capture the full range of the glitches parameters in the first few PCs, therefore, the main parameter captured by the PCs is frequency, on which the classification is then based.

Table 2.5 also shows the results using 20 PCs, which corresponds to the approximate location of the knee of the variance curve. Changing the method used to select the number of PCs that represent this data set did not lead to an improvement in the result.

2.5.3 WDF-ML

This sub-section describes the WDF-ML classification results. An SNR threshold of 15 was applied to all three data sets before classification.

Data Set 1

The WDF-ML ETG detected 1814/2000 glitches. The dimensions of the wavelet coefficients were reduced with 10 PCs that represented $\sim 95\%$ of the variance of the wavelet coefficients. The classification results are shown in Table 2.3. The efficiency for correct classification was higher than 97% for both glitch types. Figure 2.16 shows the coefficient parameter space for the classification results of the three types of glitches found in the data. The wavelet coefficients for different types of glitches are well separated in the parameter space. Type 0 contains the sine Gaussian glitches. The Gaussian glitches have been split in to two sub-types labelled type 1 and 2, where type 2 contains more lower SNR Gaussian glitches, between SNR 25 and 150, than type 1.

Data Set 2

In data set 2, WDF-ML detected 1914/2000 glitches. The results are shown in Table 2.4. Ten PCs were used to reduce the dimensions of the wavelet coefficients. They represented $\sim 98\%$ of the variance of the wavelet coefficients. WDF-ML was able to classify different glitches by waveform morphology alone, with a high, $\sim 96\%$, efficiency. The classification results are shown in Figure 2.16. There is a clear separation in the parameter space for the three different types. All of the detected ringdown glitches are in type 0. The sine Gaussian glitches have been split in to two classes, which are type 1 and 2. The two types of sine Gaussian glitches were not split by frequency or SNR in this case. The sine Gaussian and ringdown glitches can be incorrectly classified with a wrong choice of overlap value and window size, because if the glitch is split over two consecutive analysing windows then a sine Gaussian would be cut off in the middle of the waveform, which would make it appear to be a ringdown glitch. In real data, most glitches have a duration of a few milliseconds, therefore, a window of a few 100 milliseconds will be used.

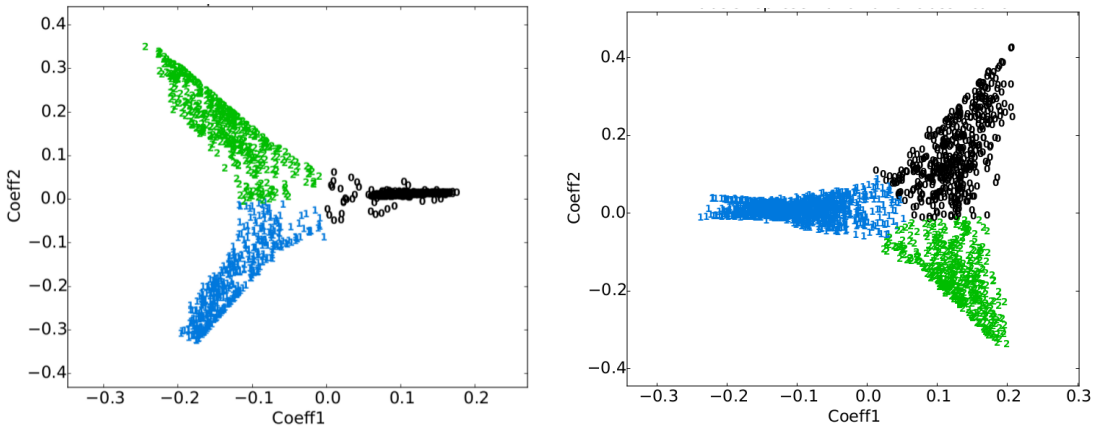

Figure 2.16: The reduced WDF-ML wavelet coefficients for the simulated glitches in data set 1 and 2. The colours represent the different glitch types. Left is the WDF-ML classification results for the transformed and reduced wavelet coefficients produced from the data set 1 glitches. Right is the transformed and reduced wavelet coefficients produced from the data set 2 glitches. The coefficients for the different types of glitches are well separated in the parameter space. Figure reproduced from [7].

Data Set 3

WDF-ML detected 2547/3000 of the glitches in data set 3. The sine Gaussian and ringdown glitches are mixed together in type 1. The Gaussian glitches have been split between types 2 and 3. The Gaussian glitches that were incorrectly classified into type 1 were those with an SNR lower than 20. Choosing more components for the Spectral Embedding stage will result in more sub-types for the sine Gaussian and ringdown glitches, but no clear distinction between the two types. In this data set, the glitches are spread in frequency and duration, therefore, results could be improved by using a multi-window analysis. This is a feature that can be added to future versions of the WDF-ML algorithm.

2.6 Summary and Discussion

This chapter introduces a new method for the fast classification of glitches in advanced GW detectors. Its purpose is to provide information that can lead to an improvement in data quality during an observing run. The method is tested and compared to other methods developed for glitch classification using data sets containing simulated glitches in Gaussian noise. The simulated data is designed to test how well the glitch classifiers can classify by frequency, SNR and waveform

morphology.

All three methods can classify glitches in GW detectors with a high level of efficiency. In the first data set, which contains glitches well separated in frequency and SNR, over 97% efficiency is obtained by all three methods. Reducing the threshold of the trigger generators, therefore including glitches with an SNR less than 20, can reduce the classification efficiency. In the second data set, we show that all three methods can classify glitches by waveform morphology alone. PC-LIB and PCAT require that the number of glitch types are specified in advance. If the number of glitch types requested by PCAT is higher than the actual number of glitch types in the data set, then the waveforms will be classified by waveform morphology first, and then split in to further sub-types by frequency and SNR. WDF-ML has also shown that if it identifies more types than those present in the data, then the waveform morphologies will be split into further sub-types by SNR or frequency. The third data set was more challenging to classify due to the large range of parameters of the simulated glitches.

The different algorithms identified different numbers of glitches in the data. To identify glitches, the PCAT ETG measures the excess power in the time series of a given channel. More sophisticated methods for transient identification have been devised, and they are in use in the LIGO and Virgo data analysis and detector characterization groups. However, the main goal of using the PCAT algorithm in this study is to provide a proof of concept for glitch classification rather than to provide a trigger generator for detector characterization analysis. Thus, a simple identification method based on excess power in time bins is sufficient for our scope. Future plans for the use of the PCA technique include improving the trigger generator or to interface the PCAT code with the Omicron ETG.

For PCAT and PC-LIB, the number of PCs that are used can have a large effect on the results of the classification. If too many PCs are used, then an incorrect classification is given due to some of the PCs consisting of only noise. As we cannot eliminate the background noise from the glitch waveforms that are used to make the PCs, we have found the best method of choosing the number of PCs to be the position of the "knee" of the variance curve. For WDF-ML, the selection of the analysing window size for the wavelet transform is fundamental for a correct classification. The window must be larger than the length of the glitches in the data, and to avoid a false classification of a glitch, the glitch must not be overlapping

between two windows. As PC-LIB runs on one second of data at a time, when analysing real glitches there may be multiple glitches of different types inside the one second of data, which could affect the efficiency of the classification.

In this study, only the GW channel of the detector is used. As all transients found by the ETGs will be classified into different types, it is possible that a real GW signal could be included in the glitch classification results. This could be avoided by removing signals that are coincident between two detectors before applying the classification methods. In future work, we plan to include multiple auxiliary channels in the classification procedure. If a glitch occurs in the GW channel in time coincidence with an auxiliary channel, it can help us to identify the cause of the glitch type [95, 96]. The number of possible auxiliary channels is very large, which makes machine learning an ideal tool for this type of classification due to the speed at which machine learning methods can process a large volume of detector data.

PCAT runs daily on data from the aLIGO detectors, providing a powerful diagnostic tool to the detector characterization team. WDF-ML has been used as a glitch event trigger generator, and monitoring tool, during past Virgo science runs. The machine learning classification procedure of WDF-ML is an innovative addition to this algorithm that will be used to classify glitches during the advanced detector science runs. The algorithms can be run on parallel computing clusters, and the code can be optimised, to allow the algorithms to run efficiently in real time.

Chapter 3

Advanced LIGO Data Quality

3.1 Introduction

During O1, GWs were detected from two binary black hole systems, GW150914 and GW151226, and another lower significance event LVT151012 [2, 19]. An extensive study of the glitches, observed around the time of the detections, was carried out as part of the validation process for the signals [66]. Detector characterisation can have a large effect on lower significance detections such as LVT151012. For example, the false alarm probability of LVT151012 was reduced from 14% to 2% after applying data quality vetoes [66]. In the previous chapter, we introduced a new method, called PC-LIB, designed for the fast classification of glitches in aLIGO and AdVirgo data. A comparison study was carried out with PCAT and WDF-ML, and it was shown that these methods can classify simulated glitches with an efficiency up to 97%.

In this chapter, we evaluate the performance of the algorithms using glitches in real data from aLIGO. This work provides an important test for understanding the performance of these methods on real, non-stationary data in preparation for future observing runs. In Section 3.2, we describe the data from aLIGO Engineering Run 7 (ER7) that was used to evaluate the performance of the algorithms on real aLIGO data. In Section 3.3, we give a brief overview of the three different algorithms and details of improvement since the study in Chapter 2. In Section 3.4, we present the results for the three algorithms on glitches from L1 and H1 ER7 detector data. In

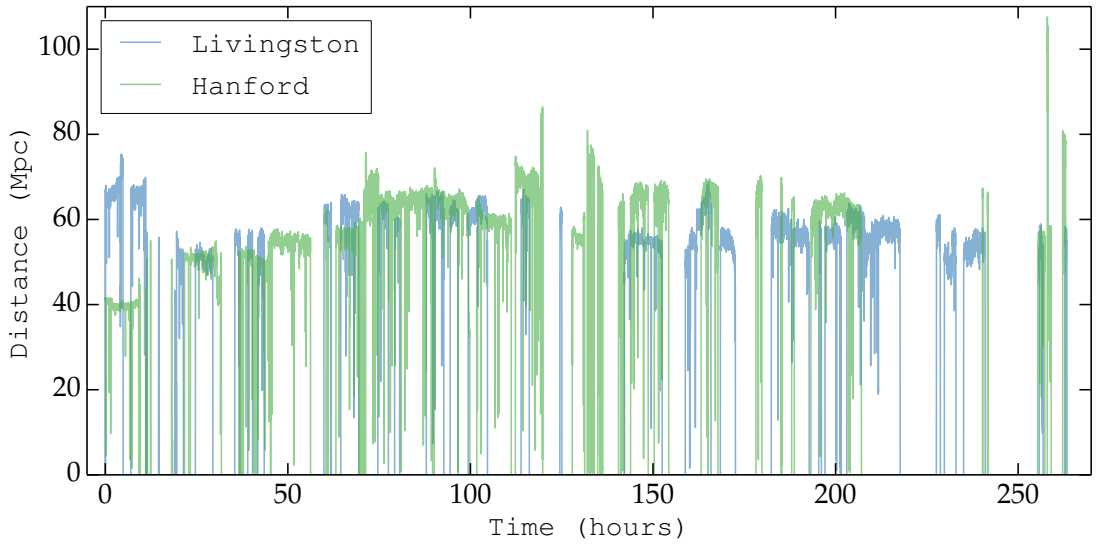

Figure 3.1: The mean angle averaged binary neutron star inspiral range for the two aLIGO detectors during ER7. The Hanford detector had a higher range but also a higher glitch rate. The average range was 50-60 Mpc. Figure reproduced from [8].

Section 3.5, we describe the results for the classification of glitches during O1, including the potential impact of the results on the searches and parameter estimation of GW signals. This is followed by a discussion in Section 3.6 of the plans for future improvements and classification during future aLIGO and AdVirgo observing runs.

3.2 Engineering Run Data

In this section, we use data from ER7, which began on the 3rd of June 2015 and finished on the 14th of June 2015. During an engineering run, the detectors are operated in the same way as during an observing run, and the data obtained is used to carry out multiple goals. The engineering run is used to test the performance of search pipelines running on data from multiple detectors, and to test a range of software and computing tools required for the detector operation, data acquisition and analysis. Detector characterization, calibration and commissioning improvements are also made during an engineering run. This results in data that is less stable than the data taken during an observation run, which is data taken with the intention of making detections. The average binary neutron star inspiral range, shown in Figure 3.1, for both H1 and L1 detectors in data analysis mode during ER7 was $50 - 60\,\mathrm{Mpc}$ [97].

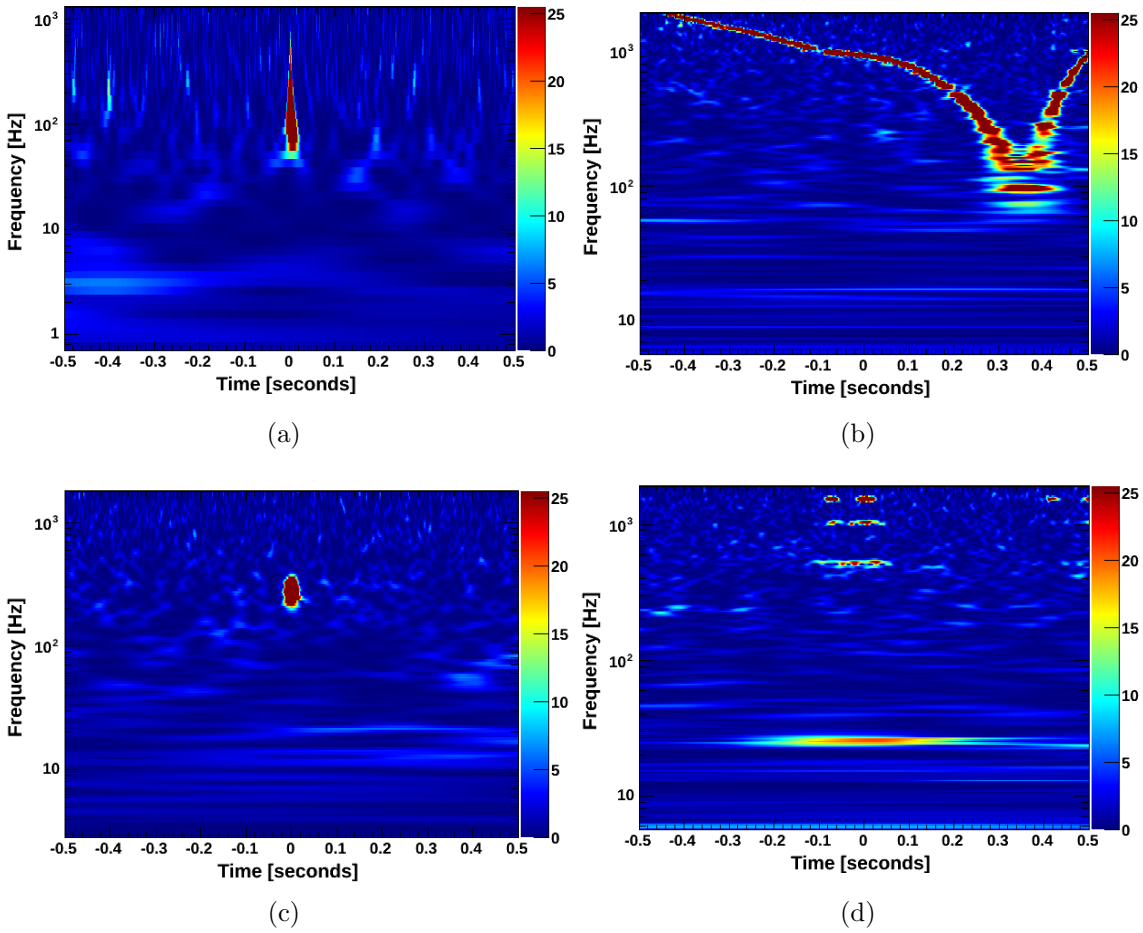

Figure 3.2: Spectrograms of typical glitch types found in Livingston ER7 data. They are generated using the Omega scan tool in LigoDV-Web [98], which matches the data to sine Gaussians. (a) A glitch characterized by a time-frequency tear drop shape in the spectrogram known as a *blip*. (b) A *whistle* glitch that often has a long duration and occurs at high frequencies. (c) A sine Gaussian hardware injection used to determine which channels are sensitive to gravitational waves. (d) An $n^*505\,Hz$ glitch characterized by high frequency lines that occur at multiples of 505 Hz. Figure reproduced from [8].

Livingston.

In the period analysed, data from L1 consists of 48 segments where the interferometer was locked and in data analysis ready mode. The data segments vary in length from 1 second to $\sim$ 7 hours. Any segments of data that are less than a minute in duration are discarded, as a longer segment of data is required to measure the PSD. The total discarded amount was 49 seconds of data. The total length of L1 data analysed is $\sim$ 87 hours.

Glitches of different types are often recognised by their shape in a spectrogram.

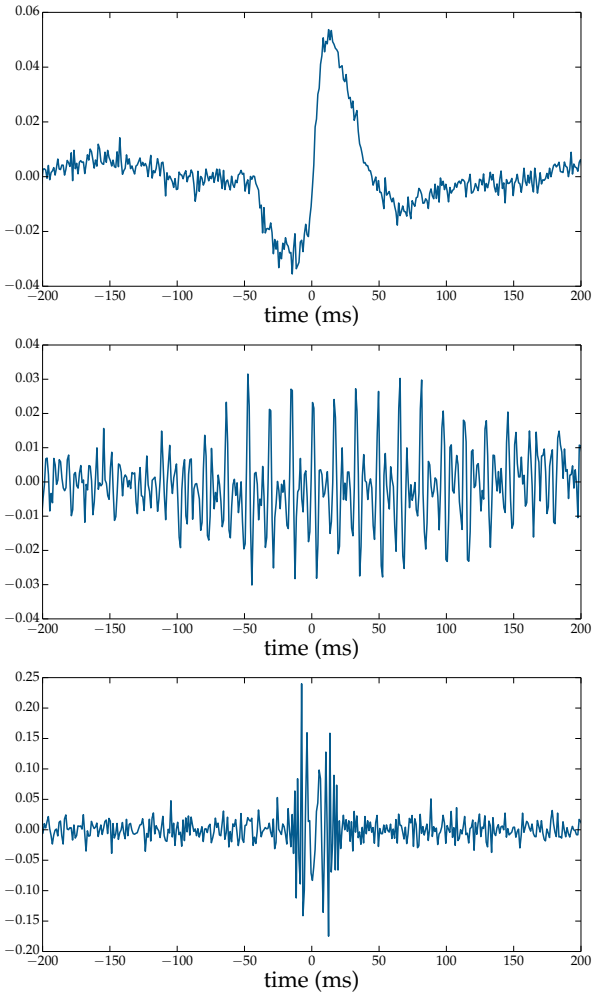

Figure 3.3: The typical high pass filtered and whitened time series waveforms for three of the most common glitch types found in the Livingston detector during ER7. (Top) A spike which appears as a tear drop in a spectrogram and is known as a blip glitch. (Middle) The time series waveform of the n^*500 Hz glitch. (Bottom) The time series of a whistle glitch. Figure reproduced from [8].

The most common glitch types in the L1 ER7 data are shown in Figure 3.2. Figure 3.2(a) shows glitches characterized by a tear drop shape, known as *blips*. Blip glitches create long tails in the CBC and burst search backgrounds, and they are particularly difficult to veto as they do not occur in any auxiliary channels that are not sensitive to GWs [66]. Figure 3.2(b) shows longer duration transients, known as *whistles*, which are caused by radio frequency beats [99]. Figure 3.2(d) shows a glitch known as an $n^*505\,Hz$ glitch as it appears at multiples of 505 Hz. The time series of the common L1 glitches is shown in Figure 3.3. Some other glitches in the data that are not shown include those below 10 Hz. Glitches span the entire frequency range considered in this study. Some glitches may have occurred due to the increased ground motion created by tropical storm "Bill" in the Gulf of Mexico [97].

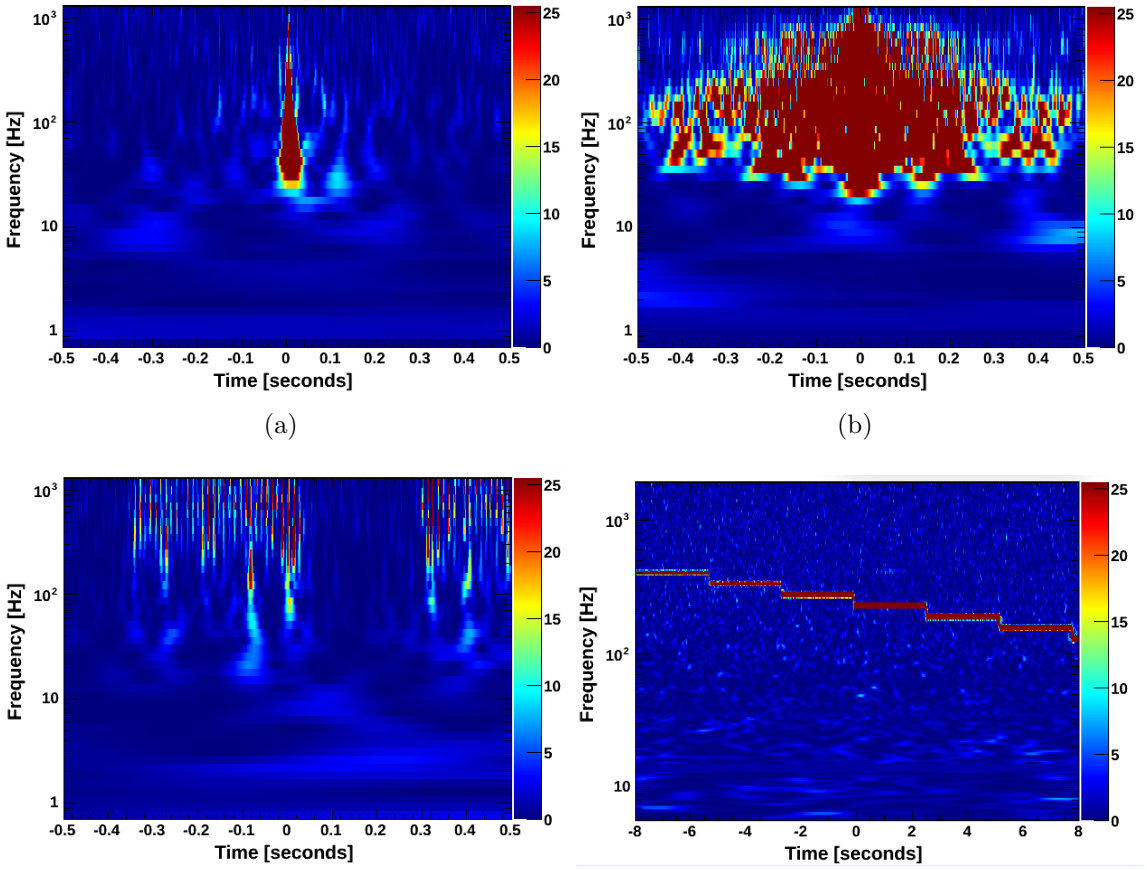

Figure 3.4: Examples of some of the most common glitch types found in Hanford ER7 data (a) A tear drop glitch known as a *blip*. (b) An *extremely loud* glitch that has a large SNR and duration. This glitch type created significant drops in the detectors range. (c) A high frequency glitch type called a *repeating* glitch. (d) A longer duration line occurring at the beginning of a number of data segments. Figure reproduced from [8].

A number of hardware injections were also made during ER7. An example is shown in Figure 3.2(c). Hardware injections are artificial signals simulated by inducing a motion of the detector optics. Hardware injections can be used for two different purposes. The first are injections made for the detector characterisation team, often sine Gaussians, which are used to test which auxiliary channels are sensitive to GWs [64, 65]. The second are hardware injections of astrophysical signals for the testing of search algorithms.

Hanford.

In the period analysed, data from the H1 detector consists of 50 segments where the interferometer was locked and in data analysis ready mode. The data segments vary in length from 1 second to almost 14 hours. As with L1, any segments of data that are less than a minute in duration are discarded. The discarded data was a total of 116 seconds. The total length of Hanford data analysed is $\sim$ 141 hours.

The H1 data is highly non-stationary and contains many more glitches than the aLIGO L1 data. In particular, the H1 data contains many high SNR glitches that caused a significant drop in the binary neutron star inspiral range. An example *extremely loud* glitch is shown in Figure 3.4(b). It was suspected that these large glitches were caused by cleaning of the beam tube [97]. As with the L1 data, H1 data also contains blip glitches and a number of hardware injections. In Figure 3.4(c) is another Hanford glitch type, which we refer to as a *repeating* glitch. The time series of the most common H1 glitch types is shown in Figure 3.4.

3.3 Classification Algorithm Updates

To classify glitches in ER7 data, we use the same three glitch classification methods described in Chapter 2. To find the ER7 glitches, PC-LIB uses Omicron, the main ETG used by the LIGO Scientific Collaboration (LSC) detector characterization group [76, 77]. WDF-ML and PCAT use their own internal ETGs.

In Chapter 2, PC-LIB created signal models using fifty glitch waveforms for each glitch type. In this chapter, we only use ten waveforms to make signal models for each of the ER7 glitch types. This configuration is better suited for a quick classification of new glitch types as we plan to implement in future observing runs.

PCAT runs in a similar way to the previous chapter. The data are down-sampled to 8192 Hz, whitened and high-pass filtered at 10 Hz, with a 0.125 s window around each GPS time, as glitches are typically of ms duration. This can lead to a loss of sensitivity to longer duration glitches. However, this effect can often be safely neglected as longer duration glitches do not occur very often during observing runs, when the data is generally more stable than during engineering runs.

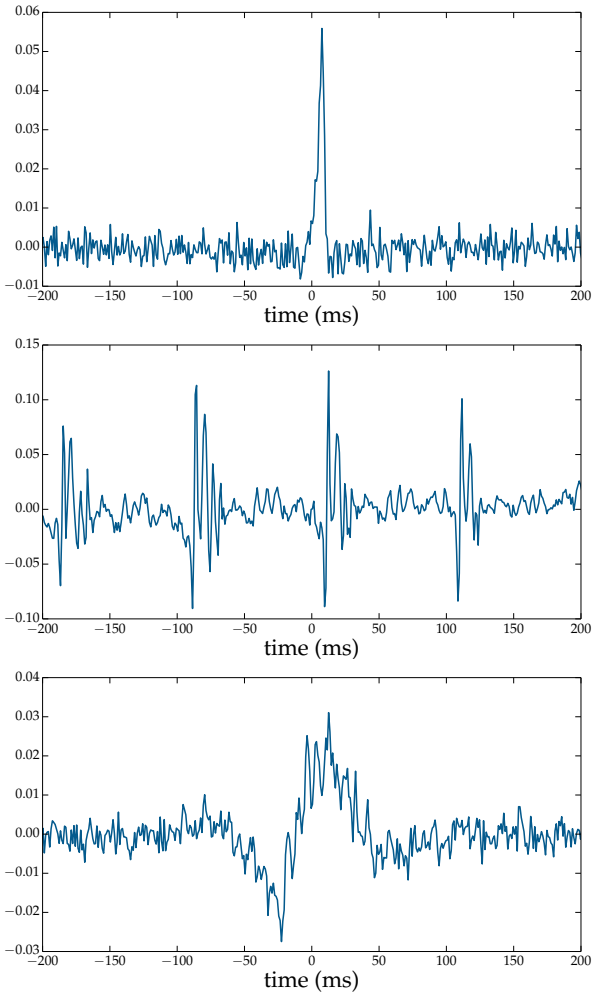

Figure 3.5: The typical whitened and high pass filtered time series waveforms for three of the most common glitches found in the Hanford detector during ER7. (Top) The typical time series waveform of a blip glitch. (Middle) The time series of the repeating glitch. (Bottom) The time series waveform of a short duration sine Gaussian hardware injection. Figure reproduced from [8].

WDF-ML down-samples to 8192 Hz before the whitening process is applied. The down-sampling is a new feature of WDF-ML that was not implemented in the version of the algorithm used in Chapter 2. The data are then whitened using parameters estimated at the beginning of each locked segment. After whitening, the wavelet-transform is applied, using the bank of wavelets described in Chapter 2. A window of 2048 points was used, with an overlap of 1968 points, which corresponds to a duration of 0.25 seconds.

3.4 ER7 Classification Results

In the following sections, we show the classification results obtained by PC-LIB, PCAT and WDF-ML for glitches in ER7 H1 and L1 data. All algorithms are run with the same configurations that we expect to use during observing runs to better understand their future performance. To determine if the glitches are classified correctly, spectrograms of all glitches are made and visually inspected to determine the glitch type. In the future, this kind of testing or training set can be provided by the citizen science project Gravity Spy (described in Section 2.3.3).

3.4.1 Livingston

To find glitches in L1 data we look for triggers that are coincident within half a second in the outputs of all ETGs. The WDF-ML ETG was run with an SNR threshold of 10 at a sampling rate of 8192 Hz. Omicron was run with a lower SNR threshold of 5. We then look for glitches that are coincident between both WDF-ML and Omicron, above SNR 20, and find a total of 426 coincident glitches. The Omicron SNR, duration and frequency of all 426 transients are shown in Figure 3.8(d). The constant lines are due to Omicron's method for measuring frequency [76]. As the PCAT ETG cannot find the lower frequency (below 10 Hz) triggers, and some longer duration triggers, we still classify glitches that are coincident between Omicron and WDF-ML, but missed by PCAT, as those triggers would still be classified when running in low latency.

PC-LIB

To create the signal models, the first 5 PCs for each glitch type are used as determined by the knee of the variance curve, as shown in Figure 3.6. As different signal models that correspond to real glitches are now implemented, and real aLIGO noise is now being used, the distribution of log Bayes factors are recalculated using the blip glitch signal model when there are no signals or glitches in the data. The results are shown in Figure 3.6. The expected value for noise only is ~ -4. A glitch is only considered as detected if the signal verses noise log Bayes factor is larger than 5.

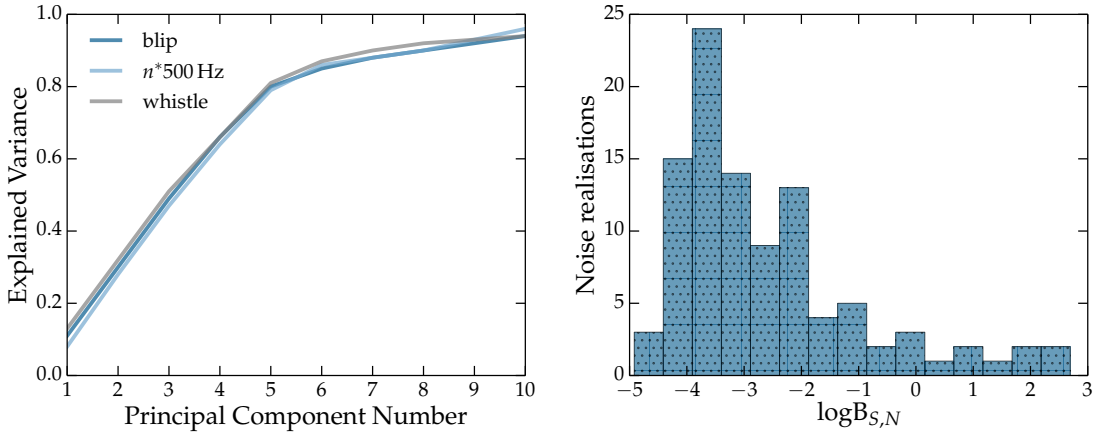

Figure 3.6: (left) The amount of variance explained by each PC for the three different types of glitches considered by PC-LIB in ER7 L1 data. The ideal number of PCs was 5, as this corresponds to the knee in the variance curve. (right) The distribution of Bayes factors for the PC-LIB blip glitch signal model run on 1000 instances of ER7 background noise.

PC-LIB classifies all glitches into four different types. Class 0 contains 33 glitches that are not detected by PC-LIB, and are thus classified into a noise class. Most of the noise class glitches occur at frequencies lower than the 10 Hz cut-off used by PC-LIB. Class 1 contains 249 glitches. Almost all of the glitches are blips except for two of the glitches in this type that are mis-classified. All of the hardware injections in the data are also found in Class 1. Class 2 contains 131 glitches that are the n^*505 Hz glitches. There are no incorrectly classified glitches in Class 2. Finally, class 3 contains 13 glitches. Most of the glitches in this class are the whistle glitches. Three of the glitches in this class are mis-classified and should be in Class 2. Overall PC-LIB classifies 98% of the detected glitches correctly.

PCAT

PCAT applied a threshold on the SNR of the glitches of 4.5 and the maximum possible number of glitch types was set to 10. The ideal number of PCs was estimated by finding the knee of the data set variance curve, as shown in Figure 3.7, which gave a total number of 20 PCs.

All the glitches were classified into 10 different classes. 90 triggers that were coincident between the Omicron and WDF-ML ETGs were missed by the PCAT ETG. Included in these missed triggers are all of the whistles, as their duration is longer than the PCAT analysis window, and 17 triggers where nothing was visible

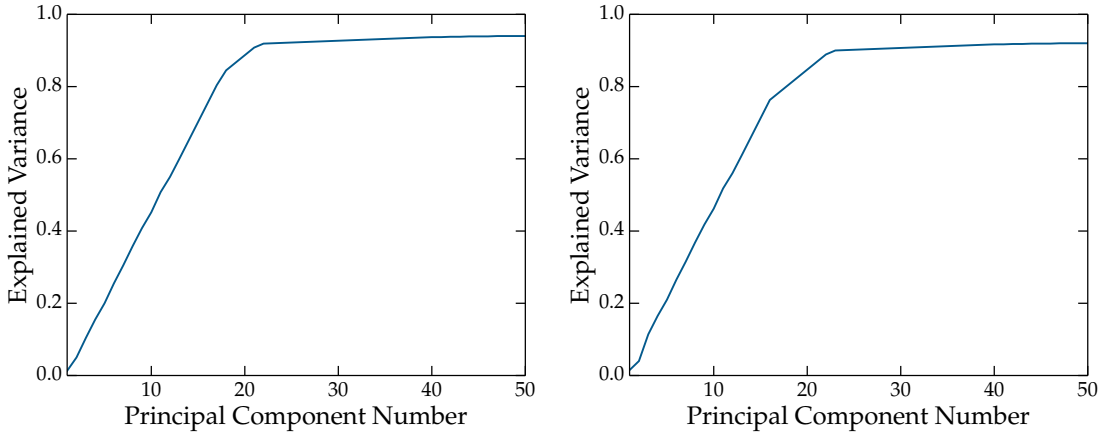

Figure 3.7: The PCAT variance curves for the glitches in Advanced LIGO ER7 data. Left is the variance curve for L1. Right is the variance curve for the H1 data. For each detector, 20 PCs were used as this corresponds to the knee in the variance curves.

in a spectrogram. 20 of the lower SNR hardware injections are also missed. As PCAT does not detect any of the whistles, the remaining glitches are classified into two main types, which are the blips and the $n^*505\,\mathrm{Hz}$ glitches, further split into different sub-types.

PCAT classes 1, 4 and 10 contain the blip glitches. Class 4 contains only 2 glitches, class 1 contains 123 glitches and class 10 contains 100 glitches. Classes 1 and 10 contain 11 and 20 hardware injections, respectively. The three sub classes are characterized by different duration of the glitches. Triggers in class 1 have the lowest ($\leq 0.005\,\mathrm{s}$) duration, class 10 have a larger ($\leq 0.01\,\mathrm{s}$) duration, and class 4 contains two longer ($\geq 0.01\,\mathrm{s}$) duration spikes. Two of the glitches in class 10 were incorrectly classified.

Classes 3, 5, 6, 7 and 8 contain the $n^*505\,\mathrm{Hz}$ glitches. Triggers in classes 5, 7 and 8 all have SNR values between 20 and 25 and durations of $\sim$ 0.01 s. Class 3 contains triggers of the same glitch type, but with larger durations (≤ 0.02 s), and SNR values up to 50. Class 6 contains only one glitch, also of the same type, but with an SNR value of 57 and a duration value of 0.005 s.

PCAT classes 2 and 9 contain 11 and 7 glitches, respectively. As these glitches are not visible in a spectrogram, it is not possible to determine what their type is and if they are classified correctly. Overall 95% of the glitches are correctly classified by PCAT.

WDF-ML

WDF-ML classifies all glitches into five different classes. The 5 classes consist of two main types of glitches, as WDF-ML cannot accurately classify the longer duration whistles, due to the short analysis time window. Sub-classes are determined by the wavelet family of the glitches, rather than split by duration or SNR as for PCAT.

WDF-ML classes 0 and 3 contain the blip glitches. Class 0 contains 195 glitches, and class 3 contains 86 glitches. The two sub-classes contain 29 hardware injections. They also contain 8 of the whistle glitches, as WDF-ML cannot accurately classify longer duration glitches. Four of the class 0, and one of the class 3 glitches, are incorrectly classified.

The second main glitch type found by WDF-ML corresponds to the $n^*505\,\mathrm{Hz}$ glitches. The glitches were split into three sub-classes, namely class 1 that contains 46 glitches, class 2 that contains 70 glitches, and class 4 that contains 29 glitches. Class 1 contains three incorrectly classified glitches, and class 3 contains two of the whistles glitches. Class 4 contains 4 hardware injections that are mis-classified. Overall WDF-ML classifies 95% of the L1 glitches correctly.

Comparison.

Figure 3.8 shows a comparison of the classifications made by all three methods. All methods are able to classify glitches with a high level of accuracy in real non-stationary ER7 data. WDF-ML performs better at classifying very low frequency glitches, as it does not need to use a lower frequency cut-off. Figure 3.8(a) shows that PC-LIB Class 1, the blip glitches, is split into two sub-types by PCAT, and PC-LIB Class 2 is split into four PCAT sub-types. Figure 3.8(c) shows that PC-LIB Class 1 is split into two WDF-ML sub-types, and PC-LIB Class 2 is split into three WDF-ML sub-types. Figure 3.8(b) shows that the method that WDF-ML and PCAT use to split glitch types into different sub-classes is different, as the blip glitches contained in PCAT classes 1 and 10 are split between WDF-ML blip glitch classes 0 and 3.

Only PC-LIB is able to separate the whistle glitches into a separate class, due

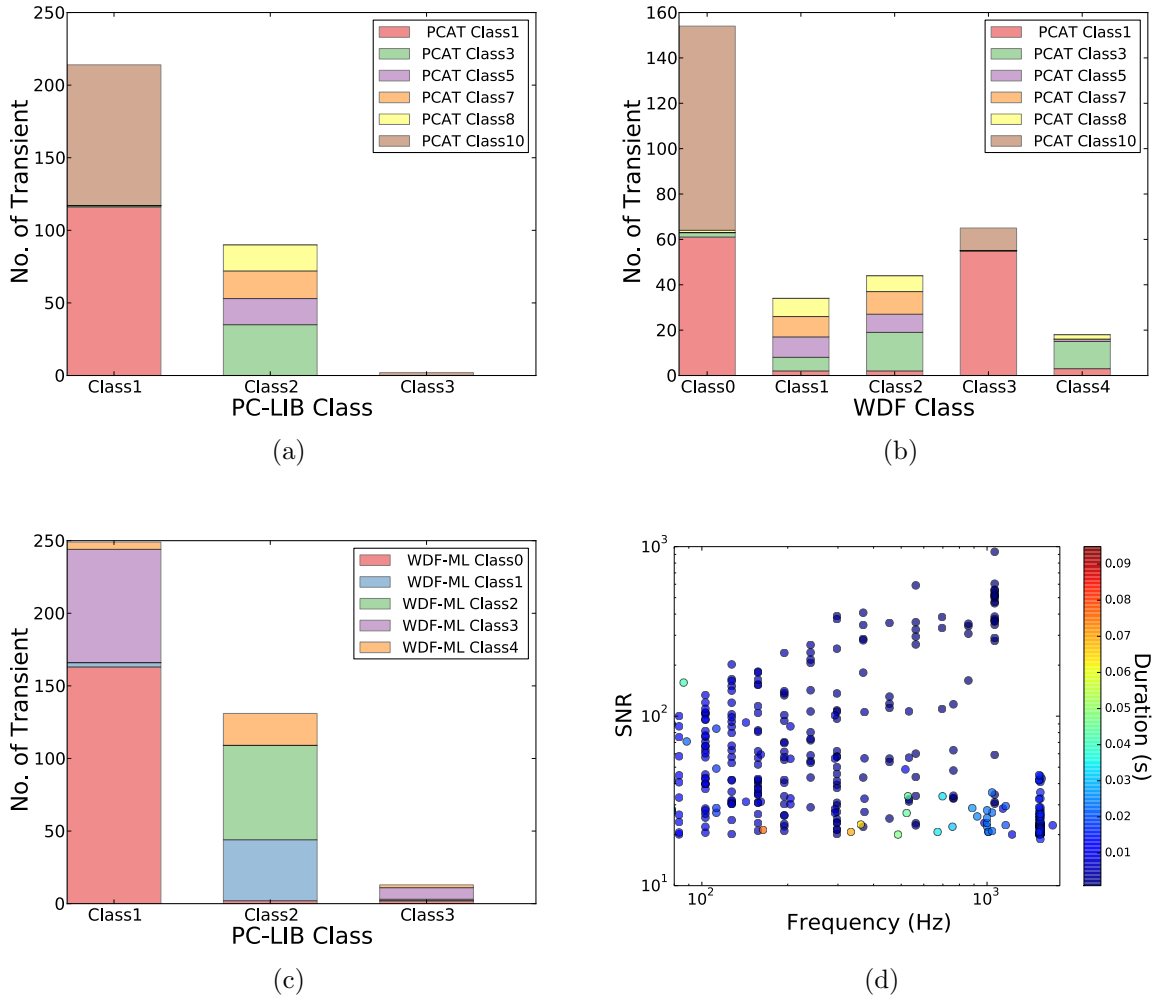

Figure 3.8: Classification comparisons for the three different classification algorithms using the data from LIGO Livingston during ER7. (a) Compares the classification results of PCAT and PC-LIB. PCAT class 2,4,6 and 9 are not shown as they contain less than 15 glitches. (b) Compares the classification results of PCAT and WDF-ML. (c) Compares the classification results of PC-LIB and WDF-ML. (d) The SNR and frequency of all the glitches classified in the data. Figure reproduced from [8].

to the longer 1 s time window used by this method. The efficiency in classifying these glitches for the other algorithms could be improved by using a longer time window. However, this could lead to multiple shorter duration glitches occurring in the same time window. As PC-LIB looks for specific known glitch types, it could be used to add labels to the classifications of the other methods. This could make it easier to find out which glitch classes correspond to known glitch types, and which classes are new types that have not occurred previously. As WDF-ML and PCAT can classify new glitch types as soon as they appear in the data, they can be used to provide waveforms for the PC-LIB signal models.

3.4.2 Hanford

As for the L1 data, glitches coincident within 0.5 s between all ETGs are classified. A higher SNR threshold of 30 is used for H1, as the data contains many more glitches than the L1 data, and is more non-stationary. A larger number of glitches are not classified, as it would take too much time to inspect spectrograms of all of the glitches to determine if the classification results are correct. A total of 1865 coincident glitches are classified in H1. The Omicron SNR, duration and frequency of the glitches are shown in Figure 3.9(d). The data contains more longer duration glitches than L1.

PC-LIB

As with the L1 data, 5 PCs are used to create signal models for the H1 glitches, as this number corresponds to the knee of the variance curve. PC-LIB splits the glitches into two different classes. A noise class contains the 6 glitches shown in Figure 3.4(d), as they cannot be detected by PC-LIB, because they do not belong to any of the known glitch types that were searched for by PC-LIB. Class 1 contains 1651 glitches that correspond to the blip glitches, and 13 hardware injections. It contains 23 glitches that are mis-classified and should be in class 2.

Class 2 contains 207 glitches, which are the repeating glitches. This class also includes 4 hardware injections that are more similar to a sine-Gaussian in shape than those classified into class 1. This class includes 61 glitches that are mis-classified and should be in class 1. Overall, PC-LIB classifies 95% of the detected H1 glitches correctly.

PCAT

With 20 PCs that correspond to the knee of the variance curve, shown in Figure 3.7, PCAT classified the H1 glitches into 7 different types. The PCAT ETG did not detect 120 of the glitches coincident between the WDF-ML and Omicron ETGs. They are glitches below 10 Hz, or triggers from the long duration lines, shown in Figure 3.4(d), which are not really glitches. The detected glitches are split into 7

different classes.

The data contains two main types of glitches. The first type is the blip glitches, which PCAT splits into 6 different sub-classes with 267, 603, 648 44, 1, and 64 glitches respectively. Class 1 contains 9 mis-classified glitches. Classes 2, 3 and 5 all have one mis-classified glitch. Classes 2, 3 and 6 contain lower duration (~ 0.005 s) glitches, with different frequency ranges. Classes 1, 5 and 16 contain relatively longer duration waveforms (~ 0.01 s), which also have different frequency ranges.

The second type of glitch is the repeating glitches. This glitch type is found in PCAT class 4, which contains 117 glitches that are all classified correctly. Overall, PCAT classifies 99% of the detected H1 glitches correctly.

WDF-ML

WDF-ML splits the H1 glitches into three different classes. Class 1, which is the main type for the blip glitches, contains 1358 glitches. This class contains all the hardware injections, and the very low frequency glitches that can not be detected by PCAT and PC-LIB. There are 10 glitches in this class that are mis-classified. WDF-ML class 2 contains 145 glitches that are characterized by spikes in the time series, but have longer durations and lower SNR values than the glitches in WDF-ML class 1.

WDF-ML class 0 contains 326 glitches corresponding to the repeating glitches. This class also contains 122 mis-classified glitches. As before, this is because all of the mis-classified glitches in this class have a duration (~ 1 s), which is much longer than the time window used in the WDF-ML analysis. Overall, WDF-ML classifies $\sim 92\%$ of the H1 glitches correctly.

Comparison.

The results obtained by all three methods for the H1 glitches are compared in Figure 3.9. As WDF-ML uses a small time window of 0.25 s, the efficiency of the classification is reduced when the data are highly non-stationary and contain many

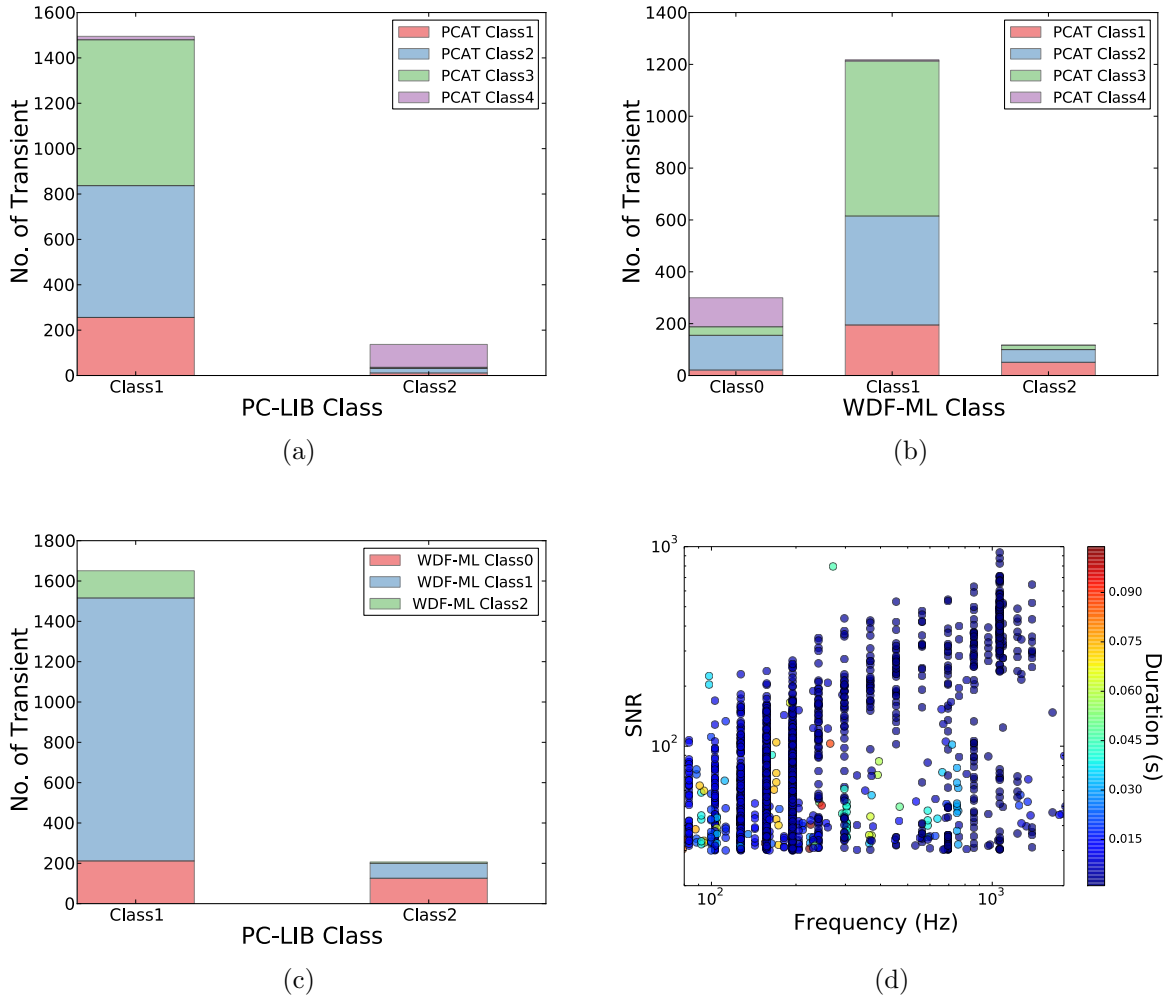

Figure 3.9: Classification comparisons for the three different classification methods for aLIGO Hanford ER7 data. (a) PC-LIB splits the glitches into two classes. PCAT can split different types into sub-classes. (b) PCAT and WDF-ML comparison. WDF-ML has difficulty with glitches which have a larger duration than their analysis window. (c) Comparison of PC-LIB and WDF-ML classifications. (d) The Omicron SNR, duration and frequency of all the glitches classified in ER7 H1. The discreteness in frequency is a feature of the Omicron algorithm. Figure reproduced from [8].

long ($\sim$ 1 s) duration glitches. Even with 137 mis-classified glitches, the overall accuracy of the WDF-ML H1 results is $\sim$ 92%. WDF-ML estimates the PSD at the beginning of each locked segment. This may introduce errors towards the end of the segment if the data is highly non-stationary. Machine learning methods perform better when the data set analysed is large. Therefore, the larger number of glitches in H1 may have improved the classification efficiency. Because of the different strengths and weaknesses of the different methods, having multiple classifiers is a winning strategy.

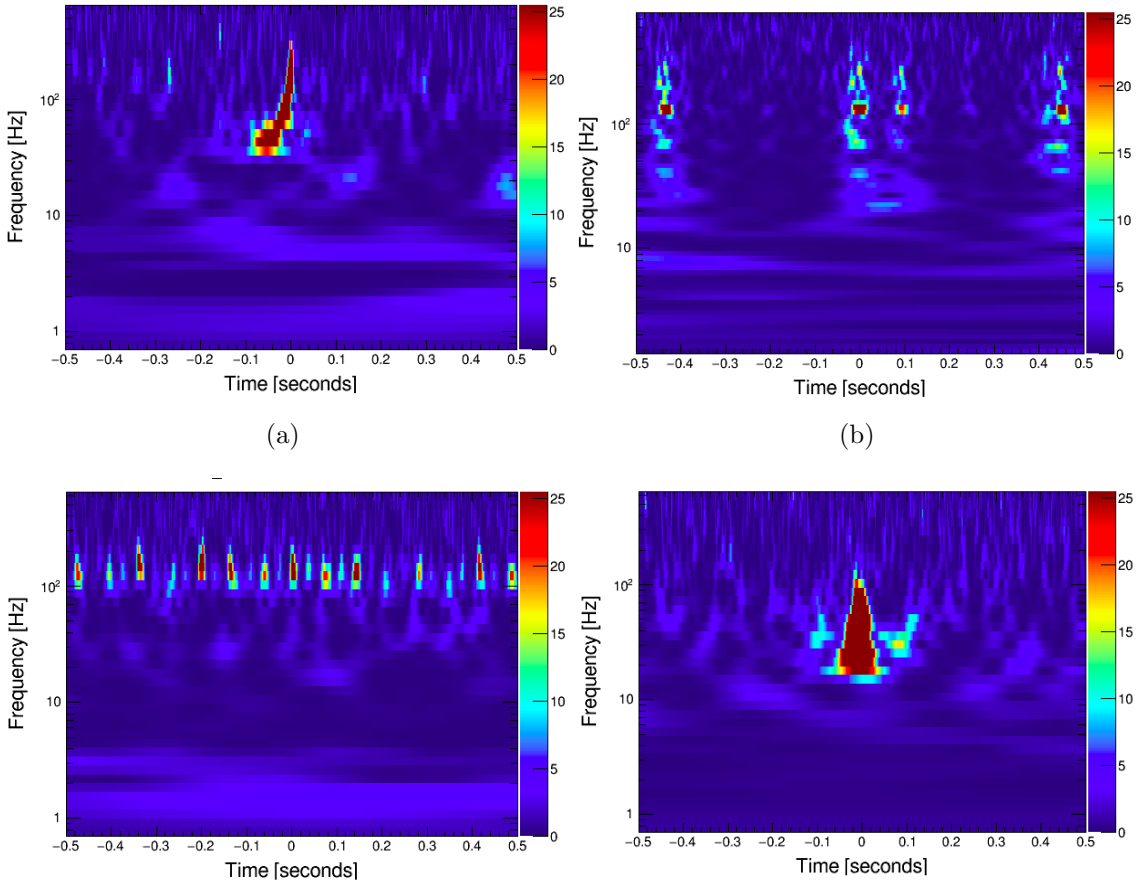

Figure 3.10: The time-frequency morphology of some common glitch types found in aLIGO Livingston data during the first observing run.(a) A CBC hardware injection that has a characteristic chirp shape. (b) A glitch type known as *helix*. (c) This glitch type is named *blue mountain*. (d) A sub-type of blip glitches known as *tomte*.

3.5 O1 Glitches

In this section, we show the PC-LIB results for glitch classification during O1. In the 51.5 days of O1 data, approximately 10^6 significant glitches over a minimum SNR threshold of 6 were identified by Omicron. As this number is too large for PC-LIB to classify all of the glitches in a reasonable time frame, we classify all O1 glitches with an SNR larger than 12 and with a frequency larger than 30 Hz, and less than 2000 Hz. This leads to a total of 2346 glitches in L1, and 7304 glitches in H1 that were classified by PC-LIB during O1.

There were 9 main types of glitches searched for by PC-LIB during O1. This is larger than the number of glitches found in the ER7 data because a lower Omicron

SNR threshold was used for the O1 glitches. The largest glitch type is the blips, shown in Figure 3.4(a), and some sub-types of blips named after their shape in a spectrogram. They are the *tomte* glitch, shown in Figure 3.10(d), and *koi fish*, shown in Figure 3.11(b). The data also contains CBC hardware injections with the characteristic chirp shape, shown in Figure 3.10(a). The other glitch types are *helix*, shown in Figure 3.10(b), extremely loud glitches that saturate a spectrogram, glitches created by light scattering in the detector, shown in Figure 3.11(a), glitches known as *blue mountain* glitches, shown in Figure 3.10(c), and whistle glitches as seen previously in the ER7 data. A few glitch types are found in only one detector. An example is the high frequency glitches, shown in Figure 3.11(d), and glitches that occur repeatedly on short time scales, shown in Figure 3.11(c), which are only found in H1. There are other types of glitches in O1 that are below the SNR threshold or the low frequency cut-off, which are classified by Gravity Spy as it uses a lower SNR threshold of 7.

As for the ER7 data, one second of data around the GPS times provided by Omicron is used. The data are down-sampled to 4096 Hz, and a lower frequency cut-off of 10 Hz is applied. To make signal models for the O1 glitches, 10 waveforms for 9 different glitch types are used to make the PCs. The first four PCs, for the blip and whistle glitches, are shown in Figure 3.12. Only a small number of PCs are needed to represent each glitch type, as there is only a small variance in their waveforms. To produce signal models for the O1 glitch types, 5 PCs as used as determined by the knee of the variance curves.

The number of glitches classified into each type, in each detector, is shown in Table 3.1. The blip glitch is the most common type of glitch found in both of the detectors, with 1598 in L1, and 3831 in H1. PC-LIB is unable to distinguish between the different sub-types of blips. This is because the time series for different blip types is almost identical, even though they have differences in their spectrograms. It is unknown if the blip sub-types have the same origin or are multiple different types of glitches. Many of the triggers identified by Omicron were classified as not being a glitch, as PC-LIB could not find anything in the data, as the Bayes factors were consistent with noise. There are 286 glitches of this type in L1, and 726 glitches of this type in H1. Some of the Omicron triggers in this class were at the edge of very high SNR glitches where the triggers were not clustered well by Omicron, or were glitches that did not fit into any of the known classes searched for by PC-LIB. Therefore, they did not match the any of the signal models well enough for them

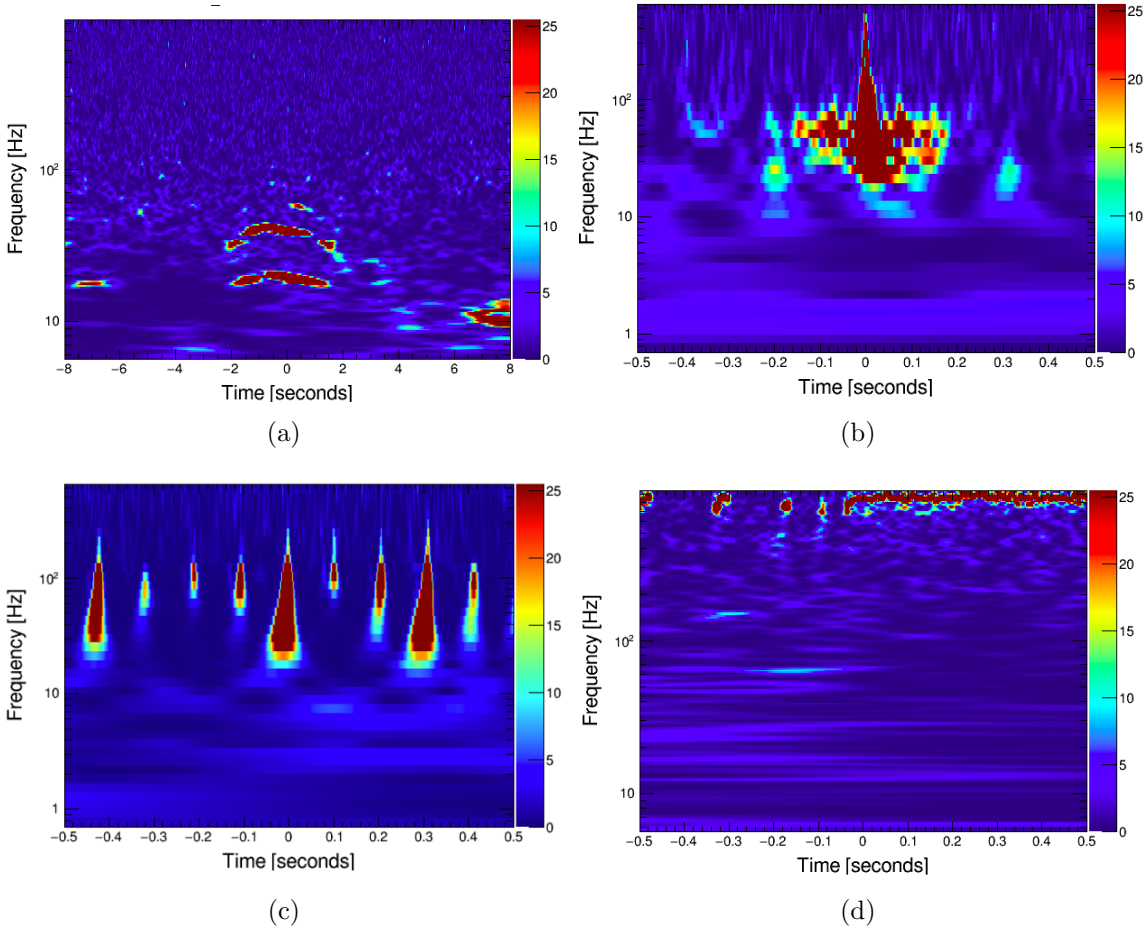

Figure 3.11: The time-frequency morphology of some common glitch types found in aLIGO Hanford data during the first observing run. (a) Glitches created by scattering of light in the detector. (b) This is a sub-type of blip glitches known as Koi fish due to the "fins" on each side of the glitch. (c) Blip glitches that occur repeatedly on a short time scale. (d) Glitches that occur at high frequencies.

to be detected.

Hardware injections are found in both detectors, with 23 in L1, and 17 in H1, and are classified into the chirp glitch category. Scattered light occurs in both detectors, but not very often at an SNR larger than the threshold used by PCLIB for classification. Glitches with an SNR large enough for them to saturate a spectrogram are in the extremely loud glitch type. Both detectors contain repeating blips, as shown in Figure 3.11(c). The helix, blue mountain and whistle glitches are only found in the Livingston detector.

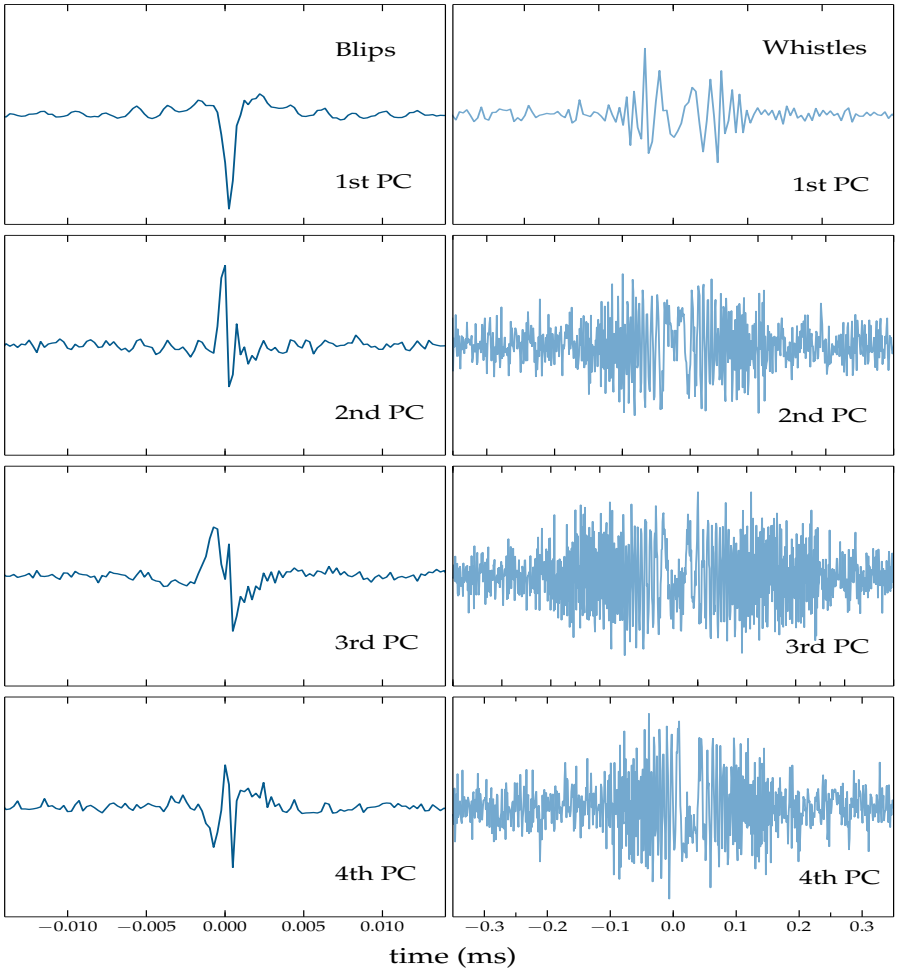

Figure 3.12: The first four PCs for the blip glitches (left), and the whistle glitches (right). Blip glitches are the most common glitches in both of the aLIGO detectors and often appear as a spike in the time series. Whistles glitches are higher in frequency and longer in duration than the blip glitches. Higher order PCs consist of mainly noise, and they can degrade classification results if they are not discarded.

3.5.1 Potential Impacts of Glitch Types.

In this sub-section, we study the impact of different glitch classes and glitch classification on the searches and parameter estimation for transient GWs, by simulating GW signals and examining the impact that glitches have on those signals. During O1, three different types of vetoes were applied to the detector data. The first, known as category 1 vetoes, are applied before any of the data is analysed by the GW searches. Category 1 vetoes remove the worst high SNR noise that is clearly coupled with environmental sensors at the detector sites. Category 2 vetoes remove other less severe glitches with a known coupling mechanism, and are applied after the data has been analysed. This is because cutting out multiple short segments

Glitch Class	Total	Livingston	Hanford
blip	5429	1598	3831
chirp	40	23	17
scattering	58	21	37
extremely loud	1195	349	846
high freq	1454	0	1454
repeating	393	36	357
no glitch	1012	286	726
helix	12	12	0
blue mountain	10	10	0
whistles	11	11	0

Table 3.1: The PC-LIB glitch classification results for O1. The numbers show how many of each glitch type is found in each detector. The blip glitch is the most common glitch in both aLIGO detectors. The chirp class contains mainly hardware injections. Helix, blue mountain and whistles were found only in the Livingston detector. The extremely loud glitches are removed from the searches by data quality vetoes.

of data can have a negative effect on the searches for transient signals, as the CBC searches require 2064 s of continuous data, and the searches for GW bursts require 620 s of continuous data [66]. Category 3 vetoes are for glitches that only occur in data that is sensitive to GWs, and cannot be vetoed using auxiliary channels. This type of glitch is a particular problem for searches for GW transients, as they create large tails in the search backgrounds [66].

No glitches were found near the GWs detected in O1. However, as the rate of glitches is high, and the number of detections is expected to increase, it is possible that a signal may occur close to a glitch in the future. Using the lists of glitch types classified in O1, the effect that different glitch classes may have on the estimated parameters of a detected burst signal is investigated. As no clues to the origin of some of the glitch types (e.g. the blip glitches) have been discovered so far, it remains likely that most of the glitch types will still be present during O2 and O3, and that the results will be a good approximation of what is expected in future observing runs.

This type of study can help the detector characterisation team decide which glitches should take priority in targeted efforts to eliminate them, and help in deciding if a new type of veto is needed for a particularly troublesome glitch type. The worst glitch types for the transient searches are already well known, but it is possible that the worst glitch types for parameter estimation may be different. It may also be possible to subtract the waveform of the glitch from the data near the

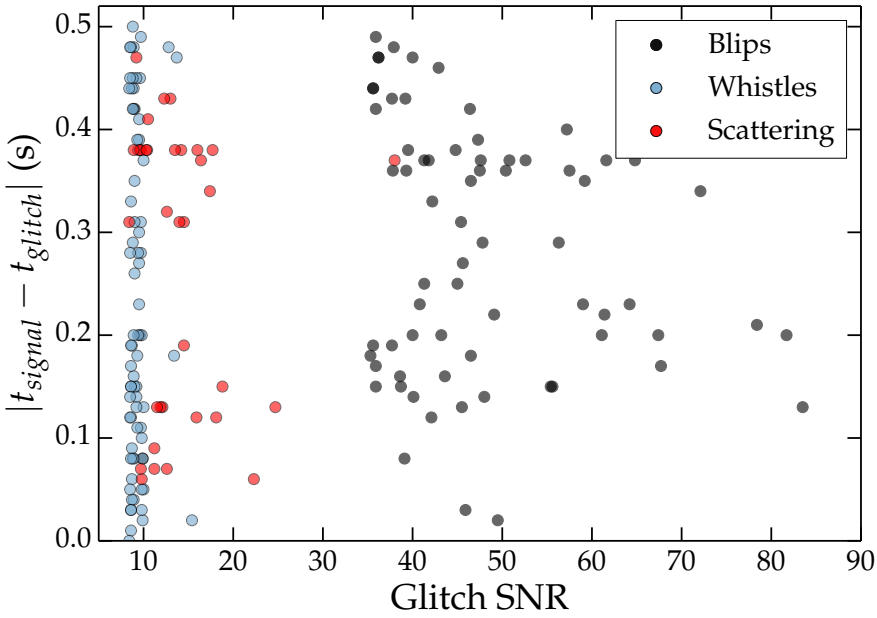

Figure 3.13: The time difference between glitches and injected sine Gaussian signals, and the glitches SNR values. All of the glitches are within half a second of the signal time. The whistles are low SNR and long duration. The blips are high SNR and short duration.

signal in an effort to further improve parameter estimation results.

Sine Gaussian signals, as defined in Equation 2.27, are simulated to mimic potential burst GW signals, with the parameters Q = 5, frequency = 200 Hz and hrss = 8.0×10^{-23}. This puts the signals in the most sensitive frequency band for aLIGO, and gives the signals a short duration of 5.6 ms, making them an ideal source for short duration burst searches. The signals are added to the O1 data, *injected*, within 0.5 s of a blip glitch, whistle glitch or scattered light. The signals are distributed uniformly on the sky, and then the sky position is altered afterwards to give all of the signals an SNR of 17. The SNR values of the two 5σ detections made during O1 were SNR 24 and SNR 13 for GW150914 and GW151226, respectively. Therefore, SNR 17 is used as this is a reasonable value to expect for a 5σ detection.

The SNR of the glitches, and the time difference between the glitches and the injected signals are shown in Figure 3.13. All of the glitches are in L1 only, and the GW signal is injected into both L1 and H1 data. As good data in H1 is needed at the same time as the L1 glitches, suitable times are found for 73 whistle glitches, 74 blip glitches and 34 instances of scattering. An SNR of 17 makes the signals larger than all of the whistles, larger than 27 of the scattered light glitches, and smaller than 71 of the blip glitches. Included in those glitches are some found by

the citizen science project Gravity Spy [92], as described in Section 2.3.3, so that glitches below the SNR 12 cut-off used by PC-LIB during O1 can be included.

The `LALInference-burst` parameter estimation algorithm [34, 44], which uses a sine Gaussian signal model, is used to recover the values of Q, frequency and hrss of the injected signals using a nested sampling method, as described previously in Section 2.2.1. The signals are injected into Gaussian noise with the same sensitivity as O1, to compare the results of the signals in glitchy data to signals in clean data. Flat priors are used for frequency and Q, with limiting values of 30 Hz to 2000 Hz, and 2 to 60, respectively. A uniform in volume prior is used for hrss, and a uniform on the sky prior is used to estimate the sky position. We analyse 3 s of data around the signal using 512 live points.

Blip glitches

Figure 3.14 shows the peak values of the posterior distributions for the Q, frequency and loghrss parameters within half a second of a blip glitch. The grey histograms are the posterior peaks obtained when no glitches are present. The blue histograms show how the recovered values change when a glitch occurs within half a second of the signal. The dashed lines show the true values of the signal parameters. Figure 3.14(a) shows the peak values of the Q posterior distributions for all of the injected signals, Figure 3.14(b) shows the peak values of the frequencies posterior distributions for all injections, and Figure 3.14(c) shows the peak values of the loghrss posterior distributions for all signals.

There are 7 signals which have posterior peak values for the quality factor outside of the range expected from signals in clean data. They are signals where the blip glitch is less than 0.15 s away from the signal. An example posterior for one injection is shown in Figure 3.14(d). The blip glitch has shifted the whole posterior distribution to lower values, but did not significantly alter the posterior widths for any of the measured parameters. The change in the frequency posteriors created by the blip glitch was not as large as for the other parameters. The largest change in frequency was for the signals with glitches 0.02 s, 0.08 s and 0.13 s away from the signal. The loghrss peak posterior values have four injections that are much louder than the others when a blip glitch is near. The three largest loghrss values are for signals with glitches at 0.02 s, 0.03 s and 0.08 s away from the signal. The fourth

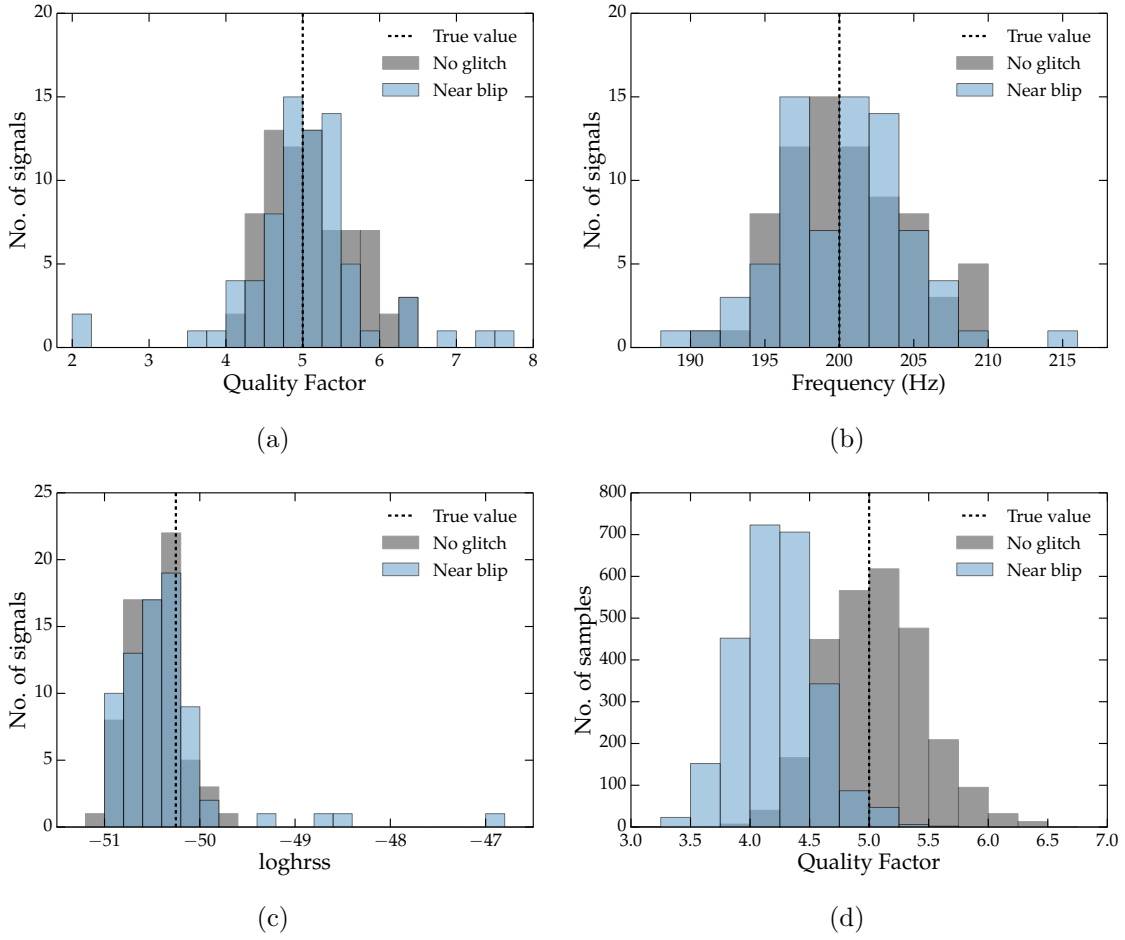

Figure 3.14: The recovered parameters of sine Gaussian signals with a blip glitch within half a second of the signal. The top two figures, and the bottom left figure, show the peaks of the posterior distributions for the recovered parameters for all of the injections. The dotted line is the true value. The grey values are from signals injected in Gaussian noise, and the blue values are for signals within half a second of a blip glitch. The bottom right shows an example posterior for the Q value of one signal. Blip glitches close to the signal can change the recovered duration and frequency, and increase the measured amplitude of the signal.

largest has a glitch at a much larger distance away from the signal at 0.44 s, but the glitch also has a much larger amplitude, with an SNR above 80.

Scattered light

In Figure 3.15, the peak values of the posterior distributions are shown for the Q, frequency and loghrss parameters of sine Gaussian signals, which occur within half a second of scattered light. As for the blip glitches, the grey histograms are the values obtained when no glitches are present, and the blue histograms show how the

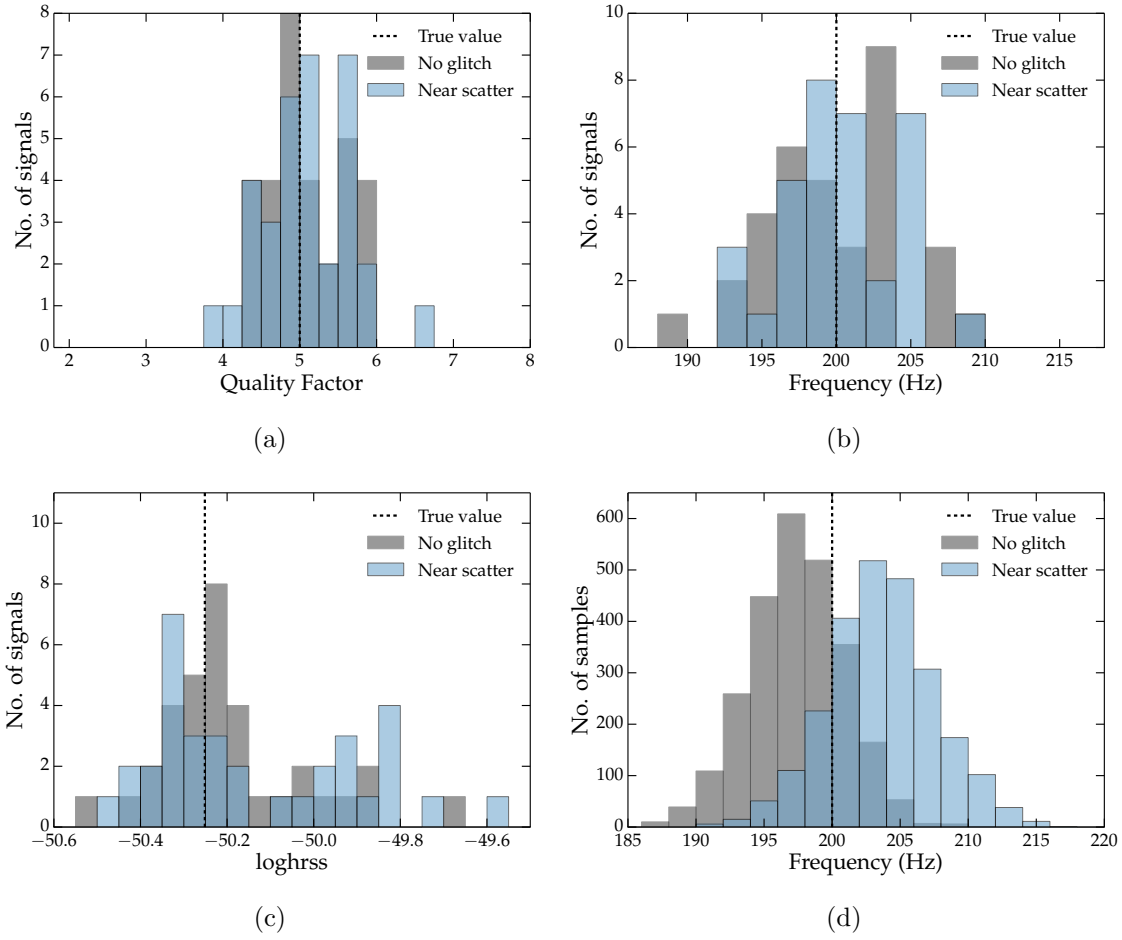

Figure 3.15: The recovered parameters of sine Gaussian signals with scattered light within half a second of the signal. The top two figures, and the bottom left figure, show the peaks of the posterior distributions for the recovered parameters for all of the injections. The dotted line is the true value. The grey values are from signals injected in Gaussian noise, and the blue values are for signals within half a second of a blip glitch. The bottom right shows an example posterior for the frequency value of one signal. The effect of the scattering was not as large as for other types of glitches.

peak posterior values change when a glitch occurs within half a second of the signal. The dashed lines show the true values of the signal parameters. The change in the distribution of the peaks of the posteriors is not as large as for the blip glitches. The worst Q posterior peak values are for signals with scattered light within 0.07 s and 0.13 s of the signal. The reduction in the effect produced by this type of glitch on the estimated signal parameters may be due to the glitches SNR being much lower than the SNR of the signal.

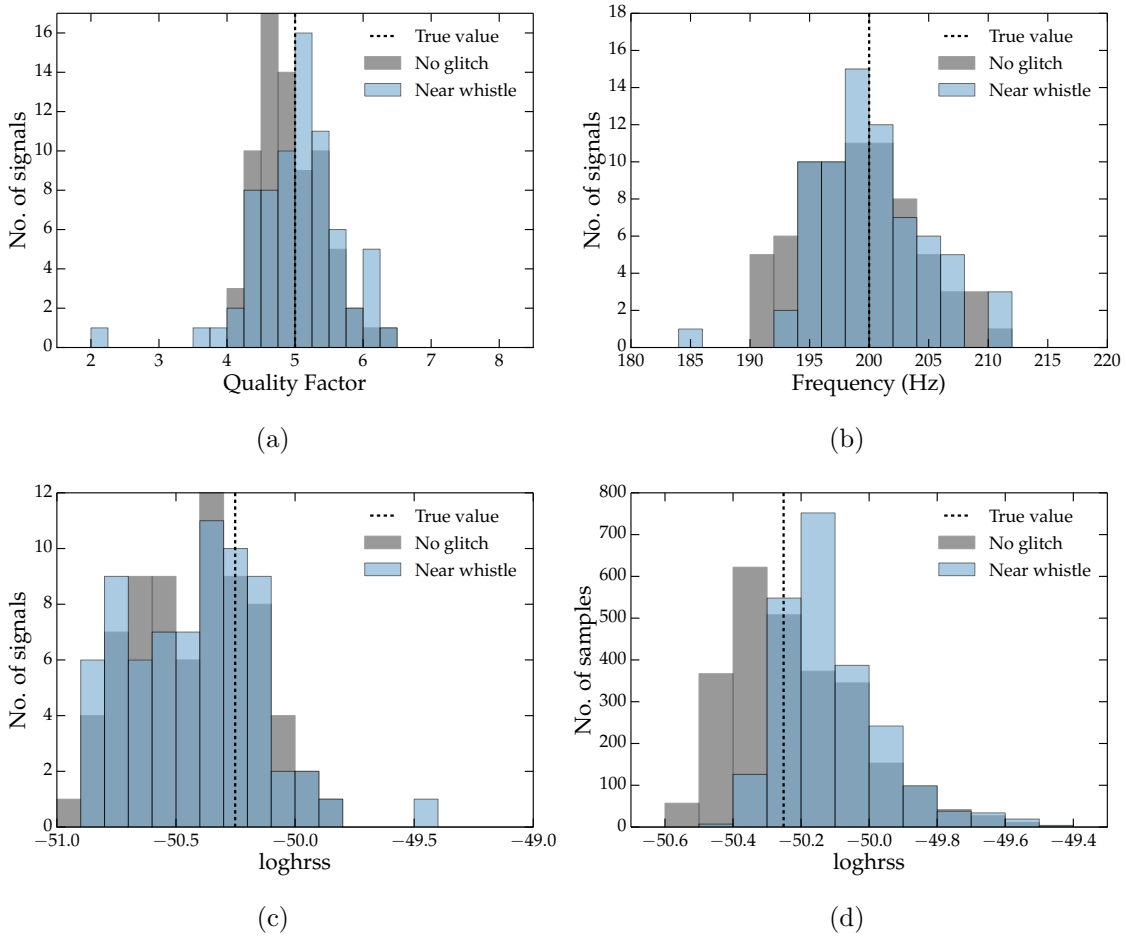

Figure 3.16: The recovered parameters of sine Gaussian signals with a whistle glitch within half a second of the signal. The top two figures, and the bottom left figure, show the peaks of the posterior distributions for the recovered parameters for all of the injections. The dotted line is the true value. The grey values are from signals injected in Gaussian noise, and the blue values are for signals within half a second of a blip glitch. A few of the worst recovered values are not shown in the figures as they are off the scale of the plot. They are one Q value at 60, two frequency values at 30 Hz and 77 Hz, and a loghrss value of -43.6. The bottom right shows an example posterior for the log of the hrss value of one signal.

Whistles

The effects of whistle glitches on the measured parameters are shown in Figure 3.16. The whistle glitches have the worst effect on the measured parameters of the signals, even though they have the lowest SNR of all the glitches examined in this section. This may be due to the whistle glitches having a longer waveform and a higher frequency than most other glitch types, as shown in Figure 3.12. This means that the whistles can be further away from the signal and still have a negative effect on the parameters. The two worst signals have Q posterior peaks of 59.9 and 2, peak posterior frequencies of 30 Hz and 77 Hz, and peak posterior loghrss values of

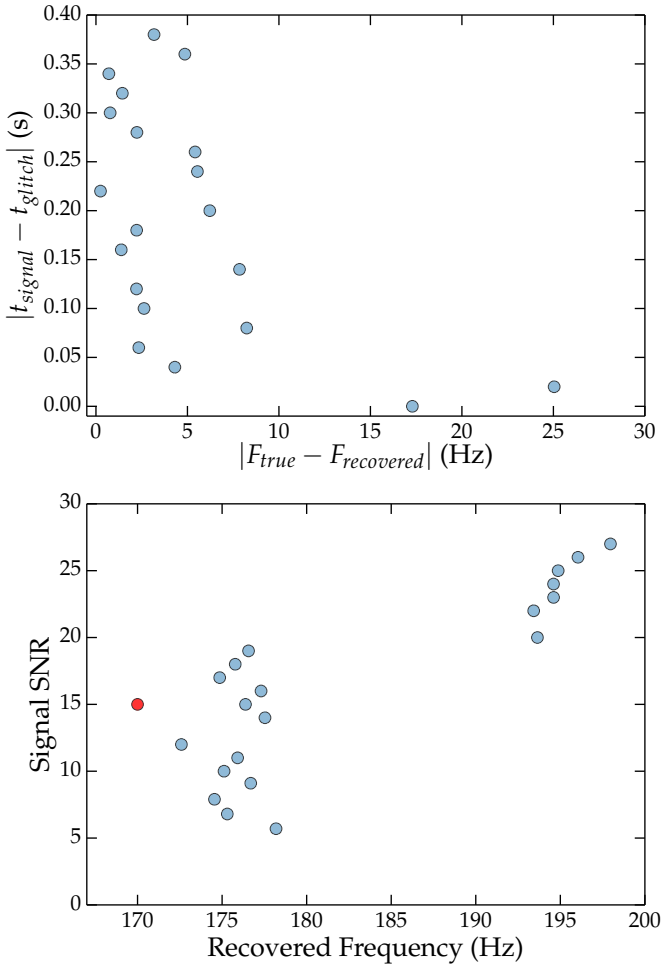

Figure 3.17: The effects on measured signal parameters produced by blip glitches at different distances and SNR values. The top figure shows how the difference in time between a glitch and signal effects the measured frequency of the signal. The injected signal was SNR 17. The error is only large when the glitch is less than 0.04 s away from the signal. The bottom figure shows how the SNR of a signal relative to a glitch effects measured signal parameters. The red dot shows the blip glitch SNR and frequency. The glitch is 0.02 s away from the signal for all points. The peak of the frequency posterior only becomes close to the true value when the signal is much larger than the glitch.

-43.6 and -47, and were 0.30 s and 0.42 s away from the glitches, with SNR values of 9.5 and 8.8, respectively. The other signals with peak posterior values for Q that were lower than expected, as shown in Figure 3.16(a), were all 0.08 s away from the glitches.

For all of the glitch types considered, the effect on the parameters is strongly influenced by the proximity of the glitch to the signal, and the difference in glitch SNR and signal SNR. This is illustrated in Figure 3.17. In the top figure, one SNR 15 blip glitch is selected and an SNR 17 sine Gaussian signal is injected near the blip, at distances that increase in 0.02 s intervals. The figure shows how large the

peak posterior frequency value is compared to the injected value of 200 Hz, as the signals distance in time from the glitch increases. The peak posterior values only have a large error when the signal is within 0.04 s of the glitch.

The bottom panel in Figure 3.17, shows the effect of the SNR of the glitch on the frequency peak posterior values. The red dot shows the SNR and frequency of the blip glitch. All of the signals are injected at a distance of 0.02 s from the glitch. The SNR of the signal is then gradually increased by increasing the amplitude of the signal. Below SNR 20, all of the frequency peak posterior values are closer to the value of the glitch than the signal. As the SNR increases above 20, the frequency peak posterior values change to the values that would be expected if no glitch was present. The results show that if the SNR of the glitch is bigger than the signal, then it may be beneficial to remove the glitch from the data before measuring the parameters of the detected signal. Longer duration signals created the biggest change in the parameter estimation results. However, as the blip glitches are often higher in SNR, and occur more frequently than the other glitch types, they are likely to create the largest error in estimated parameters of future detections.

3.6 Summary and Discussion

Non-Gaussian noise in the aLIGO and AdVirgo detectors can potentially mimic a GW signal, reduce the duty cycle of the instruments, and decrease the sensitivity of the detectors. Classification of different glitch types can help identify their origins and lead to a reduction in their number. We have developed a method for the automatic classification of glitches called PC-LIB. In the previous chapter, we demonstrated the performance of PC-LIB on simulated glitches in simulated Gaussian aLIGO noise. However, as real noise from the advanced detectors is non-stationary and non-Gaussian, a better understanding of how the method would perform during the aLIGO observation runs was required.

In the ER7 data used to test PC-LIB, there were 6 glitches that were missed and 95% of the remaining glitches were classified correctly. A similarly high efficiency was obtained by other methods used in a glitch classification comparison study. All of the methods used for glitch classification in aLIGO and AdVirgo data have a high efficiency in real, non-stationary, non-Gaussian detector noise. The efficiency

of the WDF-ML algorithm is reduced for the H1 glitches, because the duration of the glitches becomes much larger than the analysis window, which reduces the efficiency of the overall classification. WDF-ML can classify lower frequency glitches than the other two methods. PC-LIB is better able to classify longer duration glitches, due to its longer analysis window. PCAT can classify new types of glitches as soon as they appear in the data, and can potentially provide glitch waveforms for PC-LIB's signal models. Because of the different strengths and weaknesses of the different methods, having multiple classifiers is a winning strategy.

PC-LIB was used to classify glitches during O1. All glitches above SNR 12 were classified. As during ER7, the rate of glitches during O1 was much higher in H1, which contained 3831 glitches, than in L1, which contained 1598 glitches. The blip glitch was found to be the most common glitch in both of the detectors. Since glitches, such as the blips, are rarely removed by data quality vetoes, their accurate classification is crucial for the improvement of GW searches, as an accurate categorization will allow us to search for couplings within the detector [41, 66]. Classification of shorter duration glitches is more important, as they have a higher impact on the GW search backgrounds [2, 19].

The O1 classification results were then used to examine the effects of different glitch types on the estimated parameters of a GW burst signal. It was found that with width of the posterior distributions do not change when a glitch is present within half a second of the signal, but that the posterior peaks can change to values that are smaller or larger than expected. The change in the posterior peaks of the parameters is greatest when the signal occurs within 0.15 s of a glitch, and when the glitch SNR is louder than the signal SNR. If the SNR of the glitch is bigger than the signal, then it may be beneficial to remove the glitch from the data before measuring the parameters of the detected signal.

Chapter 4

Model Selection and Parameter Estimation for Core-Collapse Supernovae

4.1 Introduction

Core-collapse supernovae (CCSN) have long been considered as a potential source for advanced GW detectors [100]. Although no CCSN were found in initial detector science runs, previous studies have shown that an advanced detector network could detect these sources out to the Large Magellanic Cloud (LMC) [51, 46]. A CCSN would be an ideal multi-messenger source for aLIGO and AdVirgo, as neutrino and electromagnetic counterparts to the signal would be expected. The GWs are emitted from deep inside the core of the CCSN, which may allow astrophysical parameters to be measured from the reconstruction of the GW signal. In this chapter, we investigate Bayesian parameter estimation, and Bayesian model selection techniques, for CCSN signals detected with an aLIGO and AdVirgo detector network.

This chapter is structured as follows: In Section 4.2, we provide an overview of CCSNe and their associated GW emission. This includes a description of the GW CCSN waveforms used in this thesis. In Section 4.3, we describe the model selection and parameter estimation code, the Supernova Model Evidence Extractor

(SMEE), which we use to carry out a model selection study. In Section 4.4, we provide details of the three detector network analysis. In Section 4.5, we carry out a careful selection of the ideal number of PCs. In Section 4.6, we show the behaviour of SMEE when no signal is present in the data, and the minimum SNR needed for SMEE to detect a CCSN signal is investigated. In Section 4.7, we show the results for signals injected at Galactic and extra Galactic distances. The robustness of the method is tested in Section 4.8. A summary and discussion of the implications is given in Section 4.9.

4.2 Core-Collapse Supernovae and their Gravitational-Wave Emission

Zero age main sequence (ZAMS) stars, with masses $8\,\mathrm{M}_\odot < \mathrm{M} < 100\,\mathrm{M}_\odot$, form electron-degenerate cores. The stars nuclear burning stops when the core of the star is composed of iron nuclei, and then collapses when the stars core mass reaches the Chandrasekhar mass ($1.44\,\mathrm{M}_\odot$) [101, 102]. The collapse of the core will continue until the core reaches nuclear densities. The equation of state (EOS) stiffens above nuclear density, the inner core then rebounds, and a shock wave is launched outwards from the outer edge of the inner core. The shock then loses energy by nuclear dissociation and the emission of neutrinos from the optically thin regions. The shock then stalls and becomes an accretion shock, which must be revived within $\sim 0.5 - 3\,\mathrm{s}$, or the star will not explode, and will form a black hole as matter is accreted back on to the proto-neutron star [103]. The mechanism needed to revive the shock, in order to explode the star, is currently not well understood, and is a problem that may be solved with GWs, if a detection of a CCSN is made with advanced GW detectors.

In this section, we consider the magnetorotational and neutrino CCSN explosion mechanisms. We describe the physical processes involved in the explosions, and give a description of a selection of GW waveforms associated with each mechanism, which are used for model selection later in this chapter. Numerical simulations of CCSN have advanced rapidly in recent years, and a number of different features expected in the GW signal have been identified. They include rotating core collapse and bounce, rotational instabilities, neutrino-driven convection, prompt convection

in the region behind the shock, standing accretion shock instability (SASI), and asymmetric neutrino emission [40]. A combination of these processes could occur in a CCSN.

4.2.1 The Magnetorotational Mechanism

Rapidly-rotating CCSNe are highly energetic, and may be associated with high energy events, such as hypernovae and gamma ray bursts. Rapid-rotation is only expected in a small number, $\leq 10\%$, of progenitor stars [104, 105]. Theory and simulations have shown that magnetorotational processes could extract rotational energy and drive a jet-driven bipolar explosion [106, 107]. When core-collapse to a proto-neutron star occurs, it may result in spin-up of the stellar core by a factor of ~ 1000 [108]. The rapidly-rotating pre-collapse core results in a millisecond period proto-neutron star, which if combined with a magnetar strength magnetic field could power a strong CCSN explosion. For the magnetorotational mechanism to work, simulations suggest that the pre-collapse core needs a spin period of $\lesssim 4-5\,\mathrm{s}$, and a magnetic field of order $10^{15}\,\mathrm{G}$ [107]. This value is larger than predicted by stellar evolution models [104]. Therefore, some magnetic field amplification may be necessary after core bounce, which could be created by rotational winding of the magnetic field, or through magnetorotational instabilities [109, 110].

Some example rapidly-rotating CCSN GW signals, hereafter referred to as the `RotCC` model, are shown in Figure 4.1. Rapidly-rotating CCSN signals are dominated by the bounce and subsequent ring down of the proto-neutron star. Typically, the peak GW strain from rotating core-collapse is $\sim 10^{-21} - 10^{-20}$, for a source at $10\,\mathrm{kpc}$, and emitted energy in GWs (E_{GW}) is $\sim 10^{-10} - 10^{-8}\,M_{\odot}$. The GW energy spectrum is more narrowband than for non-rotating core-collapse, with most power emitted between $500 - 800\,\mathrm{Hz}$, over timescales of a few tens of ms. For pre-collapse cores with an initial spin period less than $\sim 0.5 - 1\,\mathrm{s}$, core bounce occurs slowly at subnuclear densities, dynamics are dominated by centrifugal effects, and most energy in GWs is emitted around $\sim 200\,\mathrm{Hz}$ [40, 111]. In the remainder of this section, we describe the rotating core-collapse waveforms used in this thesis chapter.

The Dimmelmeier *et al.* [111] waveform catalogue contains 128 two-dimensional waveforms, with progenitor star ZAMS mass values of $12\,\mathrm{M}_{\odot}$, $15\,\mathrm{M}_{\odot}$, $20\,\mathrm{M}_{\odot}$, and $40\,\mathrm{M}_{\odot}$, varying angular momentum distributions, and two different nuclear matter

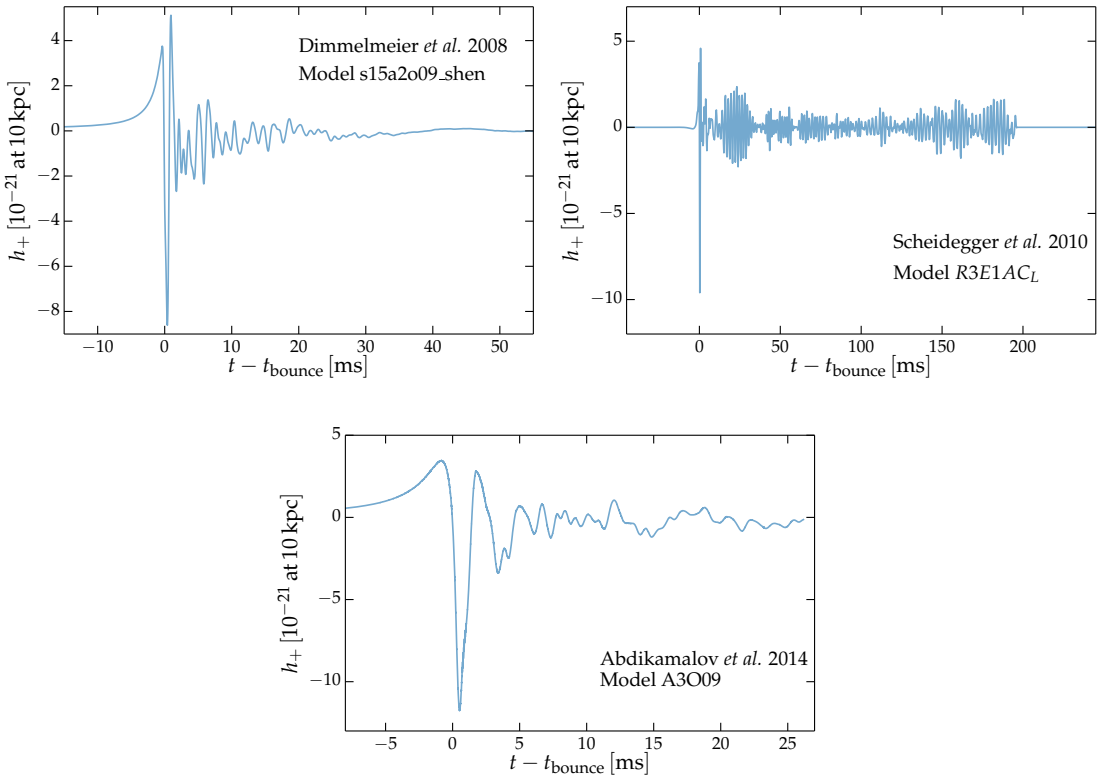

Figure 4.1: Time series GW h_+ strain for representative models of GWs from rotating core collapse, as seen by an equatorial observer at 10 kpc. The top left is a representative 2D waveform from the Dimmelmeier *et al.* [111] waveform catalogue. The top right is a representative 3D waveform from the Scheidegger *et al.* [112] waveform catalogue. The bottom sub-figure is a representative 2D waveform from Abdikamalov *et al.* [113]. The GW strain from rotating core-collapse is an order of magnitude larger than the typical GW strain from neutrino-driven explosions. Figure reproduced from [9].

EOS. They are the Lattimer-Swesty EOS [114], and the Shen EOS [115, 116]. The initial angular momentum distribution of the pre-collapse core is imposed through an angular velocity profile, $\Omega_i(\bar{\omega})$, defined as,

$$\Omega_i(\bar{\omega}) = \frac{\Omega_{c,i}}{1 + (\bar{\omega}/A)^2}\,, \tag{4.1}$$

where $\bar{\omega}$ is the cylindrical radius, $\Omega_{c,i}$ is the central angular velocity, and A is the differential rotation length scale. Simulations are performed across the angular momentum distribution space, considering strongly differential rotation ($A = 500\,\mathrm{km}$) to almost uniform rotation ($A = 50000\,\mathrm{km}$); and slowly rotating ($\Omega_{c,i} = 0.45\,\mathrm{rad\,s^{-1}}$) to rapidly rotating ($\Omega_{c,i} = 13.31\,\mathrm{rad\,s^{-1}}$) pre-collapse cores. As the simulations are axisymmetric, the waveforms are linearly polarized. A representative waveform from the Dimmelmeier *et al.* catalogue is shown in the top left panel of Figure 4.1. As the main feature of the Dimmelmeier waveforms is the spike at core bounce, they

are still a good approximation of a three-dimensional CCSN signal, as any rotating three-dimensional model stays sufficiently close to axisymmetry around the bounce signal and non-axisymmetric features only start to appear a few milliseconds after the bounce [112].

Abdikamalov *et al.* [113] performed two-dimensional, general-relativistic, hydrodynamic, rotating core-collapse simulations. They use a $15\,\mathrm{M}_\odot$ progenitor star, and the Lattimer-Swesty EOS [114]. A typical waveform from the Abdikamalov catalogue is shown in the bottom panel of Figure 4.1. The Abdikamalov waveforms are very similar in duration, amplitude and time series morphology to the Dimmelmeier waveforms. In this chapter, we use waveforms $A1O14$ ($A = 300\,\mathrm{km}$; $\Omega_c = 14\,\mathrm{rad\,s^{-1}}$), $A3O09$ ($A = 634\,\mathrm{km}$; $\Omega_c = 9\,\mathrm{rad\,s^{-1}}$), and $A4O01$ ($A = 1268\,\mathrm{km}$; $\Omega_c = 1\,\mathrm{rad\,s^{-1}}$), referred to as `abd1`, `abd2`, and `abd3`, respectively.

Scheidegger *et al.* [112] performed three-dimensional magnetohydrodynamical simulations of 25 GW signals, using a leakage scheme for neutrino transport. They use a $15\,\mathrm{M}_\odot$ progenitor star, and the Lattimer-Swesty EOS [114]. Due to the three-dimensional nature of the simulations, the Scheidegger *et al.* waveforms have two GW polarizations. The waveforms contain only h_+ around the spike at core bounce, and the $\mathrm{h}_\times$ polarisation starts a few ms later. In this chapter, we use waveform models $R3E1AC_L$ (moderate pre-collapse rotation, toroidal/poloidal magnetic field strength of $10^6\,\mathrm{G}/10^9\,\mathrm{G}$), shown in the top right panel of Figure 4.1, and $R4E1FC_L$ (rapid pre-collapse rotation, toroidal/poloidal magnetic field strength of $10^{12}\,\mathrm{G}/10^9\,\mathrm{G}$). We hereafter refer to these waveforms as `sch1` and `sch2`, respectively. The Scheidegger waveforms are much longer than the Abdikamalov and Dimmelmeier waveforms, but are similar in amplitude.

4.2.2 The Neutrino Mechanism

The neutrino-driven CCSN explosion mechanism is currently accepted as the most likely explosion mechanism for CCSNe. The neutrino mechanism was first proposed by Arnett [117], and Colgate and White [118], and a more modern form of the mechanism was first put forward by Bethe and Wilson [119]. Current reviews of the mechanism are given in [120, 121]. Neutrinos contain most of the energy, $\sim 99\%$, released during the core-collapse [102]. The neutrino mechanism involves some of the energy from the neutrinos being reabsorbed behind the shock to power the

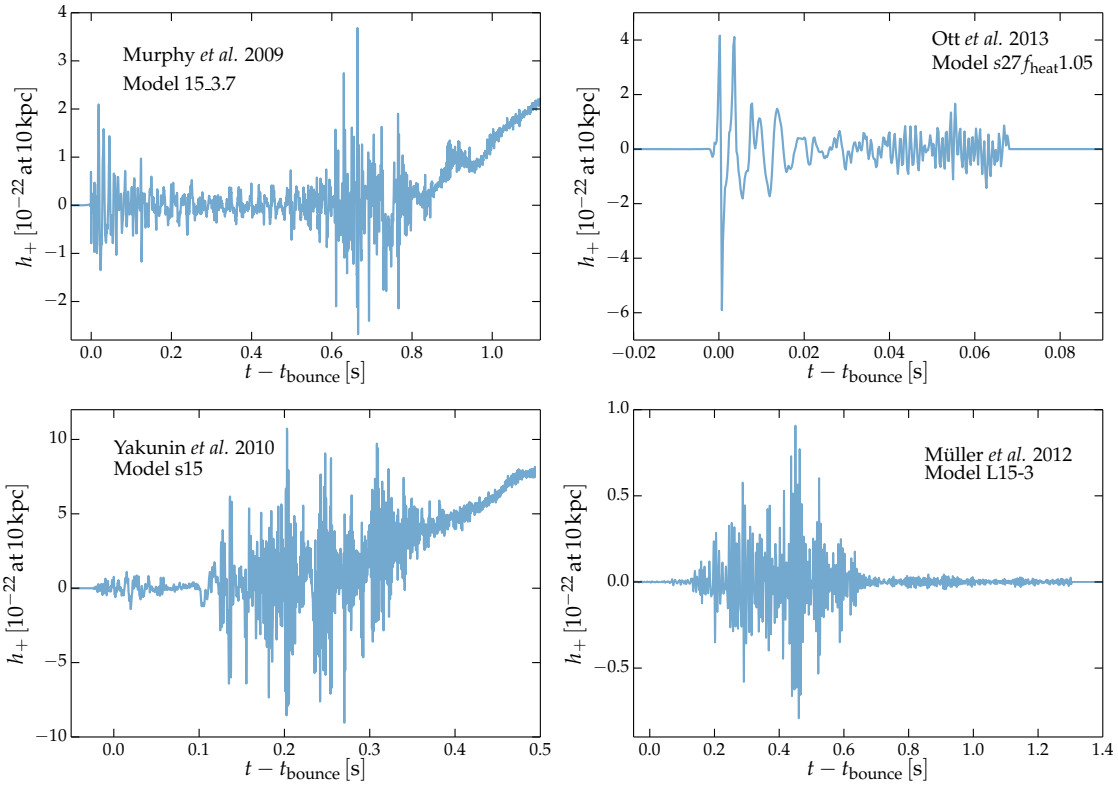

Figure 4.2: Time series GW h_+ strain for representative waveform models of neutrino-driven convection, as seen by an equatorial observer at 10 kpc. The top left is a representative waveform from the Murphy *et al.* [127] waveform catalogue. A representative waveform from the Ott *et al.* [128] waveform catalogue is in the top right. A $15\,M_\odot$ progenitor from Yakunin *et al.* [129] waveform catalogue is shown bottom left. The bottom right is a representative waveform from the Müller *et al.* [130] waveform catalogue. The typical GW signal duration is roughly an order of magnitude longer for neutrino-driven explosions than for rotating core collapse. Figure reproduced from [9].

explosion.

The GW signal from neutrino-driven CCSNe, hereafter referred to as the `C&S` model, is dominated by contributions from turbulent convection and the SASI [122, 123, 124, 125, 126]. Some example neutrino mechanism GW waveforms are shown in Figure 4.2. The GW signal is broadband in frequency, with most emission between $100-1100\,\mathrm{Hz}$. The signal typically lasts from $\sim 0.3-2\,\mathrm{s}$, with strain $\sim 10^{-22}$ for a source at 10 kpc. The total E_{GW} from neutrino-driven explosions are of order $10^{-11}-10^{-9}\,M_\odot$. The typical GW signal duration is roughly an order of magnitude longer for neutrino-driven explosions than for rotating core-collapse, and the amplitude is smaller than for rotating core-collapse waveforms. The remainder of this section describes the neutrino mechanism waveforms used in this thesis chapter.

The Murphy *et al.* [127] catalogue contains 16 waveforms, extracted using the

quadrupole approximation [131], from axisymmetric Newtonian CCSN simulations. Electron capture and neutrino leakage are treated using a parametrised scheme, and only the monopole term of the gravitational potential is included. The progenitor models considered are non-rotating, with ZAMS mass values of $12\,M_\odot$, $15\,M_\odot$, $20\,M_\odot$, and $40\,M_\odot$. A representative waveform from the Murphy *et al.* catalogue is shown in the top left panel of Figure 4.2, as seen by an equatorial observer at 10 kpc. Due to the axisymmetric nature of the simulations, the waveforms extracted are linearly polarized.

The Yakunin *et al.* [129] catalogue contains waveforms simulated by axisymmetric Newtonian simulations, using an approximate general relativity monopole term of the gravitational potential, and including radiation-hydrodynamics. Due to axisymmetry, the extracted waveforms are linearly polarized. They are complete waveforms that all explode successfully. They use three different ZAMS masses of $12\,M_\odot$, $15\,M_\odot$ and $25\,M_\odot$, and find a clear GW signal that is composed of four different parts. They are a weak prompt signal, a quiescent stage, a strong signal where most of the GWs are emitted, and a slowely increasing tail. An example Yakunin waveform, the $15\,M_\odot$ progenitor, is shown in the bottom left panel of Figure 4.2, showing all of the four stages. In this chapter, we use the waveform obtained from the $15\,M_\odot$ progenitor star simulation, which we refer to as `yak`.

Müller *et al.* [130] performed three-dimensional simulations of neutrino-driven CCSNe with gray neutrino transport and an inner boundary condition to prescribe the contraction of the proto-neutron star core. They started the simulations after core bounce, and assumed a time-varying inner boundary, cutting out much of the proto-neutron star. There are three waveform models, L15-3 and W15-4 (both with a $15\,M_\odot$ progenitor), and model N20-2 (with a $20\,M_\odot$ progenitor). In this chapter, we refer to these waveforms as `müller1`, `müller2` and `müller3` respectively. An example waveform, the L15-3 model, is shown in the bottom right panel of Figure 4.2. As the simulations are three-dimensional, the Müller *et al.* waveforms have two GW polarizations. Prompt convection only contributes to the waveforms at late times, and the contraction of the proto-neutron star lowers the GW frequency. The simulations were stopped 15 ms after bounce.

Ott *et al.* [128] performed three-dimensional simulations of neutrino-driven CCSNe using a $27\,M_\odot$ progenitor star, based on model s27 of Woosley *et al* [132]. The simulations are general-relativistic and incorporate a three-species neutrino

leakage scheme. They produce the first GWs from three-dimensional general-relativistic models. There are four GW signals, with two polarisations, produced with four different scaling factors for the neutrino heating rate. They are models $s27f_{\rm heat}1.00$, $s27f_{\rm heat}1.05$ shown in the top right panel of Figure 4.2, $s27f_{\rm heat}1.10$, and $s27f_{\rm heat}1.15$. In this chapter, we use model $s27f_{\rm heat}1.05$, and hereafter refer to this waveform as `ott`.

4.3 The Supernova Model Evidence Extractor

In this section, we introduce the Supernova Model Evidence Extractor (SMEE). SMEE is designed as a parameter estimation follow-up analysis for possible supernova detection candidates identified by GW burst searches. Its primary goal is to identify the CCSN explosion mechanism. It is not possible to gain information on the CCSN explosion mechanism from electromagnetic (EM) observations, as EM emission from CCSNe occurs in optically thin regions, far from the central engine. GWs and neutrinos, however, are emitted from deep inside the core and, as such, they are direct probes of the CCSN explosion mechanism. As supernova simulations have not advanced far enough for robust estimates of the signal's phase evolution, matched filtering (the optimal linear search method for known signals in Gaussian noise [133]) cannot be used. The first attempt to reconstruct a CCSN GW signal without knowledge of the waveform was carried out by Summerscales *et al.* [134]. A more recent study of CCSN waveform reconstructions, with minimal signal assumptions, was carried out by McIver [135].

Associating proposed explosion mechanisms with a set of GW emission processes, such that the broad characteristics of GW signals from each mechanism can be determined, can allow the detection of GWs from CCSNe to be used to infer the CCSN explosion mechanism. SMEE applies PCA via singular value decomposition, as described in Section 2.2.2, to catalogues of CCSN waveforms. The PCs can then be linearly combined to create signal models that represent each explosion mechanism. Bayesian model selection via nested sampling, (see Section 2.2.1), can then be applied to determine the most likely explosion mechanism of the GW signal. The first attempt to decompose a CCSN waveform catalogue into its main features was by Brady *et al.* [136], who used a Gram-Schmidt decomposition. Heng [137] was the first to apply PCA to CCSN waveforms, using waveforms from the Dim-

melmeier *et al.* waveform catalogue, and Röver *et al.* [138] were the first to combine PCA with Bayesian data analysis techniques for CCSN waveform reconstruction. Similar techniques have been used to extract physical parameters of GW signals from binary systems [139, 140, 141, 142, 143], and in characterizing noise sources in GW detectors (see Sections 2 and 3 and refs. [7, 8]).

The first application of SMEE to numerical GW waveforms for CCSNe, to infer the CCSN explosion mechanism, was carried out in a proof-of-principal study by Logue *et al.* [75], and considered signals from neutrino-driven convection [127], rapidly-rotating core-collapse [111], and proto-neutron star pulsations (the acoustic mechanism) [144, 100]. There were several major limitations to the first SMEE analysis. Firstly, signals were injected into data for one detector, assuming optimal orientation and sky location for maximal antenna sensitivity of the detector. Given this, the time-varying antenna sensitivity for a given detector was not taken into account, and hence the antenna sensitivity considered was artificially optimistic. The single detector network resulted in limited sensitivity, and only GW signals extracted from axisymmetric CCSN simulations were considered, resulting in linearly polarized signals.

EM observations suggest that many, if not most, CCSN explosions exhibit asymmetric features [145, 146, 147, 148, 149]. The three-dimensional magnetorotational simulations for rapidly-rotating progenitors show a dominant GW polarization is expected for the bounce signal. However, three-dimensional neutrino mechanism simulations show that the stochastic nature of the asymmetric flow structures arising from the SASI and convection will lead to unpolarized GWs from CCSNe [128, 126, 150, 151, 152, 153, 154, 155, 156, 157]. The use of Gaussian noise meant that the effect of glitches present in real GW detector noise could not be studied. Despite these limitations, the SMEE algorithm demonstrated the ability to distinguish magnetorotational explosions within the Milky Way ($\leq 10\,\mathrm{kpc}$), while neutrino-driven and acoustic explosions could be distinguished for sources closer than 2 kpc. This work was further expanded upon in the PhD thesis by Logue [158], where SMEE was updated to allow a multi-detector network analysis.

The goal of this chapter is to address the shortcomings of the original SMEE analysis, and to make more robust statements on the ability to infer the CCSN explosion mechanism from GW observations of CCSNe in the advanced detector era.

4.4 Improvements to Analysis and Simulations

In the previous SMEE analysis, a MATLAB implementation of SMEE was used, which has now been replaced with a faster and more robust C implementation, which is part of the LIGO data analysis software package, the LSC Algorithm Library (LAL) [69]. In particular, we use the `LALInference` package [70, 44, 34], which is designed for parameter estimation of GW signals.

Several other improvements to the SMEE analysis are made, designed to address several of the limitations described in the previous sections. In Logue *et al.* [75], simulated Gaussian noise was considered in a single aLIGO detector, in the context of a sky position where antenna sensitivity to linearly polarized GW signals was maximised. Real data from GW detectors is non-stationary and non-Gaussian and, as such, it is important to test the analysis in real non-stationary, non-Gaussian noise. We use the observational data taken by H1 and L1 during the S5 science run, and data taken by Virgo during the VSR1 science run, which is now publicly available via the LIGO Open Science Center (LOSC) [159]. This data is recoloured to the design sensitivity of aLIGO and AdVirgo, as outlined in [46], as this permits a more realistic estimation of the sensitivity of the analysis in future advanced detector observing runs.

The antenna response (see Section 1.3) of the detectors is periodic with an associated time-scale of one sidereal day, due to the rotation of the Earth. As a consequence of this, the sensitivity of any GW analysis using stretches of data much shorter than this time-scale is strongly dependent on the antenna response of the detectors to the source location at the relevant GPS time. To represent time-averaged sensitivity of the detector network, we choose 10 GPS times spread throughout a 24 hour period.

In the following sections, we continue to use linearly polarized GW waveform catalogues to produce the PCs. This is because at the time this study began, large waveform catalogues from three-dimensional CCSN simulations did not exist. This also allows us to compare our results with previous studies. Signals from the acoustic mechanism are no longer considered in this study, as this is no longer considered a viable explosion mechanism for CCSNe [160].

Uniform priors are applied to each PC coefficient, with prior ranges set by the catalogue waveforms padded by $\pm 10\%$ to account for uncertainty due to the lack of available waveforms. A uniform-in-volume prior is applied to the amplitude parameter, as the amplitude scales with distance. We use the multi-detector likelihood function described previously in Equation 2.5. A galactic CCSN will have coincident EM and neutrino signals, ensuring that the sky location of the target source will be known. Online searches for GW bursts can also produce sky-maps of the location of the GW signal [44]. For this reason, we fix the sky location of the source as a known parameter.

4.5 Principal Components

Figure 4.3 shows the first four PCs for the `RotCC` and `C&S` models. The first few PCs represent the main features of the waveform catalogues. It is clear that the time series structure of the `C&S` model is far more complex than that for the `RotCC` model. The main feature of the `RotCC` PCs is clearly the spike at core bounce.

In Logue *et al.* [75], the relative complexity of the `RotCC` and `C&S` models was not taken into consideration when selecting the number of PCs, and an arbitrary number of PCs was chosen. Some attempt at a careful selection of the number of PCs was made in [158], however, as major changes have been made to SMEE since this study, we carry out a new analysis of the ideal number of PCs.

In previous chapters, ideal numbers of PCs were determined by studying the variance encompassed by each PC, and using the number of PCs that cumulatively contain above some fraction of the total variance (see Chapter 2 and refs. [82, 7]). The variance curves for the `RotCC` and `C&S` models are shown in Figure 4.4(c), and Figure 4.4(d), respectively. The variance of the catalogue waveforms is much larger for the `C&S` model. Due to this, fewer `RotCC` PCs are typically needed to faithfully reconstruct GW signals from rotating core-collapse, than the number of `C&S` PCs needed to reconstruct GW signals from neutrino-driven CCSNe. However, as this method only uses the waveforms, it does not account for the limitations of the analysis method implemented in SMEE. Bayesian model selection favours simpler models, and this could increase errors when results are more uncertain, such as when the SNR of the GW signal is low [72]. To account for this, we determine

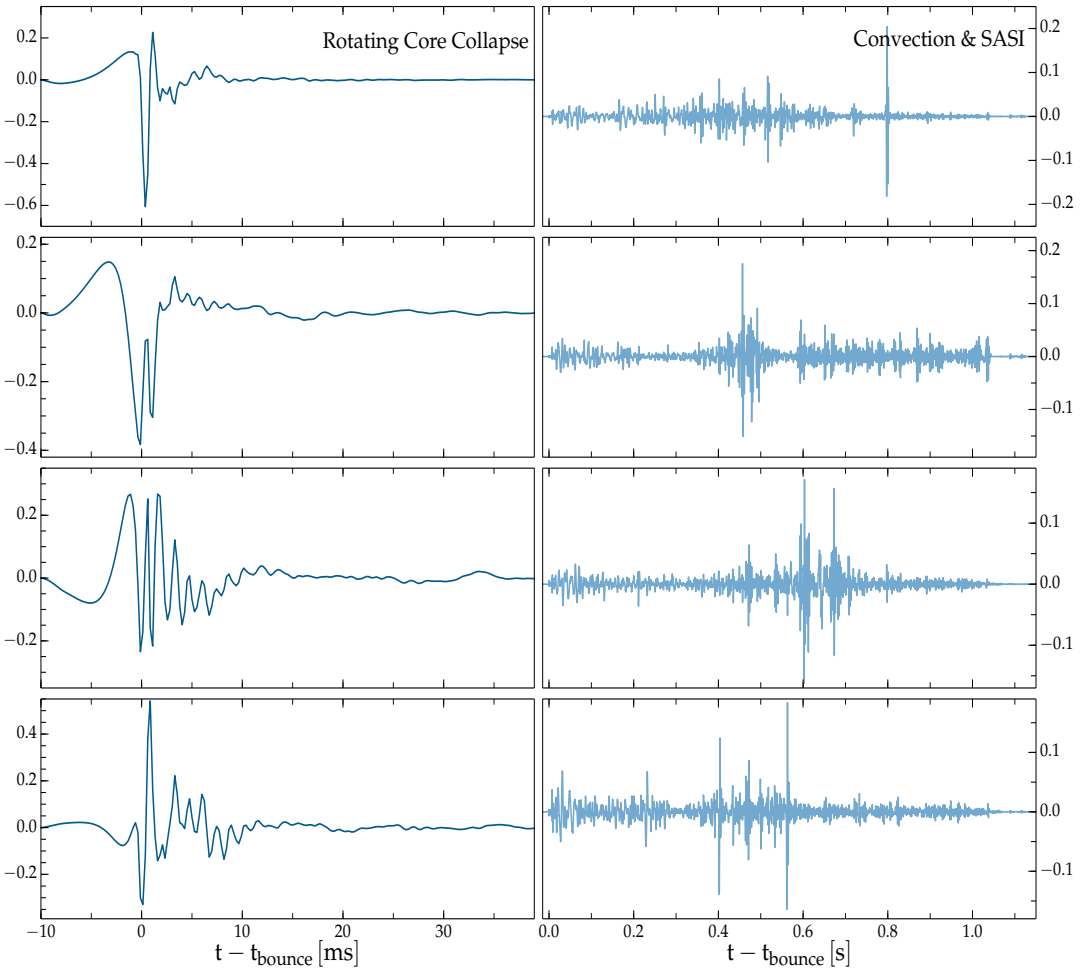

Figure 4.3: (Left) The first four PCs produced from the `RotCC` waveforms. (Right) As for the left, but for the `C&S` waveforms. The first few PCs represent the most common features of the waveforms used in the analysis. A larger number of PCs is needed to represent the broad set of features in waveforms from the `C&S` model. The main feature of the `RotCC` model PCs is the spike at core bounce. Each PC is multiplied during the analysis by an amplitude scale factor. Figure reproduced from [9].

the optimal number of PCs from the behaviour of the signal verses noise log Bayes factor, $\log B_{S,N}$, for both models across the waveform catalogues.

Figures 4.4(a) and 4.4(b) show the signal vs. noise log Bayes factors for five representative waveforms from the `RotCC` and `C&S` models, respectively. The representative waveforms are chosen so that they will span the parameter space of the catalogues. All of the signals are injected with an SNR of 20, as log Bayes factors are proportional to the square of the SNR of the signal. As the number of PCs is increased, the model becomes a better match for the signal in the data, and the Bayes factor is expected to increase sharply. After an ideal number of PCs is reached, no further information about the signal is gained by adding more PCs, and

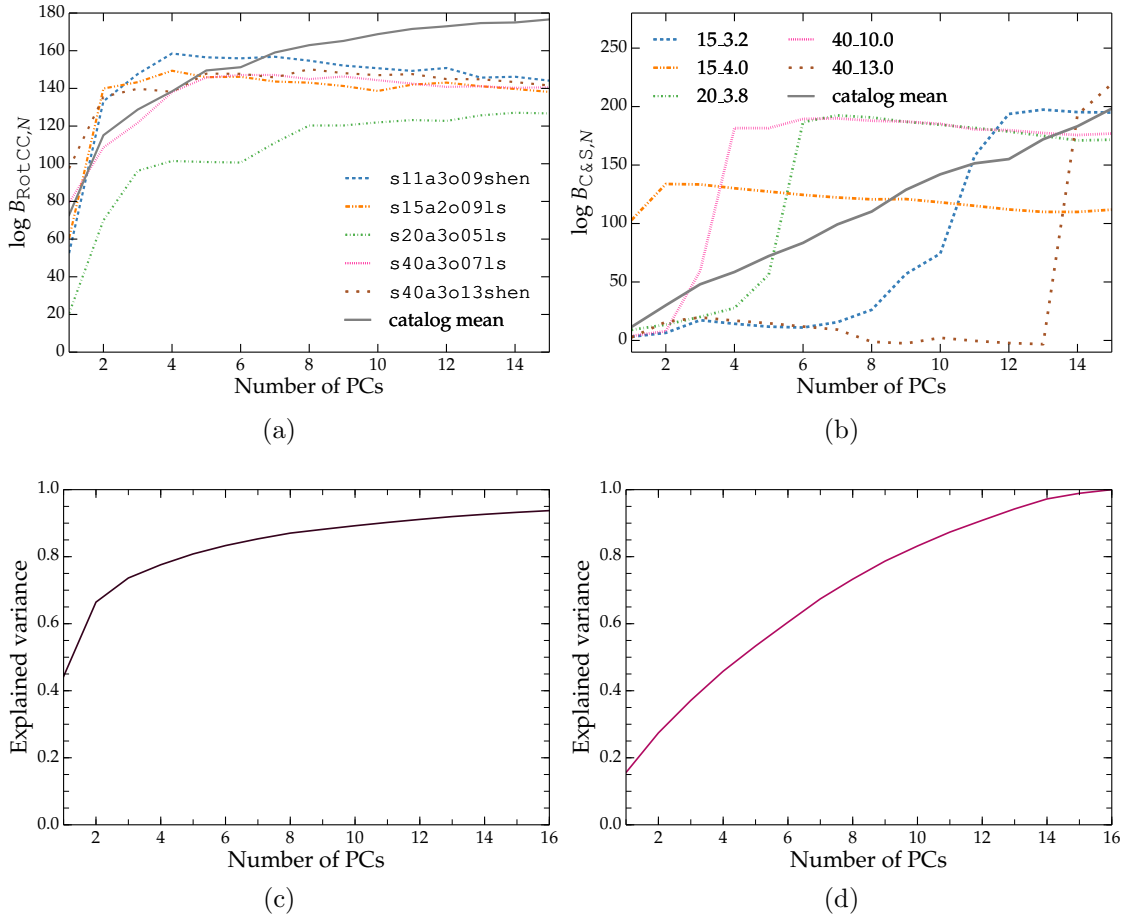

Figure 4.4: The log Bayes factors and explained variance for an increasing number of PCs. (a) The log Bayes factors for an increasing number of PCs, for five waveforms from the `RotCC` model. An ideal number of PCs is reached when the Bayes factors stop increasing. This occurs at similar values for all the `RotCC` waveforms. (b) The same result for five waveforms from the `C&S` model. The results are very different for different waveforms. (c) The variance curve for the `RotCC` model. (d) The variance curve for the `C&S` model. Both methods predict similar numbers for the ideal number of PCs. Figure reproduced from [9].

the Bayes factor stops increasing. If more PCs are added after the ideal number, then the Bayes factor will begin to decrease, due to an Occam factor that occurs as the signal model becomes too complex.

The waveforms in the `RotCC` catalogue have a small variance, therefore, a small number of PCs are needed to represent the entire catalogue. The `C&S` model has greater variance in the catalogue waveforms, and a larger number of PCs are required to accurately represent all the features included in the waveforms. We select 6 PCs for the `RotCC` model, and 9 PCs for the `C&S` model, to maximise the number of features represented in the PCs, whilst minimising the penalty that occurs when one model is significantly more complex than the other.

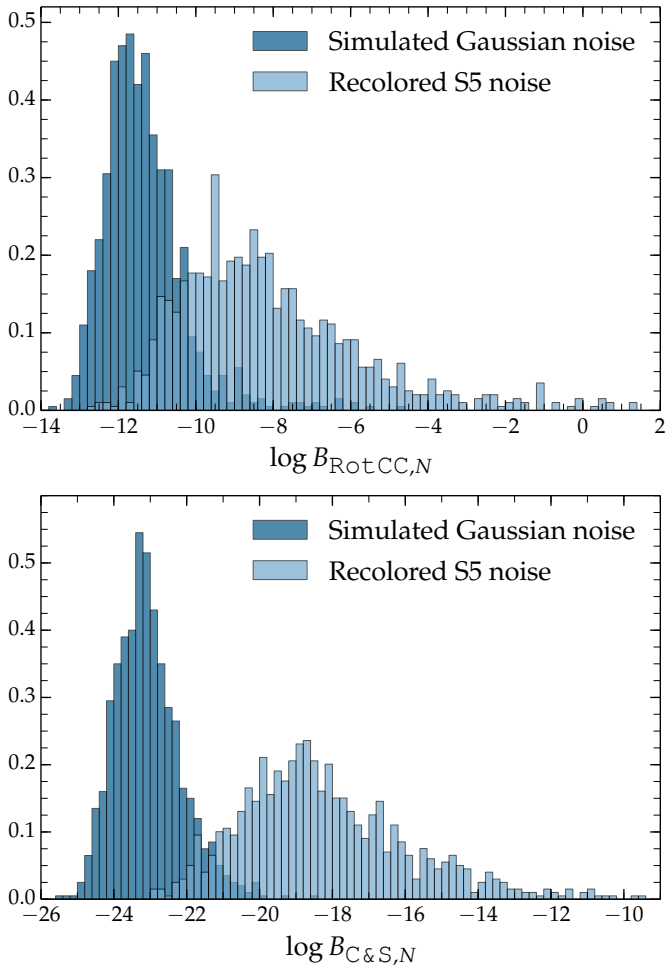

Figure 4.5: The log Bayes factors obtained for 1000 instances of simulated and recoloured aLIGO and AdVirgo design sensitivity noise, for the `RotCC` model using 6 PCs (top), and for the `C&S` model using 9 PCs (bottom). Transient noise artefacts and lines in the real data can increase log $B_{S,N}$ and the width of the noise response. Figure reproduced from [9].

4.6 Signal vs. Noise Models.

The response of SMEE to instances of simulated Gaussian noise was investigated in Logue *et al.* [75], to better understand the results in the presence of real signals. As SMEE is now implemented in C, and the relative complexity of the waveforms is now accounted for in the number of PCs, we recalculate the noise response using 1000 instances of simulated aLIGO and AdVirgo design sensitivity noise, as well as the recoloured noise that we use for a more accurate analysis than previous studies.

In Figure 4.5, the signal vs. noise Bayes factors for 1000 instances of Gaussian and real non-stationary, non-Gaussian noise is shown. The log Bayes factors are obtained by running SMEE on 1000 GPS times, during the 24 hour period of data

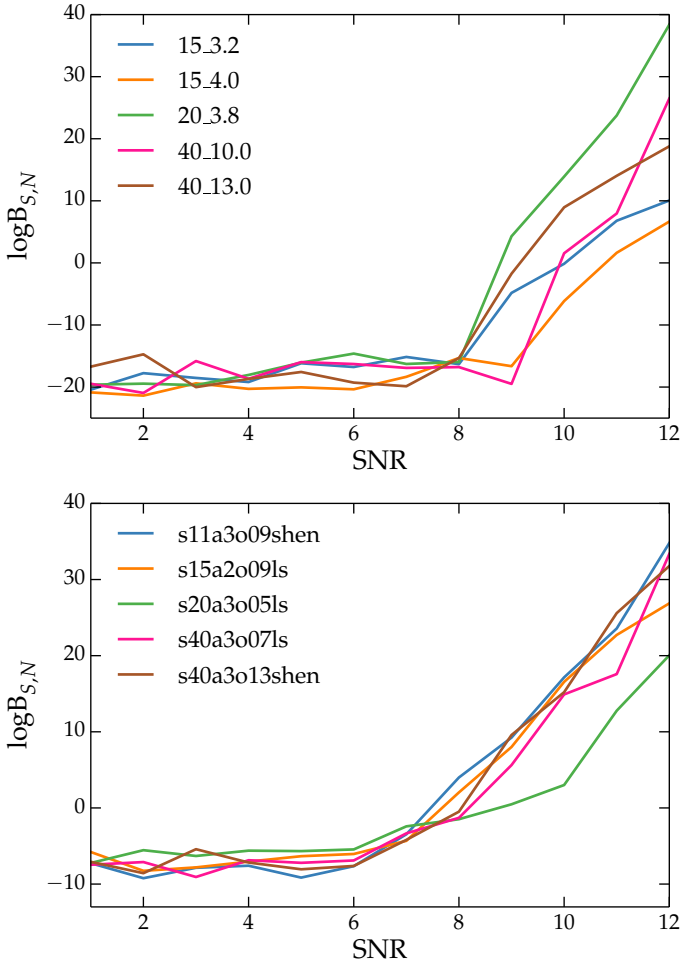

Figure 4.6: The minimum SNR needed for SMEE to detect waveforms from the Dimmelmeier and Murphy catalogues. The top figure shows $\log \mathrm{B}_{S,N}$ as the SNR is increased for five representative waveforms injected from the Murphy waveform catalogue. The bottom figure shows the same results for five representative waveforms from the Dimmelmeier catalogue. For $\log \mathrm{B}_{S,N} \geq 10$, a minimum of SNR 9 is needed for the `RotCC` model, and of SNR 10 for the `C&S` model.

used in this chapter, which contain no GW signals. The mean values are -12 for the `RotCC` model in Gaussian noise, -23 for the `C&S` model in Gaussian noise, -9 for the `RotCC` model in recoloured noise, and -19 for the `C&S` model in the recoloured noise. This is larger than the results found by Logue *et al.* who calculated values of -53.9 for the `RotCC` model and -52.3 for the `C&S` model. This is likely due to differences in normalization between the MATLAB and C implementations of SMEE. Short duration transient noise artefacts and lines in the data increase SMEE's response to noise and increase the standard deviation of the noise response. In Logue *et al.* [75] a threshold value of 5 on $\log \mathrm{B}_{S,N}$ was set using the width of the noise response. We increase the threshold on the value of $\log \mathrm{B}_{S,N}$ to 10 to account for the increased variation in the noise response found in the real, non-Gaussian data.

The minimum signal strength needed for SMEE to be able to detect the signal is investigated, as the explosion mechanism cannot be determined if the CCSN signal cannot be distinguished from detector noise. To determine the minimum SNR that SMEE requires to find a signal, five representative waveforms are chosen from the `RotCC` and `C&S` models. The representative signals are then injected into the recoloured detector noise at increasing SNR values. Logue *et al.* [75] found in their proof-of-principal study that the minimum SNR needed was $\mathrm{SNR} \geq 4 - 5$, however, they add that in a real search for CCSN, in real non-Gaussian noise, that an $\mathrm{SNR} \geq 8$ would be needed for a detection statement.

Figure 4.6 shows how the log Bayes factors change as the SNR increases. For SMEE to distinguish the representative waveforms from noise, a minimum of SNR 9 is needed for the `RotCC` model, and a minimum of SNR 10 is needed for the `C&S` model. The values are consistent with the value needed for a detection statement.

4.7 Determining the Core-Collapse Supernova Explosion Mechanism

To test the ability of SMEE to determine the explosion mechanism, all 128 `RotCC` and 16 `C&S` waveforms are injected at 10 GPS times. The sky position of the Galactic center is used, at distances of 2 kpc, 10 kpc and 20 kpc, to show how well the explosion mechanism can be determined for sources throughout the Galaxy. This gives a total of 1440 injected signals at each distance.

Table. 4.1 contains the antenna pattern averaged signal vs. noise log Bayes factors for five representative waveforms from the `RotCC` and `C&S` models injected in recoloured noise. The table shows the mean log Bayes factor is much larger for waveforms from the `RotCC` catalogue, as they have a larger SNR than the `C&S` waveforms. The log Bayes factor should be larger when using the PCs from the correct explosion mechanism. Waveforms from the `RotCC` model can be distinguished from noise at all of the Galactic distances considered. Waveforms from the `C&S` model can all be distinguished from noise at 2 kpc, and some `C&S` waveforms have enough SNR to be detected at 10 kpc, if they occur when the antenna pattern is most sensitive.

Waveform	$\log \mathrm{B}_{\mathtt{RottCC,N}}$			$\log \mathrm{B}_{\mathtt{C\&S,N}}$		
	2 kpc	10 kpc	20 kpc	2 kpc	10 kpc	20 kpc
`RotCC`						
s11a3o09_shen	24281	927	210	591	7	-8
s15a2o09_ls	27321	1050	241	785	15	-7
s20a3o05_ls	12151	447	92	1223	31	-3
s40a3o07_ls	54281	2121	508	1898	53	0
s40a3o13_shen	64323	2537	618	20510	815	192
`C&S`						
15_3.2	52	-4	-5	328	-6	-12
15_4.0	59	-4	-6	2982	90	5
20_3.8	69	-5	-5	1629	352	-8
40_10.0	20	-5	-6	1687	42	-4
40_13.0	21	-6	-6	24	-11	-12

Table 4.1: The mean signal vs. noise log Bayes factors for five representative waveforms from each mechanism. They are injected at 2 kpc, 10 kpc and 20 kpc at the sky position of the Galactic center. Waveforms from the `RottCC` model can be distinguished from noise throughout the Galaxy. The `C&S` catalogue waveforms are indistinguishable from noise at 20 kpc. Table reproduced from [9].

Figure 4.7 shows $\log \mathrm{B}_{\mathtt{RotCC-C\&S}}$ for all injections at the 3 Galactic distances considered. If the `RotCC` waveforms are identified with the correct explosion mechanism then $\log \mathrm{B}_{\mathtt{RotCC-C\&S}}$ will be positive, and if the `C&S` waveforms are identified with the correct explosion mechanism then $\log \mathrm{B}_{\mathtt{RotCC-C\&S}}$ will be negative. If $\log \mathrm{B}_{\mathtt{RotCC-C\&S}}$ is between -10 and 10, then either the injected waveform could not be distinguished from noise, or it is not possible to distinguish between the explosion mechanisms considered.

The number of detected waveforms from the `C&S` model is 157/160, 150/160 and 19/160, at distances of 2 kpc, 10 kpc and 20 kpc, respectively. The number of detected waveforms from the `RotCC` model is 1279/1280, 1198/1280 and 1019/1280, at distances of 2 kpc, 10 kpc and 20 kpc, respectively. The correct explosion mechanism is determined for all detected waveforms from both models, at all the Galactic distances considered.

All catalogue waveforms are then injected at the sky position of the LMC, at a distance of 50 kpc, at 10 different GPS times. The values of $\log B_{\mathtt{RotCC-C\&S}}$ are shown in Figure 4.7(d). A total of 707/1280 waveforms from the `RotCC` model can be distinguished from noise at this distance, and their explosion mechanism is correctly determined as magnetorotational. None of the waveforms injected from

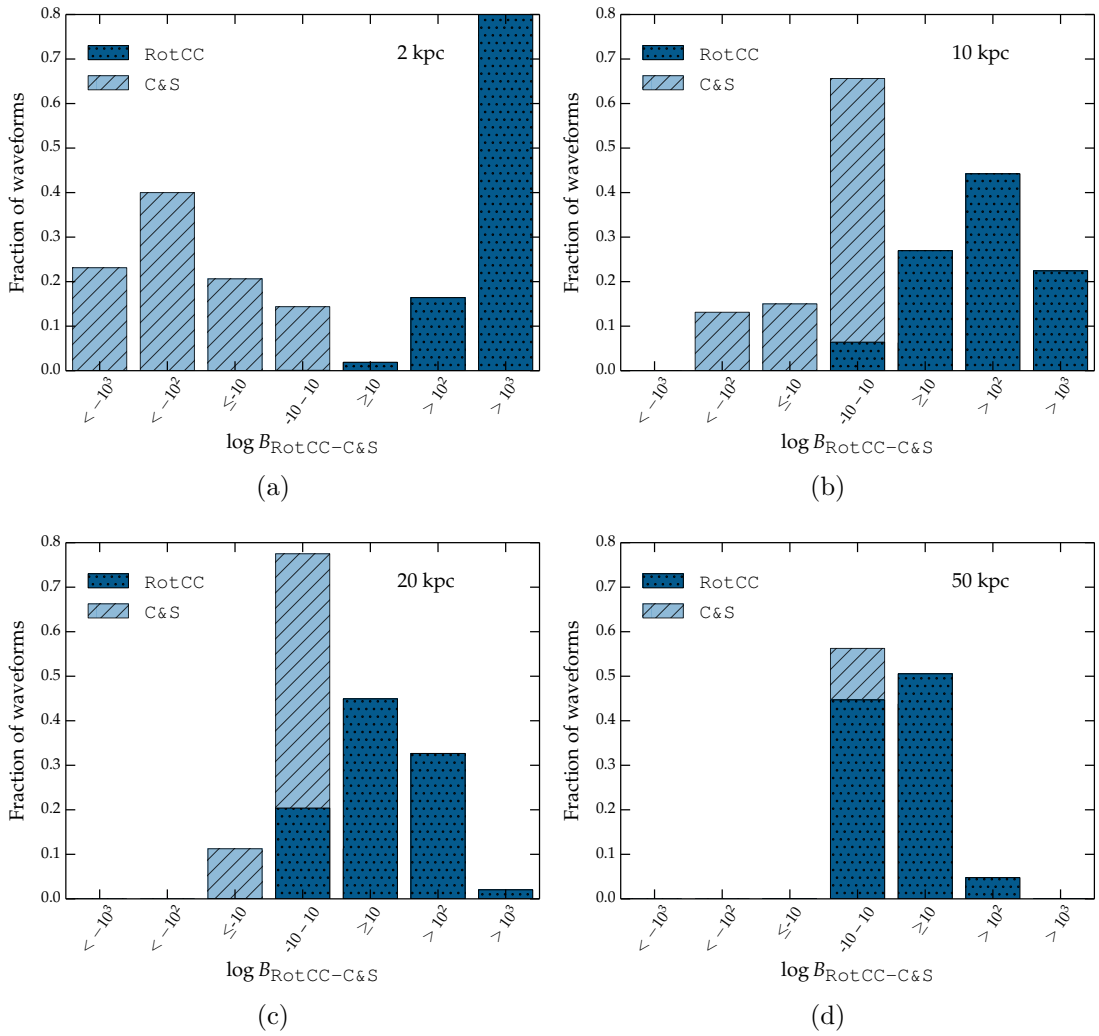

Figure 4.7: The distribution of Bayes factors used to determine the explosion mechanism for Dimmelmeier and Murphy waveforms at different Galactic distances. (a) At 2 kpc the explosion mechanism is correctly determined for all 1437/1440 detected waveforms. (b) At 10 kpc, 1198/1440 waveforms are detected and their explosion mechanism is correctly determined. (c) Almost all `C&S` waveforms have an SNR too small for them to be detected at 20 kpc. (d) Distance of 50 kpc and sky position of the Large Magellanic Cloud. Only rapidly rotating waveforms are detectable at this distance. Figure reproduced from [9].

the `C&S` model can be distinguished from noise at a distance of 50 kpc.

4.8 Testing Robustness

As the waveforms from the `RotCC` and `C&S` models, that were used to create the PCs, may not be an exact match for a real CCSN GW signal, it is important to test the robustness of the method applied in SMEE using waveforms that do not

Waveform	$\log B_{\texttt{RotCC},N}$			$\log B_{\texttt{C\&S},N}$		
	2 kpc	10 kpc	20 kpc	2 kpc	10 kpc	20 kpc
`RotCC`						
`sch1`	15116	567	124	2181	64	3
`sch2`	47185	1843	441	7369	321	69
`abd1`	87453	3454	843	21528	933	235
`abd2`	50420	2000	488	18128	798	183
`abd3`	6426	247	55	5147	185	31
`C&S`						
`yak`	23	-5	-6	141	-10	-11
`müller1`	-5	-5	-5	-9	-12	-11
`müller2`	-5	-6	-5	-8	-10	-12
`müller3`	-5	-5	-6	-9	-11	-11
`ott`	118	-2	-6	24	-12	-12

Table 4.2: The mean signal vs. noise log Bayes factor for five extra waveforms representing each explosion mechanism injected at 2 kpc, 10 kpc and 20 kpc, at the sky position of the Galactic center. The three `müller` waveforms are indistinguishable from noise at 20 kpc . The extra magnetorotational mechanism waveforms can be distinguished from noise throughout our Galaxy. Table reproduced from [9].

come from the catalogues used to construct the PCs. To test robustness, we use five extra waveforms from each mechanism. For the magnetorotational mechanism, the extra waveforms are `sch1`, `sch2`, and the three `abd` waveforms, described in Section 4.2.1. For the neutrino mechanism, the five extra waveforms are the `yak`, `ott` and three `müller` waveforms, described in Section. 4.2.2.

As for the Dimmelmeier and Müller waveforms, the 10 extra waveforms are injected at 10 GPS times, at the sky position of the Galactic center, at distances of 2 kpc, 10 kpc and 20 kpc, leading to a total of 100 injections at each distance. Table. 4.2 shows how well the extra waveforms can be distinguished from noise at the three Galactic distances considered. As for the Dimmelmeier and Müller catalogue waveforms, the table shows the antenna pattern averaged values of the signal vs. noise log Bayes factor. A larger log Bayes factor is expected when the correct signal model is used, and the confidence in the result is larger for larger log Bayes factors. All the extra magnetorotational mechanism waveforms can be distinguished from noise at the 3 Galactic distances considered. The `yak` and `ott` waveforms can be distinguished from noise at 2 kpc. The three `müller` waveforms cannot be distinguished from noise at any of the Galactic distances considered. This is due to the two-dimensional signal models being a bad representation of three-dimensional waveforms.

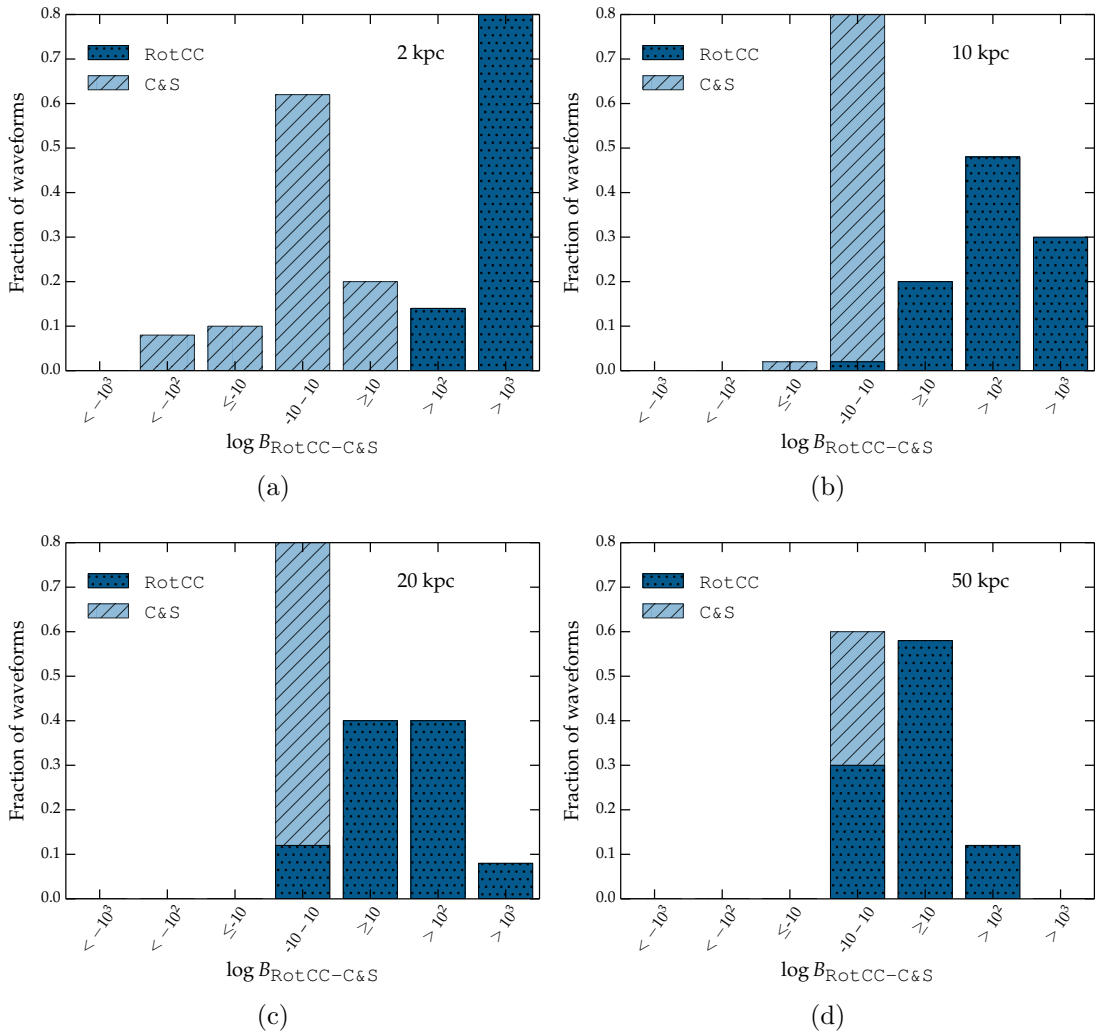

Figure 4.8: The distribution of Bayes factors used to determine the explosion mechanism for extra waveforms representing each mechanism. (a) At 2 kpc, all extra magnetorotational mechanism waveforms can be distinguished from noise, and their explosion mechanism is correctly determined. For the extra neutrino mechanism waveforms, only the explosion mechanism of the `yak` waveform is correctly determined. (b) At 10 kpc, all extra neutrino mechanism waveforms cannot be distinguished from noise. (c) At 20 kpc, 45/100 injected extra magnetorotational waveforms can be distinguished from noise, and their explosion mechanism is correctly determined. (d) The correct explosion mechanism is determined for all extra magnetorotational waveforms distinguishable from noise (27/100) at 50 kpc. Figure reproduced from [9].

Figure 4.8 shows the values of $\log \mathrm{B}_{\texttt{RotCC-C\&S}}$ for all 100 extra waveform injections at distances throughout the Galaxy. As for the waveforms used to calculate the PCs, if the explosion mechanism of the magnetorotational waveforms is correctly determined then $\log \mathrm{B}_{\texttt{RotCC-C\&S}}$ will be positive, and if the explosion mechanism of the neutrino mechanism waveforms is correctly determined then $\log \mathrm{B}_{\texttt{RotCC-C\&S}}$ will be negative. At all distances, the 30 injected `müller` waveforms cannot be distinguished from noise. At 2 kpc, the explosion mechanism of the 10 injected `yak` wave-

forms is correctly determined as neutrino-driven. The explosion mechanism of the 10 `ott` waveform injections are incorrectly determined as magnetorotational. The `Ott` waveforms, shown in the top right panel of Figure 4.2, contain a feature during the first 20 ms that appears reminiscent of the rotational bounce signals. This is due to a strong signal from the early post-bounce phase that arises because of artificially strong prompt convection induced by the neutrino leakage scheme. This feature is likely the cause of the incorrect result. All extra magnetorotational mechanism injections at 2 kpc are distinguished from noise and their explosion mechanism is correctly determined.

At 10 kpc, 1/10 `yak` injections and 49/50 magnetorotational injected waveforms can be distinguished from noise. The explosion mechanism is correctly determined for all detected waveforms. At 20 kpc, 45/50 magnetorotational waveforms, and none of the extra neutrino mechanism waveforms can be distinguished from noise. The explosion mechanism is correctly determined for all detected magnetorotational waveforms at 20 kpc.

Figure 4.8(d) shows the values of $\log \mathrm{B}_{\mathtt{RotCC-C\&S}}$ for the 100 extra waveform injections at 50 kpc and the sky position of the LMC. There are 27/50 magnetorotational waveforms that can be distinguished from noise, and their explosion mechanism is correctly determined as magnetorotational. The minimum SNR needed to detect the extra waveforms is shown in Figure 4.9. The three-dimensional waveforms need a much larger SNR than the two-dimensional waveforms for them to be detected. This shows that updating SMEE to use three-dimensional waveforms will be essential for SMEE to be able to detect lower SNR CCSN signals.

4.9 Summary and Discussion

The Supernova Model Evidence Extractor (SMEE) is designed to measure astrophysical parameters of a CCSN GW detection. CCSNe have long been considered as a potential source for an aLIGO and AdVirgo detector network, and a CCSN detection may provide an ideal probe of the inner regions of the explosion that do not emit electromagnetically. Determining the CCSN explosion mechanism is essential for a full understanding of the physics and processes involved in CCSNe.

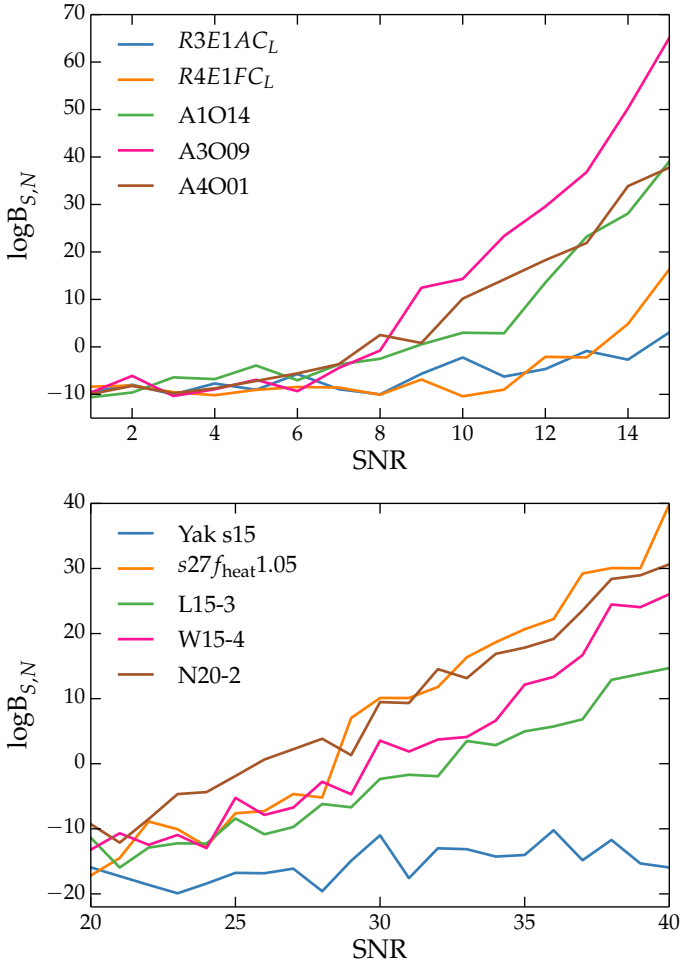

Figure 4.9: The minimum SNR needed for SMEE to detect the extra waveforms used to test robustness. The top figure shows how the signal vs. noise log Bayes factor increases, as the SNR is increased, for five extra representative rapidly-rotating waveforms. The bottom figure shows the same result for five extra representative neutrino-driven convection waveforms. The minimum SNR needed is much larger than for the catalogue waveforms, as two-dimensional signal models are a poor representation of three-dimensional waveforms.

For the first time, we demonstrate the ability of SMEE to determine the CCSN explosion mechanism, with a network of GW detectors, using real non-stationary and non-Gaussian noise. In this chapter, SMEE considers the magnetorotational and neutrino explosion mechanisms, and shows how the correct explosion mechanism can be determined for all detectable catalogue waveforms at distances throughout our Galaxy. GW signals from neutrino-driven convection have a smaller amplitude than those from rapidly-rotating core-collapse. Therefore, detections at distances of 10 kpc or less are needed for a robust result. Furthermore, we can determine the explosion mechanism of rapidly-rotating core-collapse waveforms at the distance and sky position of the LMC.

We further enhance the model selection capabilities of SMEE with a careful selection of the number of PCs, which considers the relative complexity of the different explosion models. A large number of PCs is required to represent all the common features of the neutrino-driven convection waveforms. The number of available waveforms is much smaller than those available for rapidly-rotating core collapse, and the differences between individual waveforms is much larger. This leads to a reduction in the robustness of the result from SMEE, as the parameter space of the neutrino waveforms is not sufficiently covered. Furthermore, three-dimensional neutrino waveforms contain some features that are different from the two-dimensional waveforms used to create the PCs. However, the two-dimensional rapidly-rotating core-collapse waveforms are still a good approximation for three-dimensional rapidly-rotating waveforms, as non-axisymmetric instabilities occur after the signal bounce.

During recent years, two-dimensional neutrino mechanism waveforms with more detailed physics have become available. They include an updated version of the `yak` waveforms used in this study, which are now complete (up to 1s) waveforms, as the 2010 waveforms were truncated at $\sim 500\,\mathrm{ms}$ after bounce [161]. Furthermore, a larger number of three-dimensional neutrino mechanism waveforms have become available recently, including Kuroda *et al.* (2016) [126], who simulate a $15\,\mathrm{M}_{\odot}$ star with three different EOS, showing a strong low-frequency signal from the SASI, and Andresen *et al.* (2016) [153], that include multi-group neutrino transport. Updating SMEE to use the three-dimensional waveforms will be essential for future robust parameter estimation with CCSNe GWs, and is implemented in the next chapter.

Chapter 5

Distinguishing CCSN Signals from other Transient Sources.

During the advanced detector observing runs, SMEE is used as a parameter estimation follow-up tool for any potential GW signal candidates that are identified by the GW searches, or from alerts sent by electromagnetic and neutrino detectors. Due to the low rates for CCSNe within the aLIGO and AdVirgo detection range, it is important to be prepared for a CCSN signal that may occur when the data quality is poor, or when only one detector is operational. To give an accurate result, it is important that SMEE is updated to use the latest available CCSN waveforms. Therefore, in this chapter, SMEE is updated to make signal models from waveforms that were not available when the study in the previous chapter was carried out. The results for running SMEE on real CCSN search triggers from O1 are shown, and what would be expected if a real CCSN signal is present is demonstrated using simulated CCSN signals injected in O1 aLIGO noise.

This chapter is structured as follows: In Section 5.1, we provide an overview of any CCSN waveforms used in this chapter that were not available at the time the study in the previous chapter was carried out. In Section 5.2, we show the new PCs made from the latest available three-dimensional CCSN simulations. In Section 5.3, the output of SMEE using the new signal models is shown when there are no signals or glitches present in the data, and the minimum SNR needed for SMEE to detect CCSN signals with new three-dimensional signal models is determined. In Section 5.4, the explosion mechanism is determined for CCSN signals from the neutrino

and magnetorotational mechanisms using the new signal models. In Section 5.5, a demonstration of how SMEE can be used to determine if a signal is a CCSN or a glitch is given and tested on real CCSN search triggers from O1. In Section 5.6, how well SMEE can reconstruct a CCSN signal is examined, and a demonstration is given of how the reconstructions can be used to determine if the signal is one of the CCSN models considered by SMEE, or a different kind of astrophysical signal. A summary and discussion are given in Section 5.7.

5.1 CCSN Simulations

New three-dimensional neutrino mechanism CCSN waveforms have become available since the study in the previous chapter. Here, a brief description of those waveforms is given, and some example time-series simulations are shown in Figure 5.1.

Andresen *et al.* [153] produce four CCSN GW signals for the first few hundred milliseconds after bounce. They are three-dimensional simulations, with multi-group neutrino transport, and ZAMS masses of $11.2\,\mathrm{M}_\odot$, $20\,\mathrm{M}_\odot$ and $27\,\mathrm{M}_\odot$. There are 3 failed explosions, one at each ZAMS mass, referred to as models s11, s20 and s27, and a successful explosion with a $20\,\mathrm{M}_\odot$ progenitor, referred to as model s20s. The GWs for the $11.2\,\mathrm{M}_\odot$ progenitor are convection-dominated, and the GWs for the higher mass progenitors are SASI-dominated. They find that the SASI-dominated models are clearly distinguishable from the lower mass convection-dominated model by strong low-frequency emission between $100 - 200\,\mathrm{Hz}$. They find that both the convection- and SASI-dominated models show GW emission above 250 Hz, but their GW amplitudes are much lower than previous two-dimensional simulations. Their waveform morphologies are considerably different from the two-dimensional models discussed in the previous chapter. The two $20\,\mathrm{M}_\odot$ progenitor waveforms, scaled for a distance of 10 kpc, are shown in Figure 5.1. The GW amplitude is larger for the exploding model.

Kuroda *et al.* [126] carry out fully relativistic three-dimensional simulations of a $15\,\mathrm{M}_\odot$ progenitor star with three different EOS. The simulations stop at around $\sim 350\,\mathrm{ms}$ after bounce. Figure 5.1(a) shows the waveform simulated with the SFHX EOS, scaled for a distance of 10 kpc, and Figure 5.1(b) shows the waveform simu-

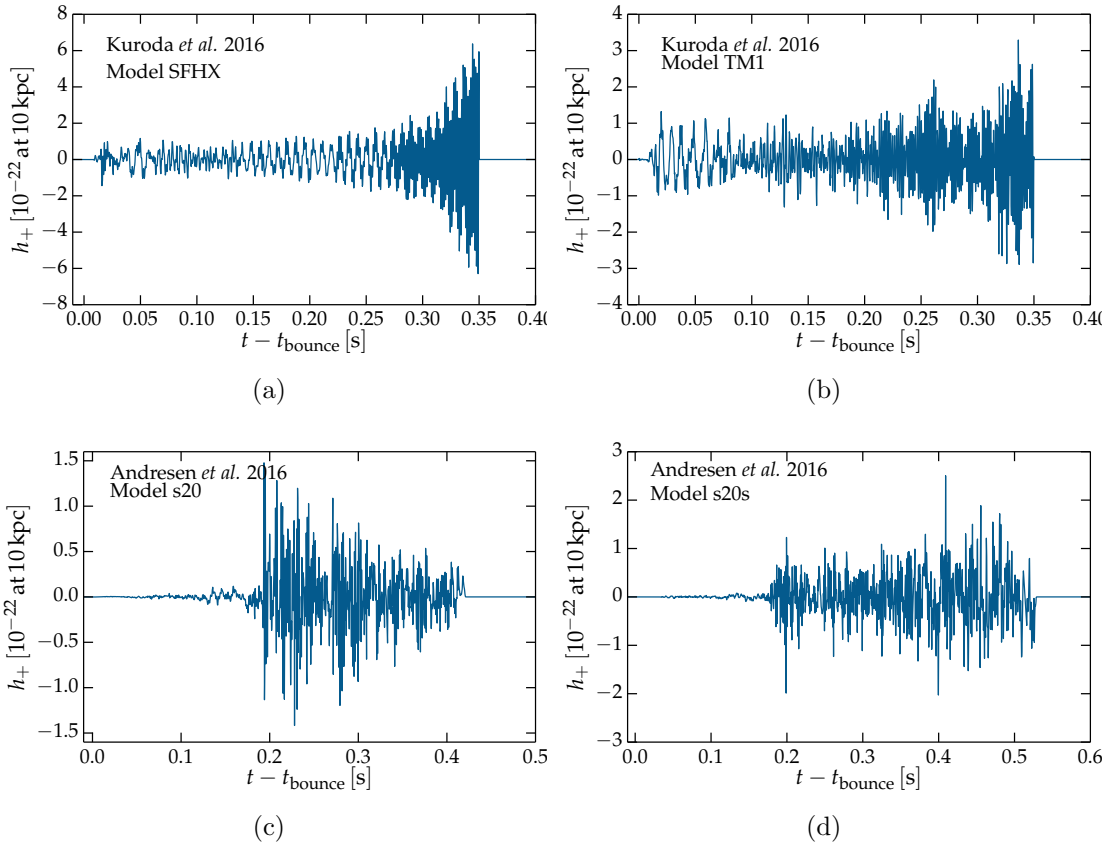

Figure 5.1: The h_+ time series of three-dimensional neutrino mechanism waveforms simulated by Kuroda *et al.* [126] and Andresen *et al.* [153]. (a) GWs from the simulation of a $15\,M_\odot$ progenitor star with the SFHX EOS. (b) GWs from the simulation of a $15\,M_\odot$ progenitor star with the TM1 EOS.(c) A $20\,M_\odot$ progenitor star that does not explode, with strong low-frequency emission between $100 - 200$ Hz. (d) GWs from the simulation of a $20\,M_\odot$ progenitor star that successfully explodes. The amplitude is larger for the successful explosion than for the failed explosion.

lated with the TM1 EOS. They find that the stiffness of the EOS creates significant changes in the SASI, and that the GW frequency increases with time due to accretion on to the proto-neutron star.

5.2 Signal Models

To maximise the probability that SMEE can detect a real CCSN signal, the latest available CCSN waveforms must be used during the analysis of advanced GW detector CCSN detection candidates. For the magnetorotational mechanism, three-dimensional waveforms from the Scheidegger *et al.* [112] waveform catalogue are used, described previously in Section 4.2.1. As Scheidegger *et al.* use a variety of

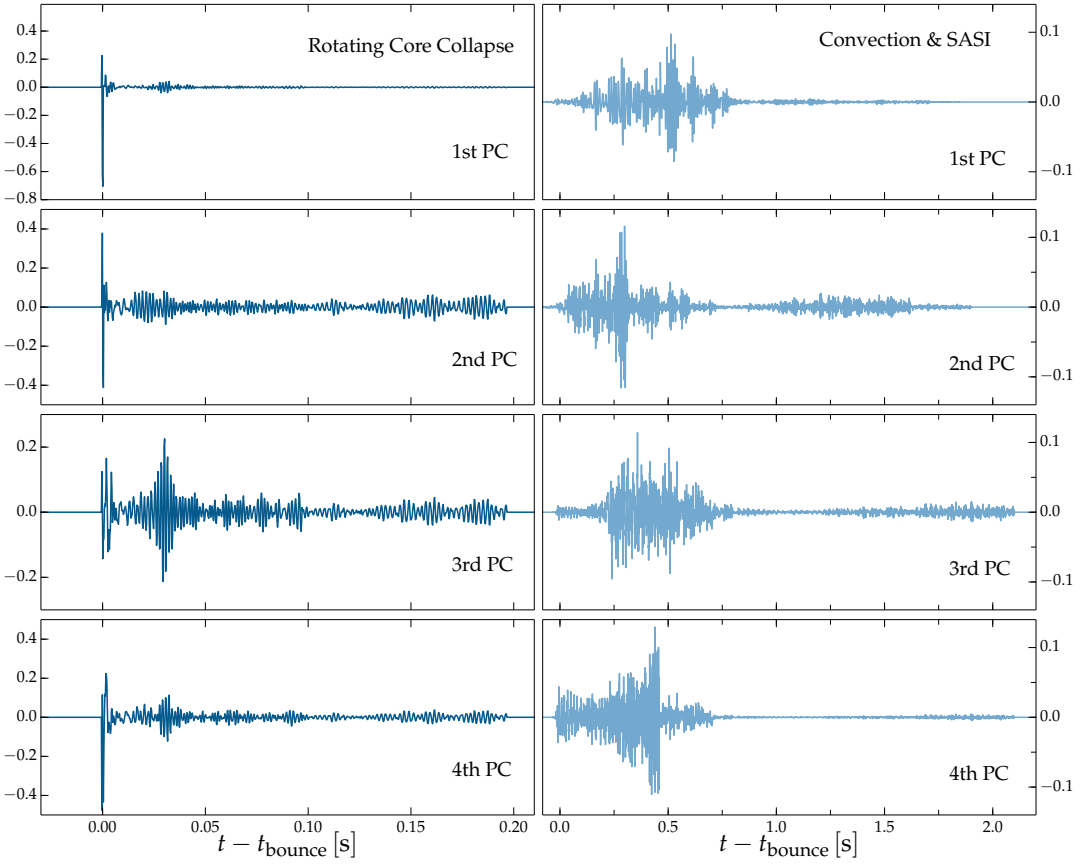

Figure 5.2: The first four three-dimensional PCs used to represent each explosion mechanism. For the magnetorotational signal model, 15 waveforms from Scheidegger *et al.* [112] are used. As for the two-dimensional magnetorotational model, the main feature of the PCs is the spike at core bounce. The neutrino mechanism signal model is made from a mixture of waveforms from Andresen *et al.* [153], Kuroda *et al.* [126] and Müller *et al.* [130]. The PCs are longer in duration than those produced with two-dimensional waveforms.

rotations in their simulations, from non-rotating to extremely rapidly-rotating, we discard the 10 simulations with the slowest rotation values leading to 15 rapidly-rotating waveforms available for use in SMEE. The waveforms from Scheidegger *et al.* are much longer in duration than the two-dimensional waveforms used in the previous chapter, allowing SMEE to reconstruct a longer part of the signal.

For the neutrino mechanism signal model, a combination of three-dimensional waveforms are used from Müller *et al.* [130], Andresen *et al.* [153], and Kuroda *et al.* [126]. There are three waveforms from Müller *et al.* [130], described in Section 4.2.2, with progenitor masses of $15\,\mathrm{M}_\odot$ and $20\,\mathrm{M}_\odot$. There are four waveforms from Andresen *et al.* [153], and two waveforms from Kuroda *et al.* [126], described in the previous section. This gives a total of 9 three-dimensional waveforms used to make the neutrino mechanism signal models.

To make the PCs, using the new three-dimensional waveforms, the same method described in Section 2.2.2 is used. Singular value decomposition is applied to a matrix containing the time-series waveforms to identify the most important features of the different explosion mechanisms. As for the two-dimensional PCs, created from the Dimmelmeier waveforms, the Scheidegger waveforms are aligned at the spike at core bounce before PCA is applied. The three-dimensional neutrino mechanism waveforms are aligned at the onset of emission. Both sets of waveforms are then zero padded to make them the same length. The first four h_+ PCs for each mechanism are shown in Figure 5.2. As for the two-dimensional magnetorotational PCs, the main feature of the three-dimensional magnetorotational PCs is the spike at core bounce. The three-dimensional rapidly rotating PCs are much longer in duration than the two-dimensional rapidly rotating PCs. Most of the GW emission in the neutrino mechanism PCs is contained in the first 1 s.

To determine the ideal number of PCs, the same method described in Section 4.5 is applied to the new three-dimensional PCs. Figure 5.3(a) shows how the log signal vs. noise Bayes factors increase as the number of PCs is increased for the magnetorotational model. As for the Dimmelmeier PCs, five representative waveforms are selected from the Scheidegger *et al.* waveform catalogue that span the full parameter range of the catalogue. Each of the waveforms are injected with a network SNR of 17. All of the signals are detected, even when only 1 PC is used. The signal vs. noise log Bayes factors increase slowly as more PCs are used in the signal model. There is no clear knee in the curves, which makes it difficult to determine from the figure what the ideal number of PCs is. The variance curve for the Scheidegger *et al.* waveforms is shown in Figure 5.3(d). We use 5 PCs for the magnetorotational explosion mechanism, as the variance encompassed in each PC increases more slowly after this number.

Figure 5.3(b) shows how the signal vs. noise log Bayes factors increase as the number of PCs is increased for the neutrino mechanism signal model. As for the Scheidegger waveforms, five representative waveforms that span the parameter space are injected with an SNR of 17. The injected waveforms are Müller *et al.* models W15-4 and N20-2, the 11.2 $M_\odot$ and 20 $M_\odot$ progenitor models from Andresen *et al.*, and the SFHX model from Kuroda *et al.*. The number of PCs needed to represent each waveform has a lot of variety between the different waveforms. The Müller W15-4 model requires two PCs, and the Andresen 11.2 $M_\odot$ progenitor model requires 8 PCs to achieve the optimal log Bayes factor. This means that the differ-

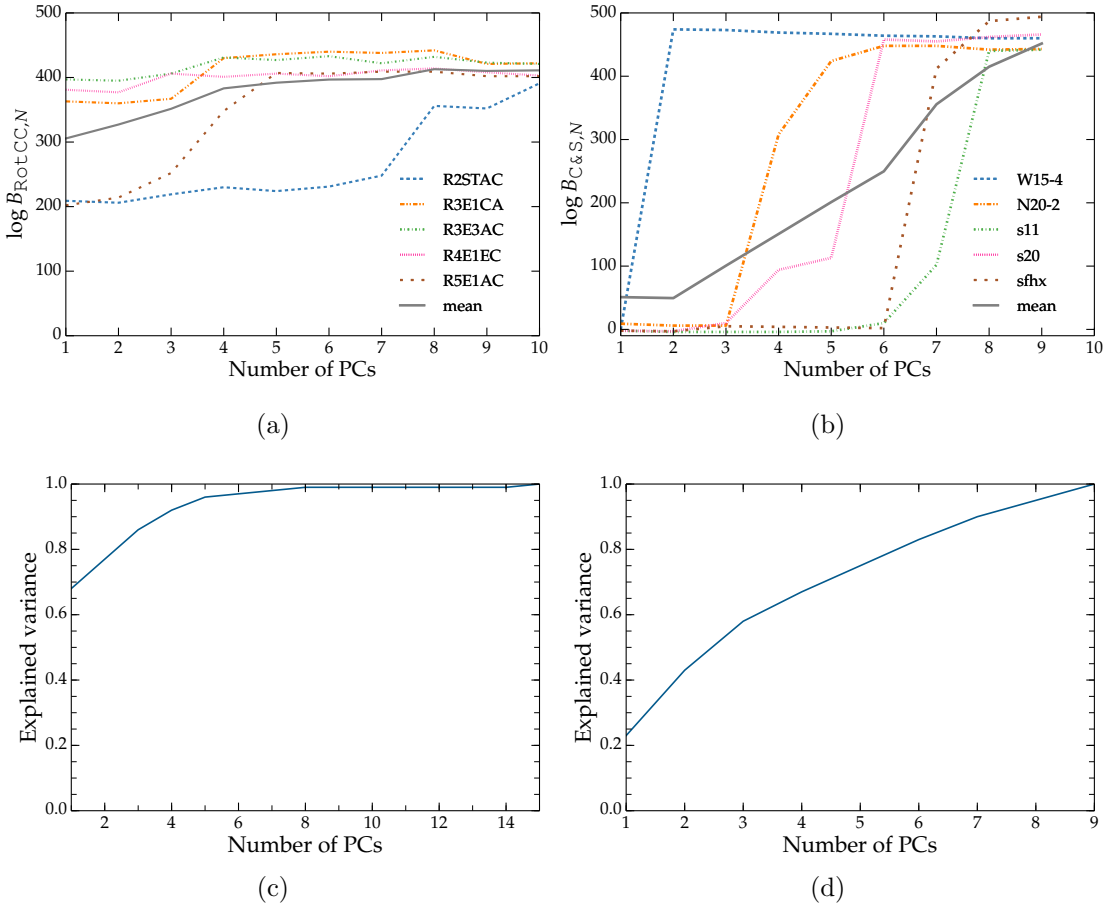

Figure 5.3: The increase in log Bayes factors and cumulative variance as the number of PCs is increased. (a) The signal vs. noise log Bayes factors for an increasing number of PCs, for five representative waveforms from the Scheidegger *et al.* [112] waveform catalogue. An ideal number of PCs is reached when the log Bayes factors are no longer sharply increasing. (b) The same result for five representative three-dimensional neutrino mechanism signals. All signals are injected with an SNR of 17. The results are very different for different waveforms due to their large variance. (c) The variance curve for the Scheidegger waveforms, and (d) is the variance curve for the neutrino mechanism waveforms. Both methods predict similar numbers for the ideal number of PCs.

ent three-dimensional neutrino mechanism waveforms do not share many common features in their time-series morphologies. The variance curve for the neutrino mechanism PCs is shown in Figure 5.3(c). There is no clear change in the variance curve that could indicate the ideal number of PCs. So that all waveforms will be well represented by the neutrino mechanism signal model in SMEE, 8 PCs are used for the three-dimensional neutrino mechanism signal model.

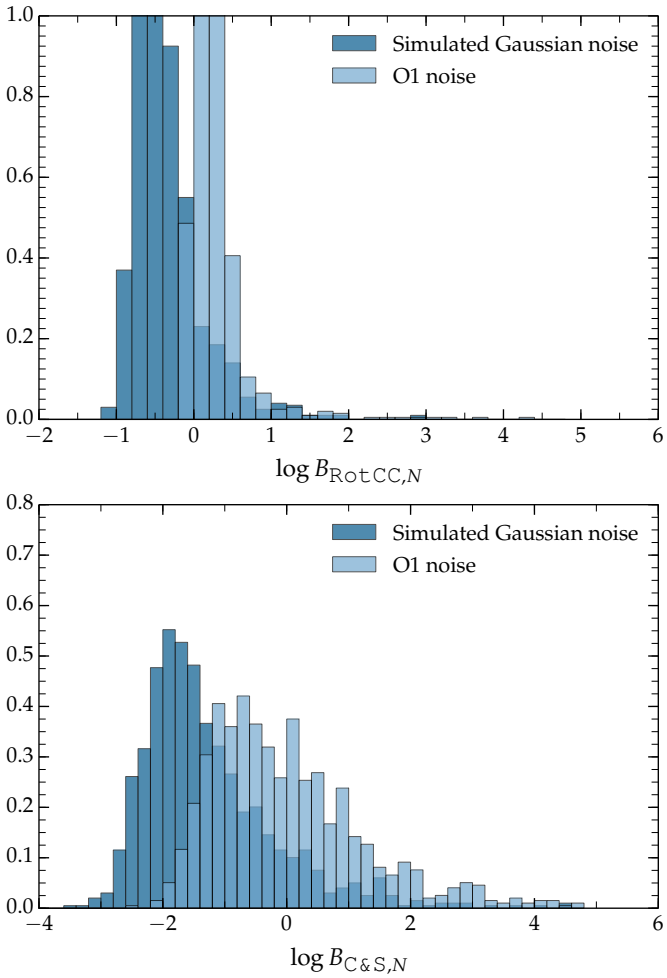

Figure 5.4: The distributions of Bayes factors determined by SMEE for 1000 instances of simulated aLIGO and AdVirgo design sensitivity noise, and 1000 instances of real O1 aLIGO noise. The top figure is the result obtained using the magnetorotational signal model. The bottom figure is the result for the neutrino mechanism model. In Gaussian noise, when no signal is present we expect SMEE to produce a signal vs. noise log Bayes factor of ~ -1 or ~ -2 using the magnetorotational and neutrino signal models, respectively. In O1 noise, when no signal is present we expect SMEE to produce a signal vs. noise log Bayes factor of ~ 0 or ~ -1 using the magnetorotational and neutrino signal models, respectively. The log Bayes factors are higher in real detector noise due to the non-Gaussian, non-stationary noise features.

5.3 Signal vs. Noise Models

As the signal models are now created using three-dimensional CCSN waveforms, the result expected when there is only noise has changed. Therefore, in this section we recalculate the result expected from SMEE when no signals are present in the data. To achieve this, we run SMEE using both signal models on 1000 instances of Gaussian aLIGO design sensitivity noise, and 1000 instances of data taken by aLIGO during O1, as we plan to use O1 data later in this chapter.

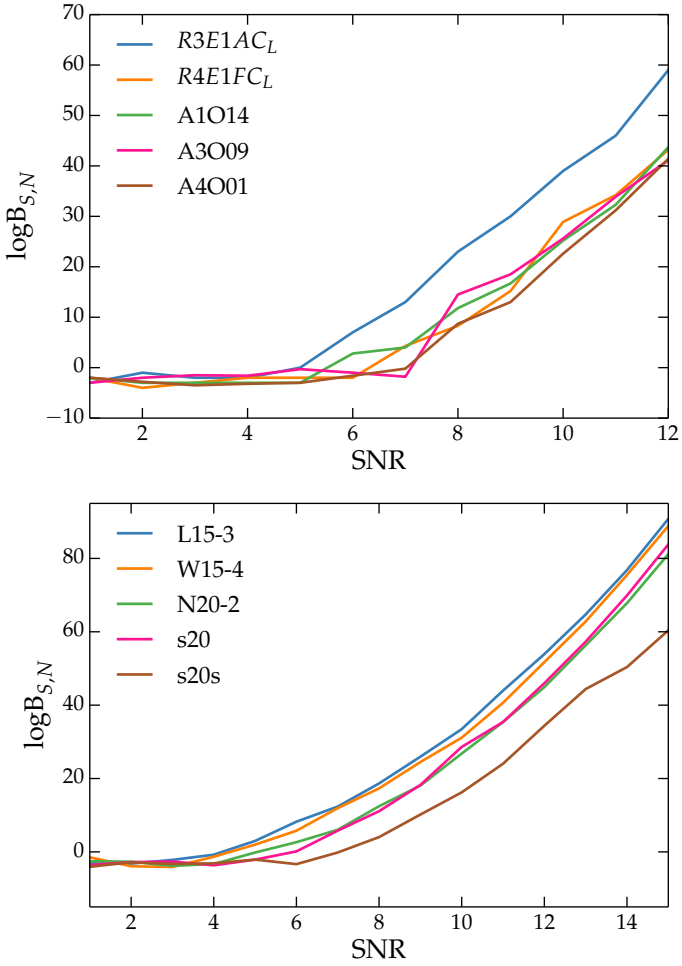

Figure 5.5: The minimum network SNR needed to detect different CCSN signals with signal models produced from three-dimensional CCSN waveforms. Five representative waveforms from each explosion mechanism are injected at increasing network SNR values. The top figure shows the signal vs. noise log Bayes factors obtained using the magnetorotational signal model. The bottom figure shows the signal vs. noise log Bayes factors obtained using the neutrino mechanism signal model. For both the magnetorotational and neutrino mechanism signals, a minimum network SNR of around 8 is needed for SMEE to detect the CCSN waveforms.

The results are shown in Figure 5.4. In Gaussian noise, when no signal is present we expect SMEE to produce a signal vs. noise log Bayes factors of ~ -1 and ~ -2 using the magnetorotational and neutrino signal models, respectively. In O1 noise, when no signal is present we expect SMEE to produce a signal vs. noise log Bayes factor of ~ 0 or ~ -1 using the magnetorotational and neutrino signal models, respectively. The noise only log Bayes factors are smaller when a greater number of PCs are used.

The minimum network SNR needed for SMEE to detect CCSN signals with the new signal models is shown in Figure 5.5. Understanding the minimum network

SNR needed by SMEE is important, as the explosion mechanism cannot be determined for a signal that is not detected. As in the previous chapter, we select 5 representative waveforms from each explosion mechanism. For the magnetorotational explosion mechanism, we select 3 waveforms from the Abdikamalov *et al.* waveform catalogue, used in the previous chapter, and 2 waveforms from the Scheidegger *et al.* waveform catalogue. For the neutrino explosion mechanism, we select the 3 waveforms from Müller *et al.*, and the $20\,M_{\odot}$ progenitor waveforms from Andresen *et al.*. All of the waveforms are injected into aLIGO and AdVirgo noise recoloured to design sensitivity at the same GPS time and sky position. The distance of each signal is then changed to increase the network SNR values.

A signal is considered as being detected by SMEE if the signal verses noise log Bayes factor is larger than 10. The minimum network SNR needed for SMEE to detect the magnetorotational representative signals with the magnetorotational signal model is network SNR 8. For the Abdikamalov waveforms, the minimum network SNR is similar to that obtained using the two-dimensional signal models in the last chapter. For the Scheidegger waveforms, the minimum network SNR needed to detect them is much smaller using the three-dimensional signal model than the previous result of network SNR 12 obtained with the two-dimensional signal model in the last chapter. The minimum network SNR needed for SMEE to detect the neutrino mechanism representative signals with the neutrino mechanism signal model is network SNR 8. This is much smaller than the minimum network SNR of 30 needed when using the two-dimensional signal models in the last chapter. Updating SMEE to three-dimensional signal models has increased the sensitivity of SMEE for all types of currently available CCSN waveforms.

To test the robustness of the result, three-dimensional waveforms that were not included in the PCs are used. As there are currently no more available three-dimensional waveforms that can be used for this test, the PCs are made again leaving out one of the signals from each of the explosion mechanisms. The left out waveform for the magnetorotational signal model is Scheidegger model $R3E1AC_L$. The left out waveform for the neutrino mechanism model is the Müller waveform L15-3. 7 PCs are then used for each signal model. The two left out signals are injected in recoloured noise, and the distance of each signal is then changed to increase the network SNR values. The results are shown in Figure 5.6. A network SNR of 15 is needed to detect the $R3E1AC_L$ waveform, and a network SNR of 20 is needed to detect the L15-3 waveform. For the magnetorotational signal model, this a only

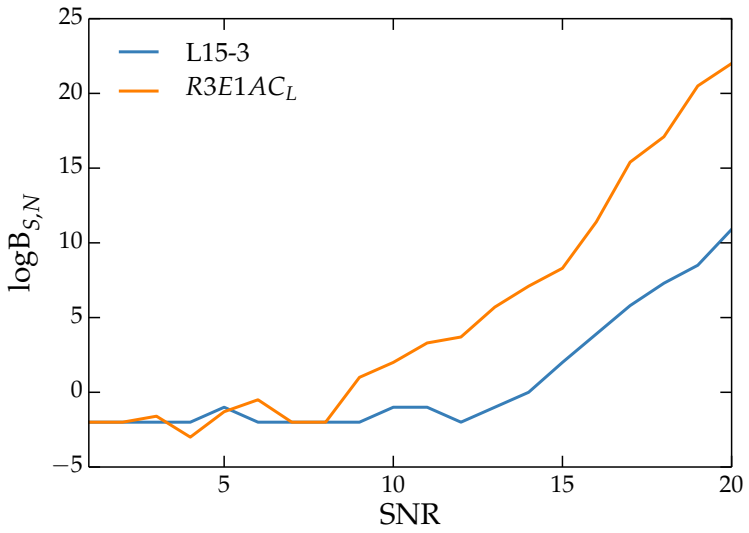

Figure 5.6: Testing the robustness of the minimum network SNR needed to detect different CCSN signals with signal models produced from three-dimensional CCSN waveforms. Two representative waveforms from each explosion mechanism that are not included in the waveforms used to make the signal model are injected at increasing network SNR values. A network SNR of 15 is needed to detect the $R3E1AC_L$ waveform, and a network SNR of 20 is needed to detect the L15-3 waveform. This is a big improvement from the results using two-dimensional waveforms.

a small improvement of the result obtained using the signal model produced from the two-dimensional waveforms. The L15-3 waveform shows a larger improvement, as the minimum network SNR needed for the L15-3 waveform is now SNR 20 and was SNR 37 in the previous chapter.

5.4 Determining the Core-Collapse Supernova Explosion Mechanism

In this section, how well SMEE can determine the explosion mechanism is examined using the new signal models made from the three-dimensional CCSN waveforms. To test the ability of SMEE to determine the explosion mechanism, all of the three-dimensional CCSN waveforms that were used when making the PCs are injected into recoloured noise. This is a total of 15 rapidly-rotating CCSN waveforms from Scheidegger *et al*, and 9 neutrino mechanism waveforms from Müller *et al.*, Kuroda *et al.* and Andresen *et al.*.

As in Section 4.7, all waveforms are injected at 10 GPS times to represent

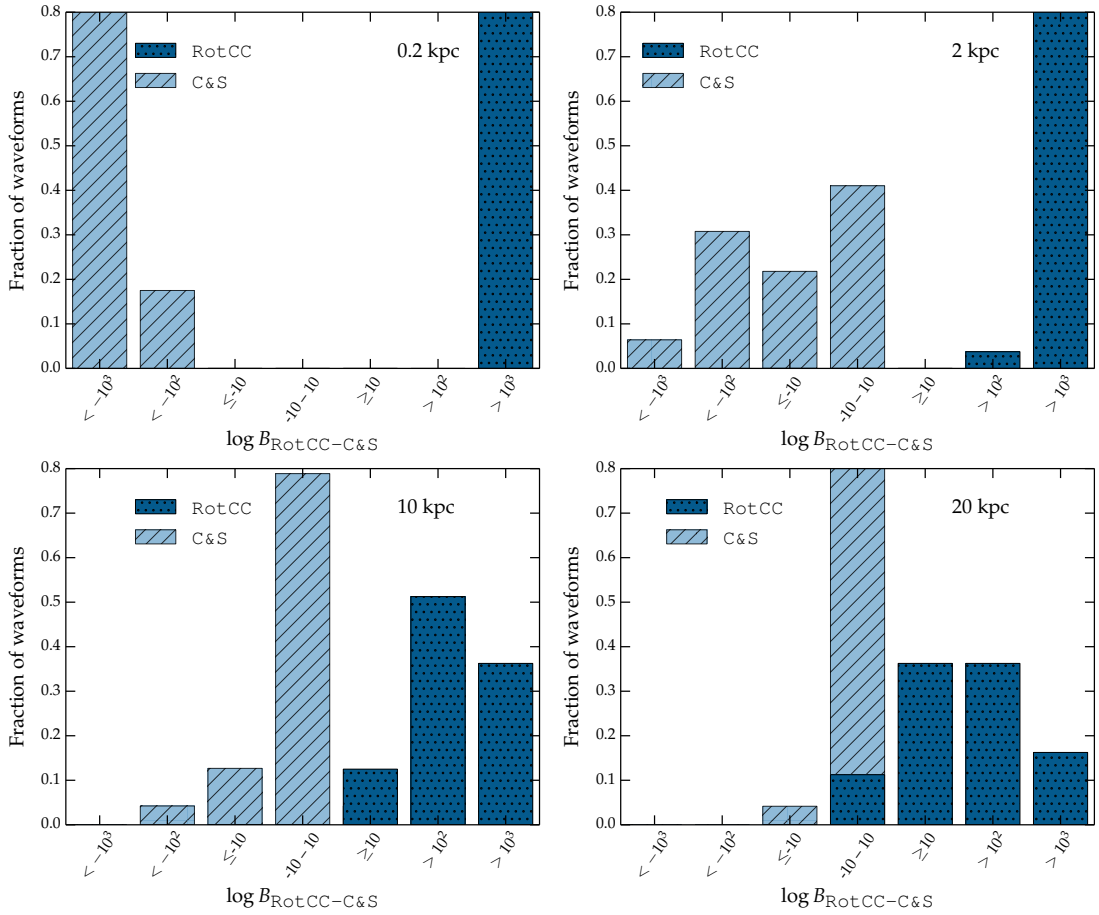

Figure 5.7: The distribution of Bayes factors used to determine the explosion mechanism using three-dimensional signal models for waveforms injected from different explosion mechanisms in recoloured aLIGO and AdVirgo design sensitivity noise. (a) At 0.2 kpc all signals are detected and their explosion mechanism is correctly determined. (b) At 2 kpc some of the neutrino mechanism waveforms can no longer be detected. (c) At 10 kpc the explosion mechanism is correctly determined for all detected waveforms. (d) At 20 kpc almost no neutrino mechanism waveforms can be detected and the correct explosion mechanism is determined for all other waveforms.

different antenna pattern sensitivities over a 24 hour period. As some of the three-dimensional neutrino mechanism waveforms have a smaller amplitude than the two-dimensional waveforms used in Section 4.7, we inject the signals in the direction of the Galactic center at three of the distances used previously (2 kpc, 10 kpc and 20 kpc), and an extra smaller distance of 0.2 kpc. We use the same recoloured aLIGO and AdVirgo noise described in Section 4.7.

Figure 5.7 shows the values of $\log B_{\mathtt{RotCC-C\&S}}$ for all injections, at the 4 Galactic distances considered. If the magnetorotational waveforms are identified with the correct explosion mechanism then $\log B_{\mathtt{RotCC-C\&S}}$ will be positive, and if the neutrino mechanism waveforms are identified with the correct explosion mechanism then $\log B_{\mathtt{RotCC-C\&S}}$ will be negative. If $\log B_{\mathtt{RotCC-C\&S}}$ is between -10 and 10 then either

the injected waveform could not be distinguished from noise, or it is not possible to distinguish between the explosion mechanisms considered.

The number of detected Scheidegger waveforms was 150/150, 150/150, 150/150 and 140/150 at distances of 0.2 kpc, 2 kpc, 10 kpc and 20 kpc, respectively. The number of detected three-dimensional neutrino mechanism waveforms was 90/90, 53/90, 16/90 and 7/90 at distances of 0.2 kpc, 2 kpc, 10 kpc and 20 kpc, respectively. The explosion mechanism was correctly determined for all detected waveforms at all Galactic distances considered. Updating the signal models to use three-dimensional waveforms has resulted in a large improvement from the results in Section 4.8, in which none of the three-dimensional Müller waveforms were detected with the two-dimensional signal models at any of the distances considered.

5.5 Core-collapse Supernova Signal or Glitch?

In this section, the ability of SMEE to distinguish between CCSN signals, glitches and other astrophysical transient sources is determined. Data taken during O1 is used, as the detectors have undergone many changes since the initial detectors S5 science run, and the types of glitches found in the data have changed enough that using glitches in recoloured S5 noise would not be an accurate representation of the glitches that are expected in future advanced detector observing runs.

Four different types of transients are analysed by SMEE in this section. The first is 1000 injections of the Scheidegger *et al.* waveform model $R3E1AC_L$ (see Section 4.2.1). The second is 1000 injections of the Müller *et al.* waveform model L15-3, (see Section 4.2.2). The third is 250 sine Gaussian waveforms, with a frequency of 250 Hz and a duration of 20 ms. The fourth are glitches that are coincident in time between the two aLIGO detectors. The 250 loudest background events found by cWB in the O1 targeted CCSN search are used. The SNR values of the Scheidegger and Müller injections are shown in Figure 5.8. The SNR varies due to the antenna pattern and the quality of the data. We only use triggers that are found after data quality vetoes have been applied. The Scheidegger waveforms are injected at a distance of 2 kpc, and the Müller waveforms are injected at 0.2 kpc, as their GW emission has a smaller amplitude, and the SNR needs to be large enough for the injections to be detected by SMEE.

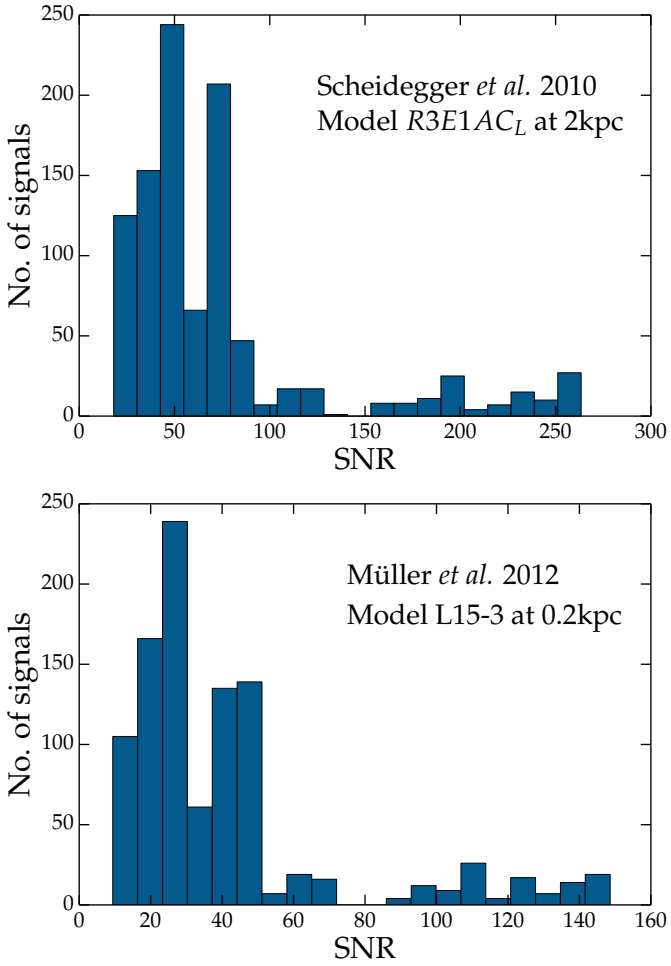

Figure 5.8: The network signal to noise ratio of 1000 Scheidegger waveforms injected at 2 kpc (top), and 1000 Müller waveforms injected at 0.2 kpc (bottom), in O1 aLIGO noise. The Müller waveforms have an order of magnitude smaller amplitude than the Scheidegger waveforms. The SNR depends on the antenna pattern at the time of the injection and the quality of the data.

A test that can be performed to determine if the signal is a real astrophysical signal or a glitch is the Bayesian coherence test [73]. To perform the coherence test, we calculate a coherent vs. incoherent signal or noise Bayes factor $B_{C,IN}$. First, the evidence must be calculated coherently, as for the previous evidences calculated by SMEE. The coherent evidence Z_c, with combined data d from all detectors, which contains a coherent signal S_c with parameters θ, is given by,

$$Z_c = \int_\theta p(\theta|S_c)p(d|\theta, S_c)d\theta\,. \tag{5.1}$$

For an incoherent signal, each of the N detectors contains a signal which can be described by different parameters for each detector. The incoherent evidence Z_i is

then given by,

$$Z_i = \prod_{j=1}^{N} \int_{\theta} p(\theta_j|S_j)p(d_j|\theta_j, S_j)d_j\theta \,. \tag{5.2}$$

The coherent vs. incoherent Bayes factor $B_{C,I}$ can then be calculated as,

$$B_{C,I} = Z_c/Z_i \,. \tag{5.3}$$

It is possible to calculate a coherent vs. incoherent or noise Bayes factor $B_{C,IN}$. The incoherent or noise evidence Z_{in} is then given by,

$$Z_{in} = Z_s^1 Z_s^2 + Z_s^1 Z_n^2 + Z_n^1 Z_s^2 + Z_n^1 Z_n^2 \,, \tag{5.4}$$

where Z_s^1 is the signal evidence for detector 1, Z_n^1 is the noise evidence for detector 1, Z_s^2 is the signal evidence for detector 2, and Z_n^2 is the noise evidence for detector 2. The coherent vs. incoherent or noise Bayes factor $B_{C,IN}$ is then given by,

$$B_{C,IN} = Z_c/Z_{in} \,. \tag{5.5}$$

The log Bayes factors for the Müller and Scheidegger injections are shown in Figure 5.9. Figure 5.9(a) shows the signal vs. noise log Bayes factors for the 1000 Müller injections using the neutrino mechanism signal model. If the signal model is a correct match for the signal in the data, then log $B_{S,N}$ should be proportional to the SNR squared. The same result for the Scheidegger injections and magnetorotational signal model is shown in Figure 5.9(b). A small number of signals have a log $B_{S,N}$ value larger than expected. This can occur if there is glitch near to the CCSN signal in one or more detector. The log $B_{\texttt{RottCC-C\&S}}$ values are shown in Figure 5.10. SMEE correctly determines the explosion mechanism for all of the 2000 CCSN signals injected in O1 data.

Figure 5.9(c) shows the coherent vs. incoherent or noise log Bayes factors for the 1000 Müller injections using the neutrino mechanism signal model. If the signal is a CCSN, then it is expected that log $B_{C,IN}$ should be larger than zero. The values of log $B_{C,IN}$ for the Scheidegger injections are shown in Figure 5.9(d). Using both signal models, some of the injected CCSN signals have log $B_{C,IN}$ values between 0 and -10. This is because log $B_{C,IN}$ can be negative when the signal is a CCSN, if the SNR is less than 8 in one or more of the detectors considered. To rule out a CCSN signal candidate as being a glitch, log $B_{C,IN}$ would need to be smaller than

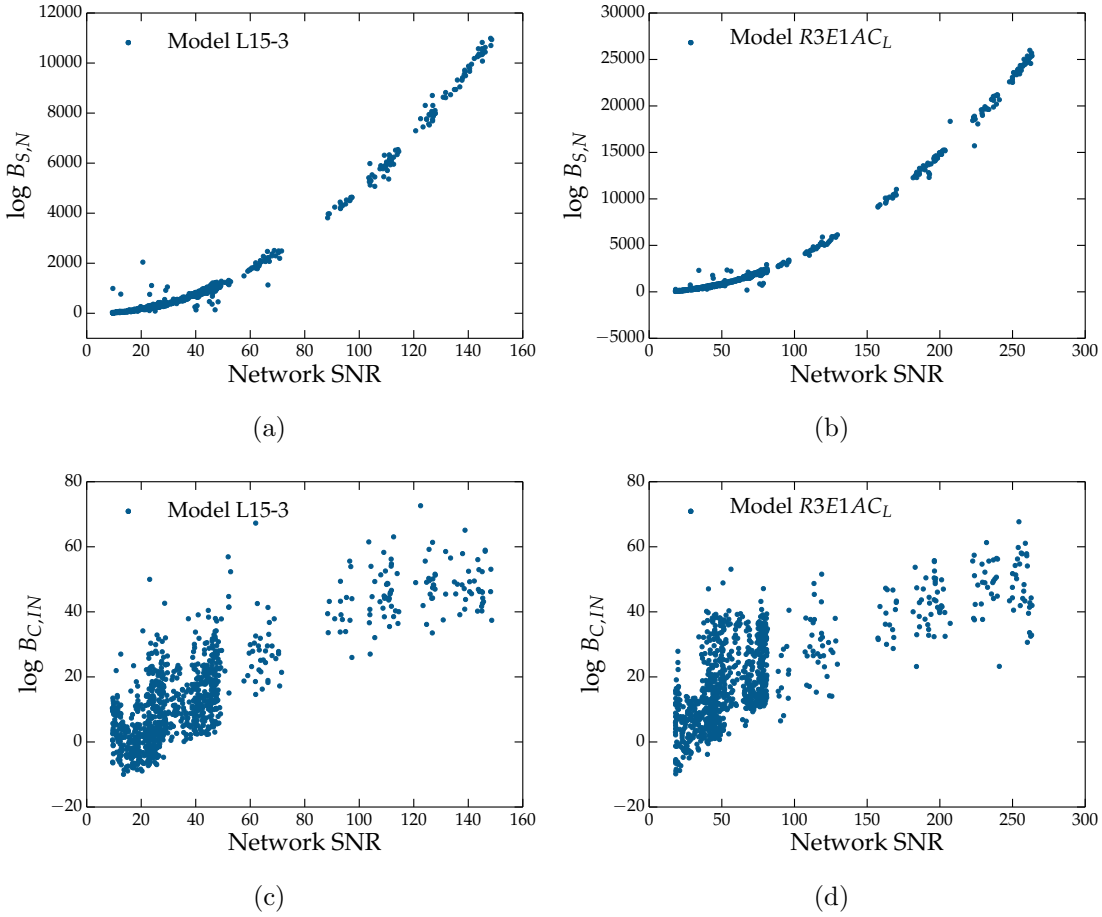

Figure 5.9: The log Bayes factors obtained for 1000 Müller and Scheidegger waveforms injected in O1 noise. (a) The signal vs. noise log Bayes factors obtained for 1000 Müller injections using the neutrino mechanism signal model. (b) The signal vs. noise log Bayes factors obtained for 1000 Scheidegger injections using the magnetorotational signal model. (c) The coherent vs. incoherent or noise log Bayes factors obtained for the Müller injections using the neutrino mechanism signal model. (d) The coherent vs. incoherent or noise log Bayes factors obtained for the Scheidegger injections using the magnetorotational signal model.

-10.

To determine if a signal candidate is a CCSN or a glitch it is possible to calculate both types of log Bayes factors, and compare the results to those expected from Figure 5.9. To determine if SMEE can reject glitches, 250 background triggers from the cWB O1 targeted CCSN search are used. To calculate the background, data from one detector is slid in time by a duration longer than the light travel time between detectors, so that all coincident triggers cannot possibly be real GWs. As we are certain that all the background triggers are glitches, they can be used to determine the output of SMEE when search triggers come from coincident glitches.

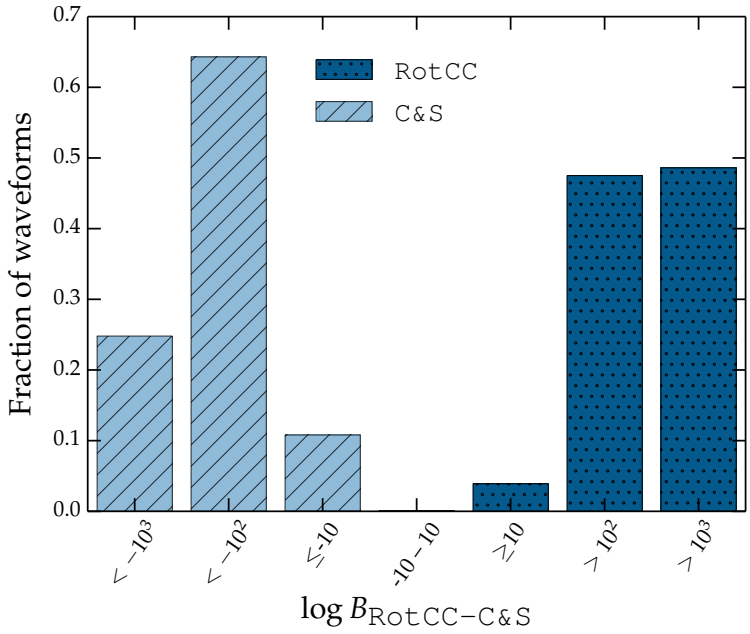

Figure 5.10: The distribution of Bayes factors used to determine the explosion mechanism for 1000 Scheidegger and 1000 Müller waveforms injected in O1 aLIGO data. The Scheidegger waveforms are injected at 2 kpc, and the Müller waveforms are injected at 0.2 kpc. If the explosion mechanism of the rapidly-rotating Scheidegger waveforms has been correctly determined then log $B_{\texttt{RotCC-C\&S}}$ will be positive, and if the explosion mechanism of the neutrino mechanism Müller waveforms is correctly determined then log $B_{\texttt{RotCC-C\&S}}$ will be negative. All waveforms are identified with the correct explosion mechanism.

The log Bayes factors obtained by SMEE for the 250 coincident glitches are shown in Figure 5.11. The signal vs. noise log Bayes factors obtained using the neutrino mechanism signal model are shown in Figure 5.11(a), and for the magnetorotational signal model in Figure 5.11(b). For the neutrino and magnetorotational mechanism signal models, there are 13 and 2 of the glitches, respectively, which have a log$B_{S,N}$ value large enough for them to be considered as possible signal candidates. The log$B_{S,N}$ values are clearly not proportional to the square of the SNR as would be expected if they were CCSN signals. The coherent vs. incoherent or noise log Bayes factors obtained using the neutrino mechanism signal model are shown in Figure 5.11(c), and the coherent vs. incoherent or noise log Bayes factors obtained using the magnetorotational signal model are shown in Figure 5.11(d). All of the log$B_{C,IN}$ values for the glitches with a large log$B_{S,N}$ value, for both signal models, are smaller than expected if the candidate is a real CCSN signal. Therefore, SMEE determines that all of the 250 cWB glitches are consistent with either noise or a glitch, and are not consistent with a CCSN signal.

The log Bayes factors determined by SMEE for the 250 sine Gaussian signals are shown in Figure 5.12. The signal vs. noise log Bayes factors obtained using the

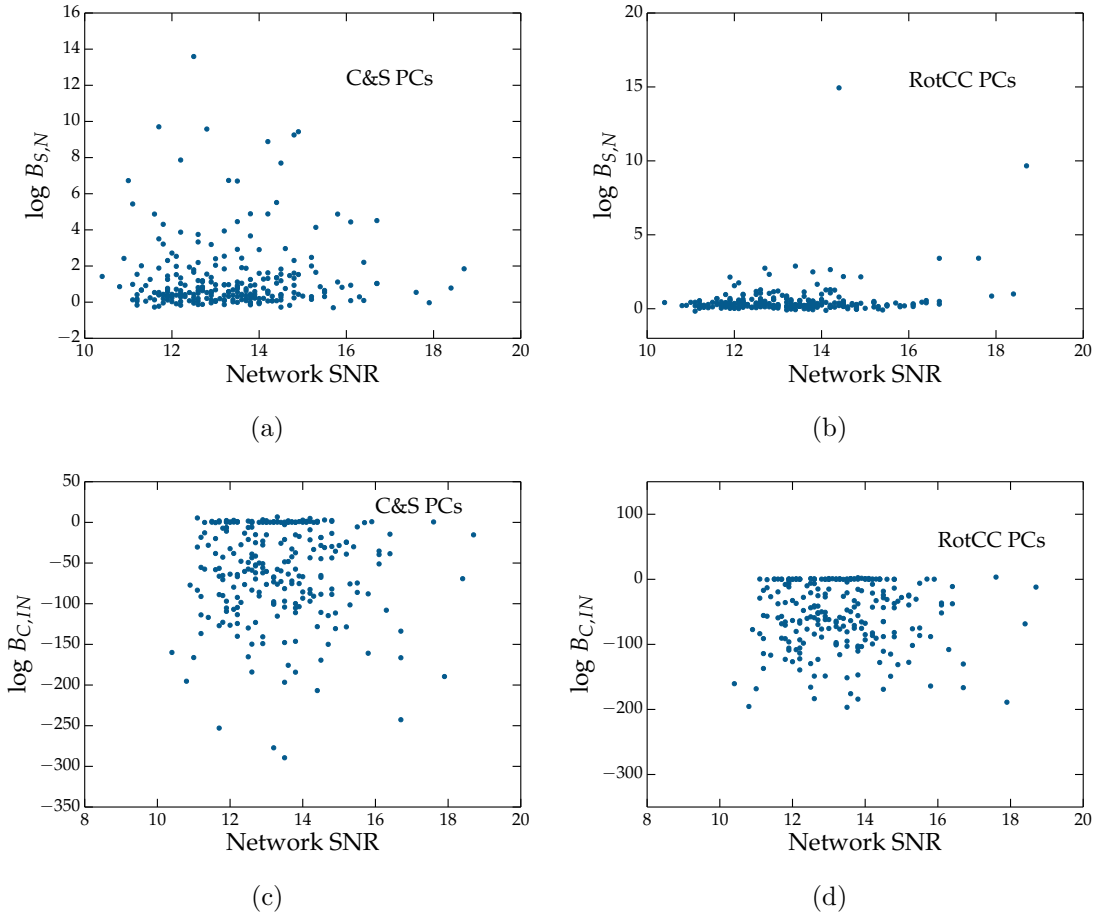

Figure 5.11: The log Bayes factors obtained for 250 cWB background triggers found during the O1 targeted CCSN search. (a) The signal vs. noise log Bayes factors obtained using the neutrino mechanism signal model. (b) The signal vs. noise log Bayes factors obtained using the magnetorotational signal model. (c) The coherent vs. incoherent or noise log Bayes factors obtained using the neutrino mechanism signal model. (d) The coherent vs. incoherent or noise log Bayes factors obtained using the magnetorotational signal model. None of the glitches are considered as potential CCSN candidates.

neutrino mechanism signal model are shown in Figure 5.12(a), and for the magnetorotational signal model in Figure 5.12(b). When using the neutrino mechanism signal model, there are 42 sine Gaussian injections which have a large enough value of log$B_{S,N}$ for them to be considered as possible signal candidates. These signals mainly have an SNR larger than 30. The coherent vs. incoherent or noise log Bayes factors obtained using the neutrino mechanism signal model are shown in Figure 5.12(c). Most of the 42 signals have a log$B_{C,IN}$ large enough that they cannot be ruled out as a glitch or noise. The coherent vs. incoherent or noise log Bayes factors obtained using the magnetorotational signal model are shown in Figure 5.12(d). None of the sine Gaussian injections had a value of log$B_{S,N}$ and log$B_{C,IN}$ large enough to be considered as a possible CCSN signal candidate. For signal candi-

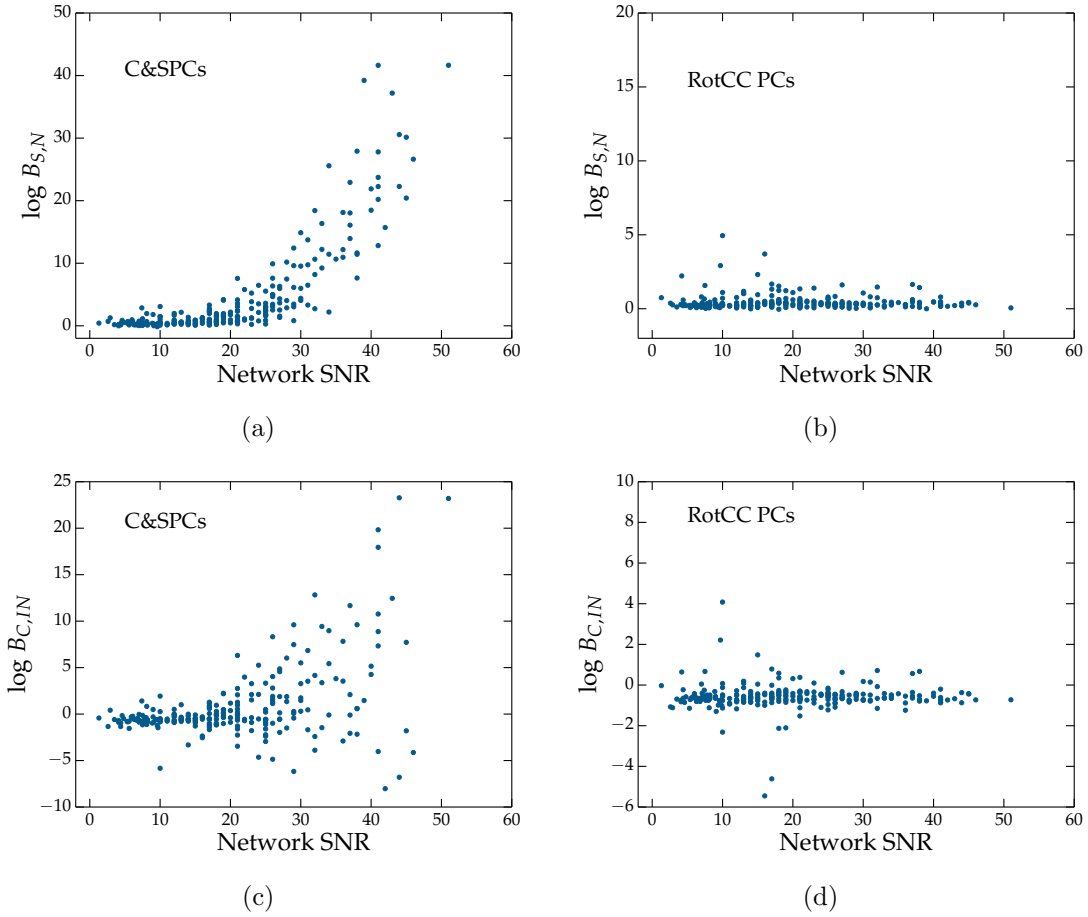

Figure 5.12: The log Bayes factors obtained for 250 sine Gaussian injections in O1 aLIGO noise. (a) The signal vs. noise log Bayes factors obtained using the neutrino mechanism signal model. (b) The signal vs. noise log Bayes factors obtained using the magnetorotational signal model. (c) The coherent vs. incoherent or noise log Bayes factors obtained using the neutrino mechanism signal model. (d) The coherent vs. incoherent or noise log Bayes factors obtained using the magnetorotational signal model. The SG signals considered as potential CCSN candidates are above SNR 30.

dates that have passed the coherence test, we can look at their reconstructed signal to determine if the signal matches one of the CCSN models considered in SMEE, or if the waveform is something unexpected from current CCSN simulations.

5.6 Reconstructions

In this section, we show how well SMEE can reconstruct a CCSN GW signal. To reconstruct the waveforms, SMEE uses Equation 2.17, with PC coefficients that are found by the nested sampler. As SMEE produces posterior distributions for each

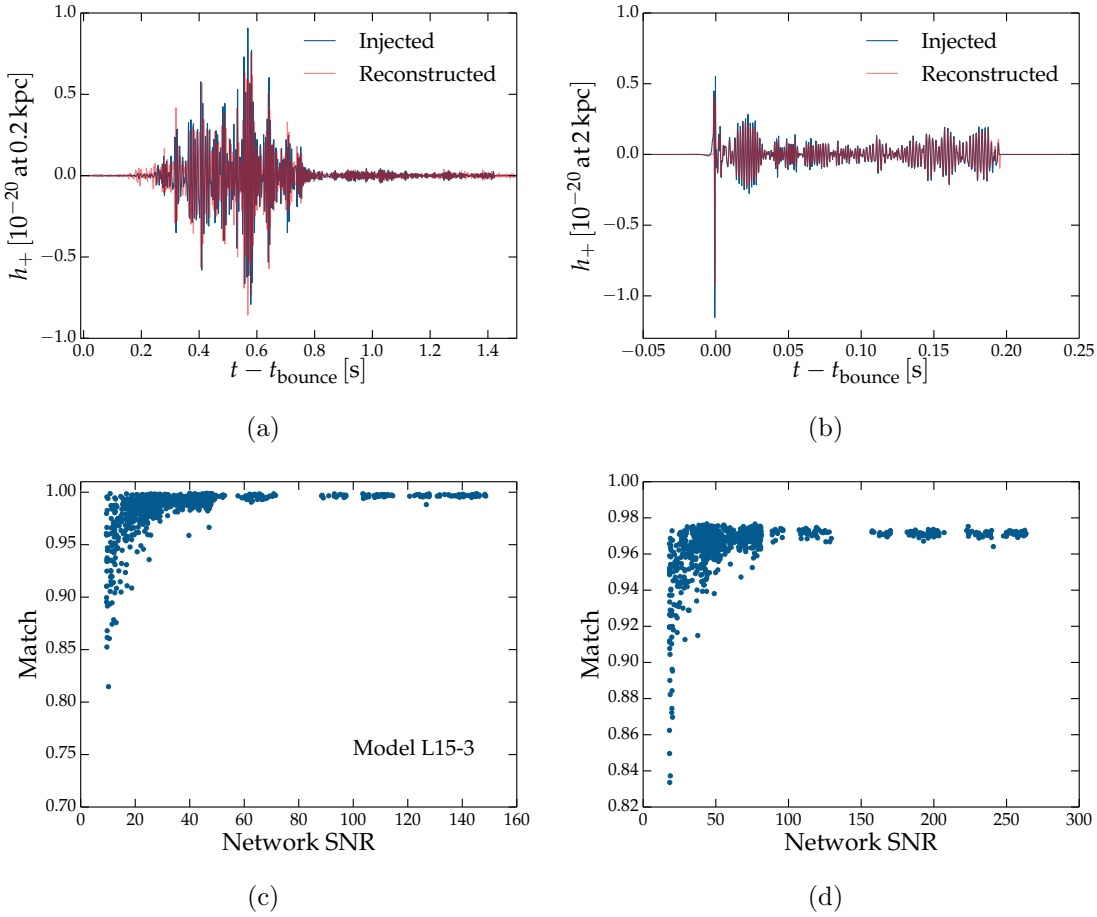

Figure 5.13: A measure of how well SMEE can reconstruct waveforms from different CCSN explosion mechanisms in data from O1. (a) The reconstruction of a Müller waveform using the neutrino mechanism signal model. (b) The reconstruction of a Scheidegger waveform using the magnetorotational signal model. (c) The match parameters for 1000 injected Müller waveforms. (d) The match parameters for 1000 Scheidegger waveforms. The reconstructed waveform is expected to be a good match for the signal in the data when the correct signal model is used.

of the PC coefficients, the 90% confidence intervals of the posteriors can be used to produce an error for each of the reconstructed waveforms. The reconstructions of the Müller, Scheidegger and sine Gaussian signals injected in O1 aLIGO noise are investigated. An example reconstruction of a Müller waveform is shown in Figure 5.13(a). As SMEE uses CCSN waveforms to create signal models, all waveforms reconstructed by SMEE will look like a CCSN signal, even if the signal in the data does not match the CCSN models considered by SMEE. Therefore, we can determine if the signal in the data is a CCSN signal by measuring how well the waveform was reconstructed. If the reconstruction is good, it is a CCSN signal, and if the reconstruction is bad, then it is another type of GW signal that does not match our current models.

To measure how well a waveform is reconstructed, a match parameter, α is calculated. It is a measure of the overlap between the injected and recovered waveforms. An injected waveform would not be available for a real detection, but it would be possible to carry out the same study using the reconstructed waveform produced by the unmodelled burst searches. The match is given by,

$$\alpha = \frac{\langle h_{rec}|h_{inj}\rangle}{\sqrt{\langle h_{rec}|h_{rec}\rangle\langle h_{inj}|h_{inj}\rangle}}\,, \tag{5.6}$$

where h_{rec} is the reconstructed signal, h_{inj} is the injected signal, and the inner product is given by,

$$\langle h_a|h_b\rangle = \int \frac{h_a^*(f)h_b(f)}{S(f)}df\,, \tag{5.7}$$

where $S(f)$ is the power spectral density. If the reconstructed waveform is an exact match for the signal in the data then α will be 1. If there is no match between the reconstructed waveform and the signal then the match will be 0.

The match parameters calculated for the 1000 Müller injections using the neutrino mechanism signal model are shown in Figure 5.13(c). All of the reconstructed waveforms were a good match for the injected signal. The match is higher than 95% for all of the Müller waveforms above SNR 20. The match parameter calculated for the 1000 Scheidegger injections using the magnetorotational signal model is shown in Figure 5.13(d). The maximum match achieved for the Scheidegger waveforms is ~ 0.97, and an example reconstructed waveform is shown in Figure 5.13(b).

5.6.1 Testing Robustness

To test the robustness of the result, three-dimensional waveforms that were not included in the PCs are used. As there are currently no more available three-dimensional waveforms that can be used for this test, the PCs are made again leaving out one of the signals from each of the explosion mechanisms. The left out waveform for the magnetorotational signal model is Scheidegger model $R3E1AC_L$. The left out waveform for the neutrino mechanism model is the Müller waveform L15-3. 7 PCs are then used for each signal model. SMEE is then run again on the 1000 Müller and Scheidegger injections, which are no longer included in the signal model. The result is shown in Figure 5.14. The maximum match for the Scheidegger waveforms is 0.82, and the maximum match for the Müller waveforms is 0.72. A

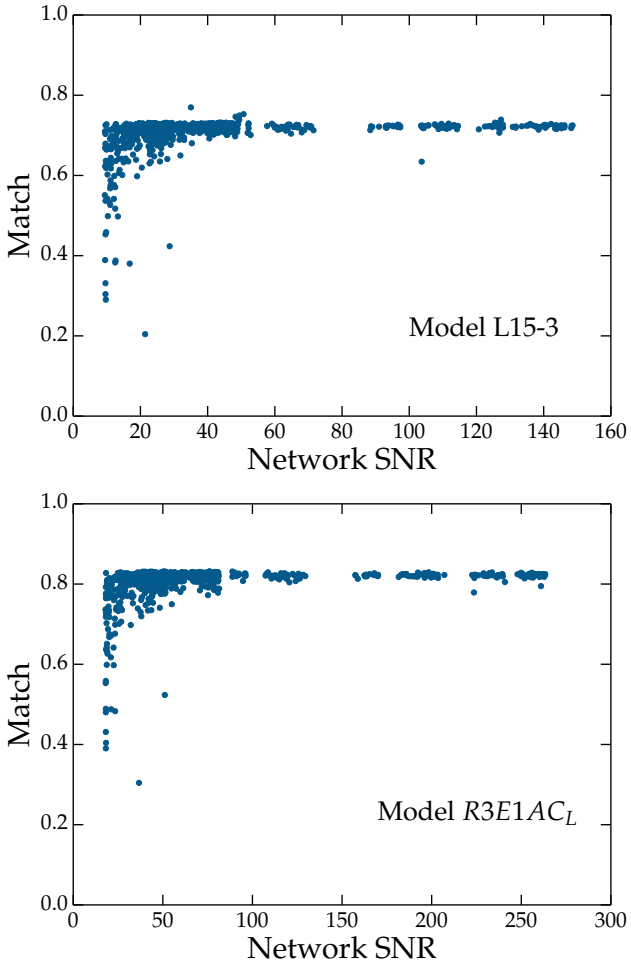

Figure 5.14: The match parameters calculated for three-dimensional waveforms not included in the signal model. The two waveforms are removed from the signal models and are then analysed again by SMEE as a test of the robustness of the method. The maximum match for the Scheidegger waveforms is now 0.82, and the maximum match for the Müller waveforms is 0.72. A better result is obtained for the magnetorotational waveforms as a larger number of simulations are available to model the signals.

better result is obtained for the magnetorotational waveforms as a larger number of simulations are available to model the signals. To be conservative, SMEE will only consider a signal candidate as being a CCSN if the match parameter is larger than 0.6.

5.6.2 Sine Gaussian Signals

Figure 5.15 shows how well the 250 sine Gaussian signals were reconstructed using the neutrino mechanism signal model and the magnetorotational signal model.

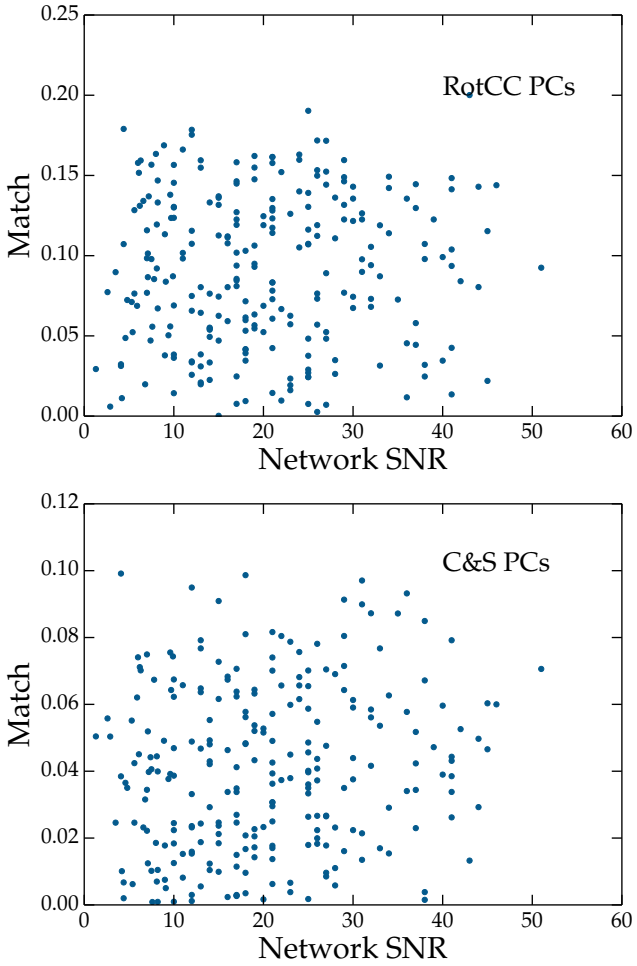

Figure 5.15: The match values for sine Gaussian injections reconstructed with neutrino mechanism (bottom) and magnetorotational mechanism signal models (top). The maximum match was 0.2 and 0.1 for the rapidly rotating signal model and neutrino signal model, respectively. All of the match values are too low for the signals to be considered as CCSN GW candidates. There is no correlation between SNR and match parameters as expected when the correct signal model is used.

When using the neutrino signal model, the maximum match parameter calculated was below 0.1. When using the magnetorotational signal model, the maximum match calculated was below 0.2. All of the matches for the sine Gaussian signals are much smaller than match values of greater than 0.6 expected for a CCSN signal. Therefore, we can conclude that none of the sine Gaussian signals that passed the coherence test belong to one of the two CCSN explosion models considered in SMEE.

5.7 Summary and Discussion

During the advanced GW detector observing runs, SMEE is used as a parameter estimation follow-up tool for potential CCSN signal candidates that are identified by the GW searches, or from alerts sent by electromagnetic and neutrino detectors. In this chapter, we update the signal models in SMEE to use three-dimensional neutrino mechanism and magnetorotational mechanism waveforms. Improvements to CCSN simulations have advanced rapidly in recent years, and using the latest available waveforms will maximise the potential for a GW CCSN detection and measurement of the signals astrophysical parameters.

For the new signal models, the ideal number of PCs is 5 for the magnetorotational signal model and 8 for the neutrino mechanism model. There is a large variance in the time series of the three-dimensional neutrino mechanism waveforms, as for the two-dimensional neutrino mechanism waveforms used in the previous chapter. A most robust result will be possible in the future when more CCSN simulations become available. We repeat the study in the previous chapter, injecting waveforms from both mechanisms at 10 GPS times in GW detector noise recoloured to aLIGO and AdVirgo design sensitivity. SMEE was able to correctly determine the explosion mechanism of all of the detected waveforms. The minimum SNR needed to detect the three-dimensional neutrino mechanism waveforms was greatly improved by using the signal models created from the three-dimensional waveforms.

A real CCSN GW signal candidate could potentially be a glitch, or a different type of astrophysical signal. In this chapter, we test the ability of SMEE to determine if a GW signal candidate is a CCSN signal, other astrophysical transient or a glitch. O1 data is used for this study, so that the glitches will be a good representation of what is expected during future observing runs. To test the method 1000 Müller waveforms, 1000 Scheidegger waveforms, 250 sine Gaussian signals, and the 250 loudest background triggers from the targeted O1 cWB search for CCSNe are used. It is shown that glitches can be eliminated as CCSN candidates by using Bayes factors to determine if the signal is coherent between all of the detectors being considered.

SMEE can produce a reconstruction of a CCSN candidate signal. The reconstructed signal will always look like a CCSN signal, as SMEE uses CCSN waveforms

to create a signal model. Therefore, if the reconstructed waveform is very different to the waveform in the data, this can be used to rule out a candidate signal as being one of the two CCSN models considered by SMEE. We find that by calculating the match parameter between the injected and recovered waveforms, that the sine Gaussian injections can be rejected as CCSN signal candidates. This method could help to determine if a CCSN signal has been detected when only one GW detector is operational.

Chapter 6

Summary and Discussion

The aLIGO GW detectors have made the first direct detections of GWs beginning a new era in GW astronomy [2, 19]. As AdVirgo joins the detector network, the rate of detections is expected to increase [12, 4, 5]. Although CBC signals are expected to be the most common source, the advanced detector network may detect GWs from other sources, such as individual neutron stars, core-collapse supernovae or an unexpected un-modelled source.

The non-Gaussian, non-stationary nature of advanced GW detector noise produces glitches, which affect the sensitivity of searches and could mimic a GW detection, in particular for un-modelled sources. Glitches can reduce the duty cycle of the instruments and decrease the sensitivity of the detectors. Multiple different types of glitches have been identified by their time-frequency morphology. If a glitch type is not correlated with any auxiliary channel that is not sensitive to GWs then it will not be removed by data quality vetoes, and their origin is particularly difficult to identify. Glitch classification and categorization may provide valuable clues for identifying the source of glitches, and possibly lead to their elimination. In initial LIGO and Virgo science runs, this classification was performed by visual inspection of the glitches' time series and/or spectrograms. In this thesis, we developed a method, called PC-LIB, designed for the fast classification of advanced detector glitches.

The performance of PC-LIB was tested on simulated data sets, and the results are compared to those obtained with other methods designed for glitch classification.

The classifiers have an efficiency of over 97% for glitches with an SNR above 20. As real noise from the advanced detectors is non-stationary and non-Gaussian, a better understanding of how the method would perform during the aLIGO observing runs was then required. In the ER7 data used to test PC-LIB, 95% of the detected glitches were classified correctly. A similarly high efficiency was obtained by other methods used in a second glitch classification comparison study in both H1 and L1 ER7 data. We conclude that all of the methods used for glitch classification in aLIGO and AdVirgo data have a high efficiency in real non-stationary, non-Gaussian detector noise.

During O1, PC-LIB was used to classify all glitches above SNR 12. The blip glitch was found to be the most common glitch in both of the detectors. Since blips are rarely removed by data quality vetoes, their accurate classification is crucial to improve GW searches, as an accurate categorization will allow us to search for couplings within the detector [41, 66]. The results of the O1 classification was then used to examine the effects of different glitch types on the estimated parameters of a GW burst signal. The change in the posterior peaks of the parameters is greatest when the signal occurs within 0.15 s of a glitch, and when the glitch SNR is louder than the signal SNR.

A CCSN has long been considered as a potential source for advanced GW detectors [100]. Although no CCSN were found in initial detector science runs, previous studies have shown that an advanced detector network could detect these sources out to the Large Magellanic Cloud (LMC) [51, 46]. In Chapter 4, we investigate Bayesian model selection techniques designed to determine the explosion mechanism of CCSN signals detected with an aLIGO and AdVirgo detector network. The tool used to achieve this is called the Supernova Model Evidence Extractor (SMEE).

The ability of SMEE to determine the CCSN explosion mechanism is demonstrated with a network of GW detectors, using real non-stationary, non-Gaussian detector noise. The magnetorotational and neutrino explosion mechanisms are considered. The results show that SMEE can determine the correct explosion mechanism for all detectable waveforms at distances throughout the Galaxy and out to the Large Magellanic Cloud. The model selection capabilities of SMEE were further enhanced with a careful selection of the number of PCs, which considered the relative complexity of the different explosion models. The two-dimensional rapidly-rotating core collapse waveforms, used in Chapter 4, are a good approximation

for three-dimensional rapidly-rotating waveforms, as non-axisymmetric instabilities only occur after the signal bounce that is the main feature represented by the signal models implemented in SMEE. However, three-dimensional neutrino waveforms contain features that are different from the two-dimensional waveforms used to create the PCs. SMEE needed to be updated to use three-dimensional waveforms for the CCSN signal models to maximise the potential for a CCSN detection and astrophysical parameter estimation.

In Chapter 5, SMEE is updated to create signal models using three-dimensional CCSN waveforms. With the new signal models, SMEE is able to correctly determine the explosion mechanism of all of the detectable waveforms throughout our Galaxy. The minimum SNR needed to detect the three-dimensional neutrino mechanism waveforms was greatly improved by using neutrino mechanism signal models created from three-dimensional waveforms. The ability of SMEE to determine if a GW signal candidate is a CCSN signal, other astrophysical transient or a glitch is tested. Data from O1 is used for this study, so that the glitch types will be similar to what is expected during future observing runs. To test the method 1000 Müller waveforms, 1000 Scheidegger waveforms, 250 sine Gaussian signals and use the 250 loudest background triggers from the targeted O1 cWB search for CCSNe are used. The results showed that glitches can be eliminated as CCSN candidates by using Bayes factors to determine if the signal is coherent between all of the detectors being considered. The match between the reconstructed waveform and the data can be used to determine if the signal is a CCSN or other type of astrophysical signal.

Bibliography

[1] G. M. Harry and LIGO Scientific Collaboration. Advanced LIGO: the next generation of gravitational wave detectors. *Classical and Quantum Gravity*, 27(8):084006, April 2010.

[2] B. P. Abbott et al. Observation of gravitational waves from a binary black hole merger. *Phys. Rev. Lett.*, 116:061102, Feb 2016.

[3] F. Acernese, M. Agathos, K. Agatsuma, D. Aisa, N. Allemandou, A. Allocca, J. Amarni, P. Astone, G. Balestri, G. Ballardin, and et al. Advanced Virgo: a second-generation interferometric gravitational wave detector. *Classical and Quantum Gravity*, 32(2):024001, January 2015.

[4] B. P. Abbott, R. Abbott, T. D. Abbott, M. R. Abernathy, F. Acernese, K. Ackley, C. Adams, T. Adams, P. Addesso, R. X. Adhikari, and et al. The Rate of Binary Black Hole Mergers Inferred from Advanced LIGO Observations Surrounding GW150914. *Astrophys. J. Lett.*, 833:L1, December 2016.

[5] B. P. Abbott, R. Abbott, T. D. Abbott, M. R. Abernathy, F. Acernese, K. Ackley, C. Adams, T. Adams, P. Addesso, R. X. Adhikari, and et al. Supplement: The Rate of Binary Black Hole Mergers Inferred from Advanced LIGO Observations Surrounding GW150914 (2016, ApJL, 833, L1). *Astrophys. J. Supp. Ser.*, 227:14, December 2016.

[6] J Aasi et al. Characterization of the ligo detectors during their sixth science run. *Classical and Quantum Gravity*, 32(11):115012, 2015.

[7] J. Powell, D. Trifirò, E. Cuoco, I. S. Heng, and M. Cavaglià. Classification methods for noise transients in advanced gravitational-wave detectors. *Class. Quantum Grav.*, 32(21):215012, November 2015.

[8] J. Powell, A. Torres-Forné, R. Lynch, D. Trifirò, E. Cuoco, M. Cavaglià, I. S. Heng, and J. A. Font. Classification methods for noise transients in advanced gravitational-wave detectors II: performance tests on Advanced LIGO data. *Classical and Quantum Gravity*, 34(3):034002, February 2017.

[9] J. Powell, S. E. Gossan, J. Logue, and I. S. Heng. Inferring the core-collapse supernova explosion mechanism with gravitational waves. *Phys. Rev. D*, 94(12):123012, December 2016.

[10] A. Einstein. Näherungsweise Integration der Feldgleichungen der Gravitation. *Sitzungsberichte der Königlich Preußischen Akademie der Wissenschaften (Berlin), Seite 688-696.*, 1916.

[11] A. Einstein. Über Gravitationswellen. *Sitzungsberichte der Königlich Preußischen Akademie der Wissenschaften (Berlin), Seite 154-167.*, 1918.

[12] F. Acernese et al. Status of Virgo. *Classical and Quantum Gravity*, 25(11):114045, June 2008.

[13] J. Abadie, B. P. Abbott, R. Abbott, M. Abernathy, T. Accadia, F. Acernese, C. Adams, R. Adhikari, P. Ajith, B. Allen, et al. TOPICAL REVIEW: Predictions for the rates of compact binary coalescences observable by ground-based gravitational-wave detectors. *Classical and Quantum Gravity*, 27(17):173001, September 2010.

[14] B. P. Abbott, R. Abbott, T. D. Abbott, M. R. Abernathy, F. Acernese, K. Ackley, C. Adams, T. Adams, P. Addesso, R. X. Adhikari, and et al. Binary Black Hole Mergers in the First Advanced LIGO Observing Run. *Physical Review X*, 6(4):041015, October 2016.

[15] B. P. Abbott, R. Abbott, T. D. Abbott, M. R. Abernathy, F. Acernese, K. Ackley, C. Adams, T. Adams, P. Addesso, R. X. Adhikari, and et al. Upper Limits on the Rates of Binary Neutron Star and Neutron Star-Black Hole Mergers from Advanced LIGO's First Observing Run. *Astrophys. J. Lett.*, 832:L21, December 2016.

[16] Robert Johnston. Gravitational wave-related images http://www.johnstonsarchive.net/relativity/pictures.html, 2005.

[17] R. A. Hulse and J. H. Taylor. Discovery of a pulsar in a binary system. *Astrophys. J. Lett.*, 195:L51–L53, January 1975.

[18] J. M. Weisberg and J. H. Taylor. The Relativistic Binary Pulsar B1913+16: Thirty Years of Observations and Analysis. In F. A. Rasio and I. H. Stairs, editors, *Binary Radio Pulsars*, volume 328 of *Astronomical Society of the Pacific Conference Series*, page 25, July 2005.

[19] B. P. Abbott et al. GW151226: Observation of Gravitational Waves from a 22-Solar-Mass Binary Black Hole Coalescence. *Phys. Rev. Lett.*, 116:241103, Jun 2016.

[20] B.S. Sathyaprakash and Bernard F. Schutz. Physics, astrophysics and cosmology with gravitational waves. *Living Reviews in Relativity*, 12(2), 2009.

[21] N. Andersson, V. Ferrari, D. I. Jones, K. D. Kokkotas, B. Krishnan, J. S. Read, L. Rezzolla, and B. Zink. Gravitational waves from neutron stars: promises and challenges. *General Relativity and Gravitation*, 43:409–436, February 2011.

[22] The LIGO Scientific Collaboration, the Virgo Collaboration, B. P. Abbott, R. Abbott, T. D. Abbott, M. R. Abernathy, F. Acernese, K. Ackley, C. Adams, T. Adams, and et al. First search for gravitational waves from known pulsars with Advanced LIGO. *ArXiv e-prints*, January 2017.

[23] Keith Riles for the LIGO Scientific Collaboration and Virgo Collaboration. Searches for continuous gravitational waves with the LIGO and Virgo detector. *ArXiv e-prints*, October 2012.

[24] Bender P et al. LISA pre-phase a report. *Unpublished*, 1998.

[25] T. Regimbau. The astrophysical gravitational wave stochastic background. *Research in Astronomy and Astrophysics*, 11:369–390, April 2011.

[26] A. Kamble and D. L. A. Kaplan. Electromagnetic Counterparts of Gravitational Wave Sources: Mergers of Compact Objects. *International Journal of Modern Physics D*, 22:1341011, January 2013.

[27] Bruce Allen, Warren G. Anderson, Patrick R. Brady, Duncan A. Brown, and Jolien D. E. Creighton. Findchirp: An algorithm for detection of gravitational waves from inspiraling compact binaries. *Phys. Rev. D*, 85:122006, Jun 2012.

[28] K. Cannon, A. Chapman, C. Hanna, D. Keppel, A. C. Searle, and A. J. Weinstein. Singular value decomposition applied to compact binary coalescence gravitational-wave signals. *Phys. Rev. D*, 82(4):044025, August 2010.

[29] K. Cannon et al. Toward Early-warning Detection of Gravitational Waves from Compact Binary Coalescence. *Astrophys. J.*, 748:136, April 2012.

[30] T. Dal Canton, A. H. Nitz, A. P. Lundgren, A. B. Nielsen, D. A. Brown, T. Dent, I. W. Harry, B. Krishnan, A. J. Miller, K. Wette, K. Wiesner, and J. L. Willis. Implementing a search for aligned-spin neutron star-black hole systems with advanced ground based gravitational wave detectors. *Phys. Rev. D*, 90(8):082004, October 2014.

[31] S. Privitera, S. R. P. Mohapatra, P. Ajith, K. Cannon, N. Fotopoulos, M. A. Frei, C. Hanna, A. J. Weinstein, and J. T. Whelan. Improving the sensitivity of a search for coalescing binary black holes with nonprecessing spins in gravitational wave data. *Phys. Rev. D*, 89(2):024003, January 2014.

[32] B. P. Abbott, R. Abbott, T. D. Abbott, M. R. Abernathy, F. Acernese, K. Ackley, C. Adams, T. Adams, P. Addesso, R. X. Adhikari, and et al. Properties of the Binary Black Hole Merger GW150914. *Physical Review Letters*, 116(24):241102, June 2016.

[33] Neil J Cornish and Tyson B Littenberg. Bayeswave: Bayesian inference for gravitational wave bursts and instrument glitches. *Classical and Quantum Gravity*, 32(13):135012, 2015.

[34] R. Lynch, S. Vitale, R. Essick, E. Katsavounidis, and F. Robinet. An information-theoretic approach to the gravitational-wave burst detection problem. *arXiv:1511.05955*, November 2015.

[35] S. Klimenko et al. Method for detection and reconstruction of gravitational wave transients with networks of advanced detectors. *Phys. Rev. D*, 93(4):042004, February 2016.

[36] S Klimenko et al. A coherent method for detection of gravitational wave bursts. *Classical and Quantum Gravity*, 25(11):114029, 2008.

[37] J. Aasi, B. P. Abbott, R. Abbott, T. Abbott, M. R. Abernathy, F. Acernese, K. Ackley, C. Adams, T. Adams, P. Addesso, and et al. Search for Gravitational Waves Associated with γ-ray Bursts Detected by the Interplanetary Network. *Physical Review Letters*, 113(1):011102, July 2014.

[38] J. Aasi, B. P. Abbott, R. Abbott, T. Abbott, M. R. Abernathy, T. Accadia, F. Acernese, K. Ackley, C. Adams, T. Adams, and et al. Search for gravitational radiation from intermediate mass black hole binaries in data from

the second LIGO-Virgo joint science run. *Phys. Rev. D*, 89(12):122003, June 2014.

[39] T. Damour and A. Vilenkin. Gravitational radiation from cosmic (super)strings: Bursts, stochastic background, and observational windows. *Phys. Rev. D*, 71(6):063510, March 2005.

[40] C. D. Ott. TOPICAL REVIEW: The gravitational-wave signature of core-collapse supernovae. *Class. Quantum Grav.*, 26:063001, March 2009.

[41] B. P. Abbott et al. Observing gravitational-wave transient GW150914 with minimal assumptions. *Phys. Rev. D*, 93:122004, Jun 2016.

[42] V Necula, S Klimenko, and G Mitselmakher. Transient analysis with fast wilson-daubechies time-frequency transform. *Journal of Physics: Conference Series*, 363(1):012032, 2012.

[43] S. Klimenko, S. Mohanty, M. Rakhmanov, and G. Mitselmakher. Constraint likelihood analysis for a network of gravitational wave detectors. *Phys. Rev. D*, 72(12):122002, December 2005.

[44] R. Essick, S. Vitale, E. Katsavounidis, G. Vedovato, and S. Klimenko. Localization of Short Duration Gravitational-wave Transients with the Early Advanced LIGO and Virgo Detectors. *Astrophys. J.*, 800:81, February 2015.

[45] W. Baade and F. Zwicky. Cosmic Rays from Super-novae. *Proceedings of the National Academy of Science*, 20:259–263, May 1934.

[46] S. E. Gossan, P. Sutton, A. Stuver, M. Zanolin, K. Gill, and C. D. Ott. Observing gravitational waves from core-collapse supernovae in the advanced detector era. *Phys. Rev. D*, 93(4):042002, February 2016.

[47] S. van den Bergh and G. A. Tammann. Galactic and extragalactic supernova rates. *Ann. Rev. Astron. Astroph.*, 29:363–407, 1991.

[48] E. Cappellaro, M. Turatto, S. Benetti, D. Y. Tsvetkov, O. S. Bartunov, and I. N. Makarova. The Rate of Supernovae - Part Two - the Selection Effects and the Frequencies Per Unit Blue Luminosity. *Astron. Astrophys.*, 273:383, June 1993.

[49] E. N. Alexeyev and L. N. Alexeyeva. Twenty years of galactic observations in searching for bursts of collapse neutrinos with the baksan underground scintillation telescope. *Journal of Experimental and Theoretical Physics*, 95(1):5–10, 2002.

[50] K. Gill, M. Branchesi, M. Zanolin, and Szczepanczyk M. The rate of core-collapse supernovae within the local universe yielding astrophysically based sne populations for all sky searches. *In prep*, 2016.

[51] B. P. Abbott et al. First targeted search for gravitational-wave bursts from core-collapse supernovae in data of first-generation laser interferometer detectors. *Phys. Rev. D*, 94:102001, Nov 2016.

[52] J. Weber. Detection and generation of gravitational waves. *Phys. Rev.*, 117:306–313, Jan 1960.

[53] J. Weber. Evidence for Discovery of Gravitational Radiation. *Physical Review Letters*, 22:1320–1324, June 1969.

[54] C Affeldt, K Danzmann, K L Dooley, H Grote, M Hewitson, S Hild, J Hough, J Leong, H Lck, M Prijatelj, S Rowan, A Rdiger, R Schilling, R Schnabel, E Schreiber, B Sorazu, K A Strain, H Vahlbruch, B Willke, W Winkler, and H Wittel. Advanced techniques in GEO 600. *Classical and Quantum Gravity*, 31(22):224002, 2014.

[55] M Punturo et al. The einstein telescope: a third-generation gravitational wave observatory. *Classical and Quantum Gravity*, 27(19):194002, 2010.

[56] Yoichi Aso, Yuta Michimura, Kentaro Somiya, Masaki Ando, Osamu Miyakawa, Takanori Sekiguchi, Daisuke Tatsumi, and Hiroaki Yamamoto. Interferometer design of the KAGRA gravitational wave detector. *Phys. Rev. D*, 88:043007, Aug 2013.

[57] P McNamara and S Vitale and K Danzmann and on behalf of the LISA Pathfinder Science Working Team. LISA Pathfinder. *Classical and Quantum Gravity*, 25(11):114034, 2008.

[58] M. Armano et al. Sub-Femto-g Free Fall for Space-Based Gravitational Wave Observatories: LISA Pathfinder Results. *Phys. Rev. Lett.*, 116:231101, Jun 2016.

[59] The LIGO Scientific Collaboration and The Virgo Collaboration. Sensitivity Achieved by the LIGO and Virgo Gravitational Wave Detectors during LIGO's Sixth and Virgo's Second and Third Science Runs. *ArXiv e-prints*, March 2012.

[60] J. Abadie, B. P. Abbott, R. Abbott, T. D. Abbott, M. Abernathy, T. Accadia, F. Acernese, C. Adams, R. Adhikari, C. Affeldt, et al. All-sky search for gravitational-wave bursts in the second joint LIGO-Virgo run. *Phys. Rev. D*, 85(12):122007, June 2012.

[61] J. Aasi, J. Abadie, B. P. Abbott, R. Abbott, T. D. Abbott, M. Abernathy, T. Accadia, F. Acernese, C. Adams, T. Adams, and et al. Search for gravitational waves from binary black hole inspiral, merger, and ringdown in LIGO-Virgo data from 2009-2010. *Phys. Rev. D*, 87(2):022002, January 2013.

[62] N. Christensen. LIGO S6 detector characterization studies. *Class.Quant.Grav.*, 27:194010, 2010.

[63] J. Aasi, J. Abadie, B. P. Abbott, R. Abbott, T. D. Abbott, M. Abernathy, T. Accadia, F. Acernese, C. Adams, T. Adams, et al. The characterization of Virgo data and its impact on gravitational-wave searches. *Classical and Quantum Gravity*, 29(15):155002, August 2012.

[64] J. R. Smith, T. Abbott, E. Hirose, N. Leroy, D. MacLeod, J. McIver, P. Saulson, and P. Shawhan. A hierarchical method for vetoing noise transients in gravitational-wave detectors. *Classical and Quantum Gravity*, 28(23):235005, December 2011.

[65] P. Ajith, T. Isogai, N. Christensen, R. X. Adhikari, A. B. Pearlman, A. Wein, A. J. Weinstein, and B. Yuan. Instrumental vetoes for transient gravitational-wave triggers using noise-coupling models: The bilinear-coupling veto. *Phys. Rev. D*, 89(12):122001, June 2014.

[66] The LIGO Scientific Collaboration and the Virgo Collaboration. Characterization of transient noise in advanced ligo relevant to gravitational wave signal GW150914. *Classical and Quantum Gravity*, 33(13):134001, 2016.

[67] J. Aasi et al. Advanced LIGO. *Classical and Quantum Gravity*, 32(7):074001, 2015.

[68] S Mukherjee, R Obaid, and B Matkarimov. Classification of glitch waveforms in gravitational wave detector characterization. *Journal of Physics: Conference Series*, 243(1):012006, 2010.

[69] LIGO Algorithm Library. www.lsc-group.phys.uwm.edu/daswg/projects/lalsuite.html.

[70] J. Veitch, V. Raymond, B. Farr, W. Farr, P. Graff, S. Vitale, B. Aylott, K. Blackburn, N. Christensen, M. Coughlin, W. Del Pozzo, F. Feroz, J. Gair, C.-J. Haster, V. Kalogera, T. Littenberg, I. Mandel, R. O'Shaughnessy, M. Pitkin, C. Rodriguez, C. Rover, T. Sidery, R. Smith, M. Van Der Sluys, A. Vecchio, W. Vousden, and L. Wade. Parameter estimation for compact binaries with ground-based gravitational wave observations using the LALInference software library. *Phys. Rev. D*, 91(4):042003, February 2015.

[71] L. P. Singer, L. R. Price, B. Farr, A. L. Urban, C. Pankow, S. Vitale, J. Veitch, W. M. Farr, C. Hanna, K. Cannon, T. Downes, P. Graff, C.-J. Haster, I. Mandel, T. Sidery, and A. Vecchio. The First Two Years of Electromagnetic Follow-up with Advanced LIGO and Virgo. *Astrophys. J.*, 795:105, November 2014.

[72] D. S. Sivia. *Data Analysis, A Bayesian Tutorial*. Oxford, 1996.

[73] J. Veitch and A. Vecchio. Bayesian coherent analysis of in-spiral gravitational wave signals with a detector network. *Phys. Rev. D*, 81(6):062003, March 2010.

[74] F. Feroz, M. P. Hobson, E. Cameron, and A. N. Pettitt. Importance Nested Sampling and the MultiNest Algorithm. *ArXiv e-prints*, June 2013.

[75] J. Logue, C. D. Ott, I. S. Heng, P. Kalmus, and J. Scargill. Inferring Core-Collapse Supernova Physics with Gravitational Waves. *Phys. Rev. D*, 86(4):044023, August 2012.

[76] F. Robinet. Omicron: an algorithm to detect and characterize transient events in gravitational-wave detectors. 2015.

[77] S. Chatterji, L. Blackburn, G. Martin, and E. Katsavounidis. Multiresolution techniques for the detection of gravitational-wave bursts. *Classical and Quantum Gravity*, 21:S1809–S1818, October 2004.

[78] J.E. Jackson. *A User's Guide to Principal Components*. Wiley series in probability and mathematical statistics: Applied probability and statistics. Wiley, 2003.

[79] Yaser S Abu-Mostafa, Malik Magdon-Ismail, and Hsuan-Tien Lin. *Learning from data*. AMLBook, 2012.

[80] F. Pedregosa, G. Varoquaux, A. Gramfort, V. Michel, B. Thirion, O. Grisel, M. Blondel, P. Prettenhofer, R. Weiss, V. Dubourg, J. Vanderplas, A. Passos, D. Cournapeau, M. Brucher, M. Perrot, and E. Duchesnay. Scikit-learn: Machine Learning in Python . *Journal of Machine Learning Research*, 12:2825–2830, 2011.

[81] H.S. Bhat and N. Kumar. On the Derivation of the Bayesian Information Criterion. Technical report, 2010.

[82] J. Friedm T. Hastie, R. Tibshirani. *The Elements of Statistical Learning*. Springer, 2001.

[83] F. Acernese et al. NAP: a tool for noise data analysis. Application to Virgo engineering runs. *Classical and Quantum Gravity*, 22(18):S1041, 2005.

[84] Ingrid Daubechies et al. *Ten lectures on wavelets*, volume 61. SIAM, 1992.

[85] S. Mallat. *A wavelet tour of signal processing*. Academic Press, 1998.

[86] E. Cuoco, G. Calamai, L. Fabbroni, G. Losurdo, M. Mazzoni, R. Stanga, and F. Vetrano. On-line power spectra identification and whitening for the noise in interferometric gravitational wave detectors. *Classical and Quantum Gravity*, 18(9):1727, 2001.

[87] David L Donoho and Jain M Johnstone. Ideal spatial adaptation by wavelet shrinkage. *Biometrika*, 81(3):425–455, 1994.

[88] Brendan J Frey and Delbert Dueck. Clustering by passing messages between data points. *science*, 315(5814):972–976, 2007.

[89] D. Arthur and S. Vassilvitskii. k-means++: the advantages of careful seeding. In *SODA '07: Proceedings of the eighteenth annual ACM-SIAM symposium on Discrete algorithms*, pages 1027–1035. Society for Industrial and Applied Mathematics, 2007.

[90] A. Y. Ng, M. I. Jordan, and Y. Weiss. On spectral clustering: Analysis and an algorithm. In *Advances in neural information processing systems*, pages 849–856. MIT Press, 2001.

[91] Mikhail Belkin and Partha Niyogi. Laplacian eigenmaps for dimensionality reduction and data representation. *Neural computation*, 15(6):1373–1396, 2003.

[92] M Zevin, S Coughlin, S Bahaadini, E Besler, N Rohani, S Allen, M Cabero, K Crowston, A K Katsaggelos, S L Larson, T K Lee, C Lintott, T B Littenberg, A Lundgren, C sterlund, J R Smith, L Trouille, and V Kalogera. Gravity spy: integrating advanced ligo detector characterization, machine learning, and citizen science. *Classical and Quantum Gravity*, 34(6):064003, 2017.

[93] D Trifiro. ldas-jobs.ligo-wa.caltech.edu/$\tilde{\text{b}}$rethil/time_PCAT/L1:GAUSSIAN/MDC-3/whitened_highpassed_40.0_amplitude_t-4.5_w-512/.

[94] D Trifiro. ldas-jobs.ligo-wa.caltech.edu/$\tilde{\text{b}}$rethil/time_PCAT/L1:GAUSSIAN/MDC-1/whitened_highpassed_40.0_amplitude_t-4.5_w-512/.

[95] R. Biswas et al. Application of machine learning algorithms to the study of noise artifacts in gravitational-wave data. *Phys. Rev. D*, 88(6):062003, September 2013.

[96] R. Essick, L. Blackburn, and E. Katsavounidis. Optimizing vetoes for gravitational-wave transient searches. *Classical and Quantum Gravity*, 30(15):155010, August 2013.

[97] J. McIver, A. Lundgren, D. Macleod, L. Nuttall, T.J. Massinger, et al. Data Quality (DQ) Shifts Pre O1. 2015.

[98] J. Areeda and J. Smith. LIGOdv-web: Providing easy, secure and universal access to a large distributed scientific data store for the LIGO Scientific Collaboration. 2016.

[99] J. Smith. aLIGO Glitch Classes Seen So Far.

[100] C. D. Ott, A. Burrows, E. Livne, and R. Walder. Gravitational Waves from Axisymmetric, Rotating Stellar Core Collapse. *Astrophys. J.*, 600:834–864, January 2004.

[101] E. Baron and J. Cooperstein. The effect of iron core structure on supernovae. *Astrophys. J.*, 353:597–611, April 1990.

[102] H. A. Bethe. Supernova mechanisms. *Reviews of Modern Physics*, 62:801–866, October 1990.

[103] E. O'Connor and C. D. Ott. Black Hole Formation in Failing Core-Collapse Supernovae. *Astrophys. J.*, 730:70, April 2011.

[104] A. Heger, S. E. Woosley, and H. C. Spruit. Presupernova Evolution of Differentially Rotating Massive Stars Including Magnetic Fields. *Astrophys. J.*, 626:350–363, June 2005.

[105] N. Langer. Presupernova Evolution of Massive Single and Binary Stars. *Ann. Rev. Astron. Astroph.*, 50:107–164, September 2012.

[106] T. Takiwaki and K. Kotake. Gravitational Wave Signatures of Magnetohydrodynamically Driven Core-collapse Supernova Explosions. *Astrophys. J.*, 743:30, December 2011.

[107] A. Burrows, L. Dessart, E. Livne, C. D. Ott, and J. Murphy. Simulations of Magnetically Driven Supernova and Hypernova Explosions in the Context of Rapid Rotation. *Astrophys. J.*, 664:416–434, July 2007.

[108] C. D. Ott, A. Burrows, T. A. Thompson, E. Livne, and R. Walder. The Spin Periods and Rotational Profiles of Neutron Stars at Birth. *Astrophys. J. Supp. Ser.*, 164:130, May 2006.

[109] T. Rembiasz, J. Guilet, M. Obergaulinger, P. Cerdá-Durán, M. A. Aloy, and E. Müller. On the maximum magnetic field amplification by the magnetorotational instability in core-collapse supernovae. *Mon. Not. Roy. Astron. Soc.*, 460:3316–3334, August 2016.

[110] P. Mösta, C. D. Ott, D. Radice, L. F. Roberts, E. Schnetter, and R. Haas. A large-scale dynamo and magnetoturbulence in rapidly rotating core-collapse supernovae. *nature*, 528:376–379, December 2015.

[111] H. Dimmelmeier, C. D. Ott, A. Marek, and H.-Thomas Janka. Gravitational wave burst signal from core collapse of rotating stars. *Phys. Rev. D*, 78:064056, 2008.

[112] S. Scheidegger, R. Käppeli, S. C. Whitehouse, T. Fischer, and M. Liebendörfer. The influence of model parameters on the prediction of gravitational wave signals from stellar core collapse. *Astron. Astrophys.*, 514:A51, May 2010.

[113] E. Abdikamalov, S. Gossan, A. M. DeMaio, and C. D. Ott. Measuring the angular momentum distribution in core-collapse supernova progenitors with gravitational waves. *Phys. Rev. D*, 90(4):044001, August 2014.

[114] J. M. Lattimer and F. Douglas Swesty. A generalized equation of state for hot, dense matter. *Nuclear Physics A*, 535:331–376, December 1991.

[115] H. Shen, H. Toki, K. Oyamatsu, and K. Sumiyoshi. Relativistic equation of state of nuclear matter for supernova and neutron star. *Nuclear Physics A*, 637:435–450, July 1998.

[116] H. Shen, H. Toki, K. Oyamatsu, and K. Sumiyoshi. Relativistic Equation of State of Nuclear Matter for Supernova Explosion. *Progress of Theoretical Physics*, 100:1013–1031, November 1998.

[117] W. David Arnett. Gravitational collapse and weak interactions. *Canadian Journal of Physics*, 44(11):2553–2594, 1966.

[118] S. A. Colgate and R. H. White. The Hydrodynamic Behavior of Supernovae Explosions. *Astrophys. J.*, 143:626, March 1966.

[119] H. A. Bethe and J. R. Wilson. Revival of a stalled supernova shock by neutrino heating. *Astrophys. J.*, 295:14–23, August 1985.

[120] H.-T. Janka. Explosion Mechanisms of Core-Collapse Supernovae. *Ann. Rev. Nuc. Par. Sci.*, 62:407, November 2012.

[121] Adam Burrows. Colloquium. *Rev. Mod. Phys.*, 85:245–261, Feb 2013.

[122] J. M. Blondin, A. Mezzacappa, and C. DeMarino. Stability of Standing Accretion Shocks, with an Eye toward Core-Collapse Supernovae. *Astrophys. J.*, 584:971–980, February 2003.

[123] T. Foglizzo, P. Galletti, L. Scheck, and H.-T. Janka. Instability of a Stalled Accretion Shock: Evidence for the Advective-Acoustic Cycle. *Astrophys. J.*, 654:1006–1021, January 2007.

[124] T. Foglizzo, L. Scheck, and H.-T. Janka. Neutrino-driven Convection versus Advection in Core-Collapse Supernovae. *Astrophys. J.*, 652:1436–1450, December 2006.

[125] L. Scheck, H.-T. Janka, T. Foglizzo, and K. Kifonidis. Multidimensional supernova simulations with approximative neutrino transport. II. Convection and the advective-acoustic cycle in the supernova core. *Astron. Astrophys.*, 477:931–952, January 2008.

[126] T. Kuroda, K. Kotake, and T. Takiwaki. A New Gravitational-wave Signature from Standing Accretion Shock Instability in Supernovae. *Astrophys. J. Lett.*, 829:L14, September 2016.

[127] J. W. Murphy, C. D. Ott, and A. Burrows. A Model for Gravitational Wave Emission from Neutrino-Driven Core-Collapse Supernovae. *Astrophys. J.*, 707:1173–1190, December 2009.

[128] C. D. Ott et al. General-relativistic Simulations of Three-dimensional Core-collapse Supernovae. *Astrophys. J.*, 768:115, May 2013.

[129] K. N. Yakunin, P. Marronetti, A. Mezzacappa, S. W. Bruenn, C.-T. Lee, M. A. Chertkow, W. R. Hix, J. M. Blondin, E. J. Lentz, O. E. Bronson Messer, and S. Yoshida. Gravitational waves from core collapse supernovae. *Class. Quantum Grav.*, 27:194005, October 2010.

[130] E. Müller, H.-T. Janka, and A. Wongwathanarat. Parametrized 3D models of neutrino-driven supernova explosions. Neutrino emission asymmetries and gravitational-wave signals. *Astron. Astrophys.*, 537:A63, January 2012.

[131] C. W. Misner, K. S. Thorne, and J. A. Wheeler. *Gravitation.* San Francisco: W.H. Freeman and Co., 1973.

[132] S. E. Woosley, A. Heger, and T. A. Weaver. The evolution and explosion of massive stars. *Rev. Mod. Phys.*, 74:1015–1071, Nov 2002.

[133] B. J. Owen and B. S. Sathyaprakash. Matched filtering of gravitational waves from inspiraling compact binaries: Computational cost and template placement. *Phys. Rev. D*, 60(2):022002, July 1999.

[134] T. Z. Summerscales, A. Burrows, L. S. Finn, and C. D. Ott. Maximum Entropy for Gravitational Wave Data Analysis: Inferring the Physical Parameters of Core-Collapse Supernovae. *Astrophys. J.*, 678:1142–1157, May 2008.

[135] Jessica McIver. *The impact of terrestrial noise on the detectability and reconstruction of gravitational wave signals from core-collapse supernovae.* PhD thesis, University of Massachusetts Amherst, 9 2015.

[136] Patrick R Brady and Saikat Ray-Majumder. Incorporating information from source simulations into searches for gravitational-wave bursts. *Classical and Quantum Gravity*, 21(20):S1839, 2004.

[137] I. S. Heng. Rotating stellar core-collapse waveform decomposition: a principal component analysis approach. *Class. Quantum Grav.*, 26(10):105005, May 2009.

[138] C. Röver, M.-A. Bizouard, N. Christensen, H. Dimmelmeier, I. S. Heng, and R. Meyer. Bayesian reconstruction of gravitational wave burst signals from simulations of rotating stellar core collapse and bounce. *Phys. Rev. D*, 80(10):102004, November 2009.

[139] K. Cannon, A. Chapman, C. Hanna, D. Keppel, A. C. Searle, and A. J. Weinstein. Singular value decomposition applied to compact binary coalescence gravitational-wave signals. *Phys. Rev. D*, 82(4):044025, August 2010.

[140] R. J. E. Smith, K. Cannon, C. Hanna, D. Keppel, and I. Mandel. Towards rapid parameter estimation on gravitational waves from compact binaries using interpolated waveforms. *Phys. Rev. D*, 87(12):122002, June 2013.

[141] Michael Prrer. Frequency-domain reduced order models for gravitational waves from aligned-spin compact binaries. *Classical and Quantum Gravity*, 31(19):195010, 2014.

[142] Jonathan Blackman, Scott E. Field, Chad R. Galley, Béla Szilágyi, Mark A. Scheel, Manuel Tiglio, and Daniel A. Hemberger. Fast and accurate prediction of numerical relativity waveforms from binary black hole coalescences using surrogate models. *Phys. Rev. Lett.*, 115:121102, Sep 2015.

[143] J A Clark, A Bauswein, N Stergioulas, and D Shoemaker. Observing gravitational waves from the post-merger phase of binary neutron star coalescence. *Classical and Quantum Gravity*, 33(8):085003, 2016.

[144] A. Burrows, E. Livne, L. Dessart, C. D. Ott, and J. Murphy. A New Mechanism for Core-Collapse Supernova Explosions. *Astrophys. J.*, 640:878–890, April 2006.

[145] L. Wang and J. C. Wheeler. Spectropolarimetry of Supernovae. *Ann. Rev. Astron. Astroph.*, 46:433, September 2008.

[146] R. Chornock et al. The Transitional Stripped-envelope SN 2008ax: Spectral Evolution and Evidence for Large Asphericity. *Astrophys. J.*, 739:41, September 2011.

[147] N. Smith et al. SN 2010jp (PTF10aaxi): a jet in a Type II supernova. *Mon. Not. Roy. Astron. Soc.*, 420:1135, February 2012.

[148] B. Sinnott, D. L. Welch, A. Rest, P. G. Sutherland, and M. Bergmann. Asymmetry in the Outburst of SN 1987A Detected Using Light Echo Spectroscopy. *Astrophys. J.*, 767:45, April 2013.

[149] S. E. Boggs et al. ^{44}Ti gamma-ray emission lines from SN1987A reveal an asymmetric explosion. *Science*, 348:670–671, May 2015.

[150] C. D. Ott, H. Dimmelmeier, A. Marek, H.-T. Janka, I. Hawke, B. Zink, and E. Schnetter. 3D Collapse of Rotating Stellar Iron Cores in General Relativity Including Deleptonization and a Nuclear Equation of State. *Physical Review Letters*, 98(26):261101, June 2007.

[151] M. Shibata and Y.-I. Sekiguchi. Three-dimensional simulations of stellar core collapse in full general relativity: Nonaxisymmetric dynamical instabilities. *Phys. Rev. D*, 71(2):024014, January 2005.

[152] S. Scheidegger, T. Fischer, S. C. Whitehouse, and M. Liebendörfer. Gravitational waves from 3D MHD core collapse simulations. *Astron. Astrophys.*, 490:231–241, October 2008.

[153] H. Andresen, B. Mueller, E. Mueller, and H.-T. Janka. Gravitational Wave Signals from 3D Neutrino Hydrodynamics Simulations of Core-Collapse Supernovae. *ArXiv e-prints*, July 2016.

[154] T. Kuroda, T. Takiwaki, and K. Kotake. Gravitational wave signatures from low-mode spiral instabilities in rapidly rotating supernova cores. *Phys. Rev. D*, 89(4):044011, February 2014.

[155] K. Kotake, W. Iwakami-Nakano, and N. Ohnishi. Effects of Rotation on Stochasticity of Gravitational Waves in the Nonlinear Phase of Core-collapse Supernovae. *Astrophys. J.*, 736:124, August 2011.

[156] K. Kotake, W. Iwakami, N. Ohnishi, and S. Yamada. Stochastic Nature of Gravitational Waves from Supernova Explosions with Standing Accretion Shock Instability. *Astrophys. J. Lett.*, 697:L133–L136, June 2009.

[157] K. Yakunin, P. Marronetti, O. B. Messer, A. Mezzacappa, E. J. Lentz, S. W. Bruenn, W. R. Hix, J. A. Harris, and J. M. Blondin. 3D Core-Collapse Supernova Models: Gravitational and Neutrino Signatures. In *American Astronom-*

ical Society Meeting Abstracts #223, volume 223 of *American Astronomical Society Meeting Abstracts*, page 354.09, January 2014.

[158] Joshua Logue. *Bayesian model selection with gravitational waves from supernovae*. PhD thesis, University of Glasgow, 2 2015.

[159] M. Vallisneri et al. The LIGO Open Science Center. *Journal of Physics Conference Series*, 610(1):012021, May 2015.

[160] N. N. Weinberg and E. Quataert. Non-linear saturation of g-modes in proto-neutron stars: quieting the acoustic engine. *Mon. Not. Roy. Astron. Soc.*, 387:L64–L68, June 2008.

[161] K. N. Yakunin et al. Gravitational wave signatures of ab initio two-dimensional core collapse supernova explosion models for 12 -25 M stars. *Phys. Rev. D*, 92(8):084040, October 2015.